UNIVERSITY *of the*
WESTERN CAPE

Electrochemically Enhanced Ferric Lithium Manganese Phosphate/Multi-Walled Carbon Nanotube, as a Possible Composite Cathode Material for Lithium Ion Battery

Sabelo Sifuba

(BSc Honours)

A mini thesis submitted in partial fulfilment of the requirements for the degree of

Magister Scientiae in Nanoscience

Faculty of Science

University of the Western Cape, Bellville, Cape Town, South Africa

Supervisors: Dr Natasha Ross, Prof Emmanuel Iwuoha

Co-supervisors: Dr Usisipho Feleni

May 2019

DECLARATION

I hereby declare that this *"Electrochemically enhanced iron doped lithium manganese phosphate ($LiFe_{0.5}Mn_{0.5}PO_4$)-multi-walled carbon nanotube cathode system"* that is submit for the research qualification

Magister Scientiae in Nanoscience

to the University of the Western Cape, is, apart from the recognised assistance of my supervisors, my own work and has not previously been submitted by me to another institution to obtain a research diploma or degree.

_____ on this ____ day of _____

(Candidate)

_____ on this ____ day of _____

(Supervisor)

_____ on this ____ day of _____

(Co-supervisor)

_____ on this ____ day of _____

(Co-supervisor)

DEDICATION

This work is dedicated to:

My late parents; Nontsikelelo Sifuba and Zamukulungisa Sifuba,

My siblings;

Nomalinge Sifuba, Luleka Sifuba, Nokonwaba Sifuba, Xolile Sifuba, Nomthandazo Sifuba, Bathobele Sifuba and my late brother Nyameko Sifuba.

My children;

Iminathi Sifuba and Sinothando Raydene Sifuba.

ACKNOWLEDGEMENTS

To God almighty that created and gave me mental and physical strength to complete this project and the one behind all my successes, be the glory and honour. I would like to thank both my supervisors, Prof Emmanuel Iwuoha and Dr Ross, for the encouragement and support that they have been giving throughout the course of the year, may God richly bless them. To my co-supervisors, Dr Usisipho Feleni, thank you for your advice and guidance for this project. To my family Nomalinge (may you get well soon, and God be with you), Luleka, Nokonwaba, Xolile, Nomthandazo, and Bathobele), and my friends (Nyameko Skoti, Wanele Buswana, Bangile Rolihlahla Yongama Ngayeka, Wandisa Wandisa Mandla, Noniko Nqakala, Penny Mathumba, Siyabonga Mdluli and Emanuel Ramoroka) I would like to send a big thank for your support and encouragement that you always give me, it has been a challenging year for me emotionally and physically, but you made everything easy for me, and you always believed in me. I would also like to Thank Yolanda Shezi, for the support you gave throughout this journey, always encouraging, and supportive through bad and good times. To the SensorLab family, it has been fun working with you guys though frustrating at times, thanks to everyone who ever willing to help. To the 2017 Nanoscience group I would like to express my sincere gratitude to all for their insight and guidance. I am honoured to have worked with such ingenious individuals' thanks for your encouragements. A big thank you to my family and friends, who showed a great support and kept motivating and supportive me throughout my studies. I also would like to acknowledge National Nanosciences Postgraduate Teaching and Training Platform (NNPTTP) for the award of MSc Scholarship, and lastly but not the least, the Chemistry Department and UWC, for providing me the opportunity to study for this postgraduate degree.

LIST OF PUBLICATIONS AND CONFERENCES

1. Ross, N., Nqakala, N., Willenberg, S., **Sifuba, S**. and Iwuoha, E., 2019. Electrochemical Properties of Polyoxometalate (H3PMo 12 O 40)-Functionalized Graphitic Carbon Nitride (gC 3 N 4). *Electrocatalysis*, pp.1-7.

2. **SACI/RSC Western Cape Young Chemists' Symposium 2019** was held on 17 May 2019, at Cape Peninsula University of Technology (CPUT).

3. **SACI/RSC Western Cape Young Chemists' Symposium 2018** was held on 6 April 2018, at University of Cape Town (UCT).

4. **NPEP [Symposium on Nanotechnology and Energy in South Africa**], was held on the 26 October 2017, Venue: SAASTA Auditorium, Didacta Building, 211 Nana Sita Str. Pretoria

ABSTRACT

Electrochemically enhanced iron doped lithium manganese phosphate ($LiFe_{0.5}Mn_{0.5}PO_4$)-multi-walled carbon nanotube cathode system

Lithium iron manganese phosphate ($LiFe_{0.5}Mn_{0.5}PO_4$), is a promising, low cost and high energy density (700 Wh/kg) cathode material with high theoretical capacity and high operating voltage of 4.1 V vs. Li/Li^+, which falls within the electrochemical stability window of conventional electrolyte solutions. However, a key problem prohibiting it from large scale commercialization is its severe capacity fading during cycling. The improvement of its electrochemical cycling stability is greatly attributed to the suppression of Jahn-Teller distortion at the surface of the $LiFe_{0.5}Mn_{0.5}PO_4$ particles. Nanostructured materials offered advantages of a large surface to volume ratio, efficient electron conducting pathways and facile strain relaxation. The $LiFe_{0.5}Mn_{0.5}PO_4$ nanoparticles were synthesized via a simple-facile microwave method followed by coating with multi-walled carbon nanotubes (MWCNTs) nanoparticles to enhance electrical and thermal conductivity. The pristine $LiFe_{0.5}Mn_{0.5}PO_4$ and $LiFe_{0.5}Mn_{0.5}PO_4$-MWCNTs composite were examined using a combination of spectroscopic and microscopic techniques along with electrochemical techniques such as cyclic voltammetry (CV) and electrochemical impedance spectroscopy (EIS). Microscopic results revealed that the $LiFe_{0.5}Mn_{0.5}PO_4$-MWCNTs composite contains well crystallized particles and regular morphological structures with narrow size distributions. The composite cathode exhibits better reversibility and kinetics than the pristine $LiFe_{0.5}Mn_{0.5}PO_4$ due to the presence of the conductive additives in the $LiFe_{0.5}Mn_{0.5}PO_4$-MWCNTs composite. For the composite cathode, $D = 2.0 \times 10^{-9}$ cm^2/s while for pristine $LiFe_{0.5}Mn_{0.5}PO_4$ $D = 4.81 \times 10^{-10}$ cm^2/s. The charge capacity and the discharge capacity for $LiFe_{0.5}Mn_{0.5}PO_4$-MWCNTs composite were 259.9 mAh/g and 177.6 mAh/g, respectively, at 0.01 V/s. The corresponding values for pristine $LiFe_{0.5}Mn_{0.5}PO_4$ were 115 mAh/g and 44.75 mAh/g, respectively. This was corroborated by EIS measurements. $LiFe_{0.5}Mn_{0.5}PO_4$-MWCNTs composite showed to have better conductivity which corresponded to faster electron transfer and therefore better electrochemical performance than pristine $LiFe_{0.5}Mn_{0.5}PO_4$. The composite cathode material ($LiFe_{0.5}Mn_{0.5}PO_4$-MWCNTs) with improved electronic conductivity holds great

promise for enhancing electrochemical performances and the suppression of the reductive decomposition of the electrolyte solution on the $LiFe_{0.5}Mn_{0.5}PO_4$ surface. This study proposes an easy to scale-up and cost-effective technique for producing novel high-performance nanostructured $LiFe_{0.5}Mn_{0.5}PO_4$ nano-powder cathode material.

TABLE OF CONTENTS

LIST OF FIGURES

Figure ***Description*** ***Page***

LIST OF TABLES

Table ***Description*** ***Page***

LIST OF SCHEMES

LIST OF ABBREVIATIONS

CV: Cyclic voltammetry

EIS: Electrochemical Impedance spectroscopy

XRD: X-ray diffraction

SEM: Scanning electron microscopy

EDS: Energy dispersive x-ray spectroscopy

TEM: Transmission electron microscopy

HRTEM: High resolution transmission electron microscopy

$LiMnPO_4$: Lithium manganese phosphate

$LiFePO_4$: Lithium iron phosphate

MWCNTs: Multi-walled carbon nanotubes

SAXS: Small-angle X-ray scattering

LiMnFePO4-MWCNTs: Lithium iron manganese phosphate coated with multi-walled carbon nanotubes

CHAPTER 1
INTRODUCTION

1. Background

At the start of the 21st century, combustion of hydrocarbons remains the popular energy source for transportation, but the rate of global warming and projected limits in oil supply require a sustainable alternative (Ma *et al.,* 2012). Electrochemical energy conversion devices such as fuel cells, and electrochemical storage devices such as batteries and supercapacitors, represent an array of devices alternative to the combustion engine. Battery technology has found commercial use in the form of electric and hybrid electric vehicles (EV/HEV). These battery systems, lithium-ion (Li-ion) battery technology offers, the greatest development potential for electric vehicles and advanced energy storage of clean electricity, but increased power density is desired for high power applications Ma *et al*., *2013*). Higher power allows for shorter charging times, which is an important aspect for those considering a switch from a combustion-powered vehicle to an EV. Increased power density will decrease Li-ion battery charging time. Specific power is the product of voltage and specific current. In addition, the increase can be achieved by selecting positive and negative materials which lead to a higher voltage and by increasing overall charge/discharge rates. Replacing the conventional microparticles of the positive electrode material with nanoparticles significantly enhance the electrode/electrolyte interface area which improves overall charge/discharge rates (Ding, Su and Tian., 2016).

In comparison with other batteries, lithium-ion batteries are by far the only batteries which offer the highest energy density (Ding and Tian., 2016; Yang *et al.,* 2013). Their small size and low weight make them ideally suitable for portable electronic devices. Their high energy density offers a promising future for them being applied in a variety of energy storage systems, ranging from small, portable electronics to electrical hybrid vehicles as well as in advanced storage systems such as standby power grid (Aurbach *et al,* 1997). However, these batteries have low power density and because of this their applications are restricted (Ariga *et al*, 2012).

Research on rechargeable Li-ion batteries for electric and hybrid electric vehicles have generated a lot of interest over the years (Zaban *et.al.*, 2016). The development of new cathode materials amongst others holds the key to the improvement of the capacity, rate capability and cyclability of these batteries. Lithium iron manganese phosphate ($LiFe_{0.5}Mn_{0.5}PO_4$) has been shown to be the most promising cathode material based on its low cost and non-toxicity (Cao *et al.*, 2004). The $LiFe_{0.5}Mn_{0.5}PO_4$ has a cubic structure with space group symmetry Pbnm (62) in which the PO_4, $Fe^{3+/2+}$ and $Mn^{3+/2+}$ ions which are in the 8a tetrahedral site and 16-d octahedral site, respectively.

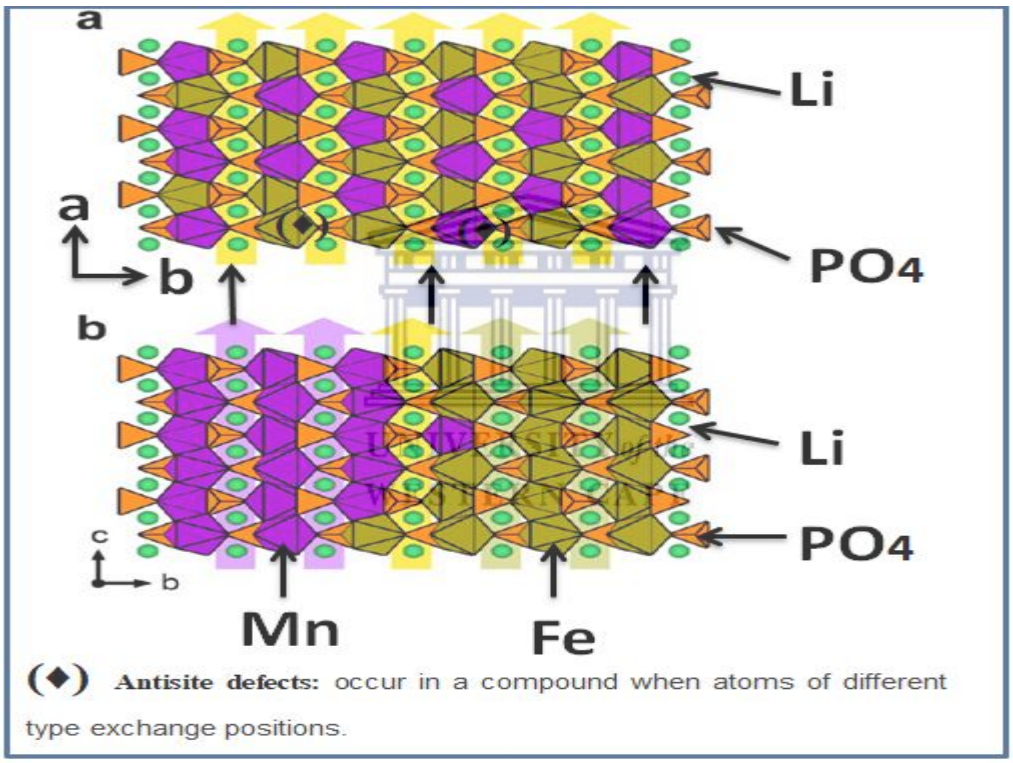

Scheme 1: The $Fe_{0.5}Mn_{0.5}PO_4$ shows the cubic structure with anti-site defects.

The $Fe_{0.5}Mn_{0.5}PO_4$ spinel framework provides a three-dimensional interstitial space for the reversible insertion of lithium ions. $LiFe_{0.5}Mn_{0.5}PO_4$ however suffers from severe capacity fading especially in high temperatures due to disproportionation reaction and Jahn-Teller effect. However, functionalization of $LiFe_{0.5}Mn_{0.5}PO_4$ is recognized as an effective method

to modify the conductivity, stability and control its physicochemical properties (Chan, 2005). Enormous efforts have been made in recent years to overcome these problems by cationic doping, decreasing the particle size through various synthesis methods, (Chan, 2003; Churikov *et al,* 2009*)* and coating with electronically conducting agents (Dahn *et al, 1994)*. Particularly, nanosized $LiFe_{0.5}Mn_{0.5}PO_4$ particles have been shown to exhibit excellent performance with high rate capability due to a shortening of both the electron and lithium ion diffusion path lengths within the particles (Doeff., 2013). In this regard, dimensionally modulated nanostructures such as nanotubes, nanorods, nanowires, and nanosheets are appealing as they can efficiently transport charge carriers while maintaining a large surface to volume ratio, enhancing the contact with the electrolyte and the reaction kinetics. Hence, nanomaterials have been confirmed to be a new effective material for protecting electrode from dissolution (Fergus, 2010). Recently, several reports have focused on the effect of surface modification of $LiFe_{0.5}Mn_{0.5}PO_4$ by nanomaterials such as AlF_3 nanoparticles on electrochemical performance at higher cut-off voltage up to 4.1 V (Hu *et.al.,* 2018). The aluminium tri-flouride (AlF_3) coating layer, which reduces the formation of lithium fluoride (Li-F) film that increases the cathode/electrolyte interfacial impedance and suppresses manganese (Mn) dissolution by covering $LiFe_{0.5}Mn_{0.5}PO_4$. The surface from hydrogen fluoride (HF) attack which improves the capacity retention $LiFe_{0.5}Mn_{0.5}PO_4$ at 4.1 V cut-off cycling. In is study, the poor electrochemical performance of $LiFe_{0.5}Mn_{0.5}PO_4$ has been enhanced by (1) reducing the particle size to the sub-micrometer scale and (2) functionalization with conducting multi-walled carbon nanotubes, thereby diminishing electric and Li-diffusion resistances by shortening the distances for electron and lithium transport.

1.1 Problem statement

The olivine lithium iron manganese phosphate is an outstanding cathode material for lithium ion battery due to its superior redox potential at 4.1 V vs. Li/Li^+ (due to lithium manganese phosphate) and at 4.1 V vs. Li/Li^+ (due to lithium iron phosphate), when compared with the already commercialized olivine $LiFePO_4$ (3.5 V), layered $LiCoO_2$ (4.5 V) and spinel $LiMnO_4$ (4.1 V). However, it has extremely low electronic and ionic conductivities caused by huge volume change between $LiMnPO_4$ and $LiFePO_4$ during intercalation; and poor electronic conductivity limits its application. This work focused on

enhancing the stability and electron transport within the cathode material. This was done through decreasing the particle size, and surface modification resulting in a change of electrode potential (thermodynamics of the reaction). Nanomaterials provide new reactions which are not possible with only bulk materials. In this research project $LiFe_{0.5}Mn_{0.5}PO_4$ cathode material will be prepared by coating with multi-walled carbon nanotubes thereby enhancing its conductivity. The electrochemical characterization of the prepared materials will be conducted by employing electrochemical impedance spectroscopy (EIS) and cyclic voltammetry (CV). The proposed composite cathode material ($LiFe_{0.5}Mn_{0.5}PO_4$-MWCNTs) with improved electronic conductivity holds great promise for enhanced electrochemical performances, discharge capacity, cycle performance and suppression of the reductive decomposition of the electrolyte solution on the $LiFe_{0.5}Mn_{0.5}PO_4$ surface.

1.2 *Aim and objectives*

The research aim is to develop a novel lithium ion cathode systems with enhanced electrochemical properties that will fit the characteristics (high capacity, safety and low cost) required in the modern lithium ion batteries for applications not only in portable devices but also in controlled emission vehicles, so as to protect the environment challenges and threats caused by CO_2 emission from fossil fuel in internal combustion engines. This thesis focused on the following objectives:

(i) Preparation and microscopic analysis of the lithium iron manganese phosphate ($LiFe_{0.5}Mn_{0.5}PO_4$) and multi-walled carbon nanotubes (MWCNTs) composite.

(ii) Preparation and microscopic analysis of lithium iron manganese ($LiFe_{0.5}Mn_{0.5}PO_4$)

(iii) Determination of their voltammetry, impedimetric and charge/discharge properties.

1.3 Outline of the thesis

This thesis comprises six (6) chapters and is structured as follows:

Chapter one

This chapter gives us an introduction of different cathode materials used for Li-ion batteries but mostly focussed on $LiFe_{0.5}Mn_{0.5}PO_4$ as well as the different dopants such as nanomaterial that have been done to improve its electrochemical performance. The aim and objectives are also stated in this chapter.

Chapter two

This chapter gives a literature review relating to the definition of Li-ion batteries, its main components. A better understanding of $LiFe_{0.5}Mn_{0.5}PO_4$ as well as nanomaterial will be presents in this section.

Chapter three

The method used for the synthesis of $LiFe_{0.5}Mn_{0.5}PO_4$, multi-walled carbon nanotubes (MWCNTs) coated lithium iron manganese phosphate ($LiFe_{0.5}Mn_{0.5}PO_4$) as well as the instrumentation technique and characterization used are fully detailed in this section. The results found for the synthesized $LiFe_{0.5}Mn_{0.5}PO_4$, and commercially purchased MWCNTs are presented and discussed in this chapter.

Chapter four

The results found for the synthesized MWCNTs coated $LiFe_{0.5}Mn_{0.5}PO_4$ are presented and discussed in this chapter.

Chapter five

This section displays electrochemistry and discussion obtained for the novel $LiFe_{0.5}Mn_{0.5}PO_4$, and MWCNTs coated $LiFe_{0.5}Mn_{0.5}PO_4$.

Chapter six

Finally, this chapter will present the conclusion as well as recommendations.

Reference

This section is ascribed to the references that were used for this thesis.

1.4 Thesis Structure

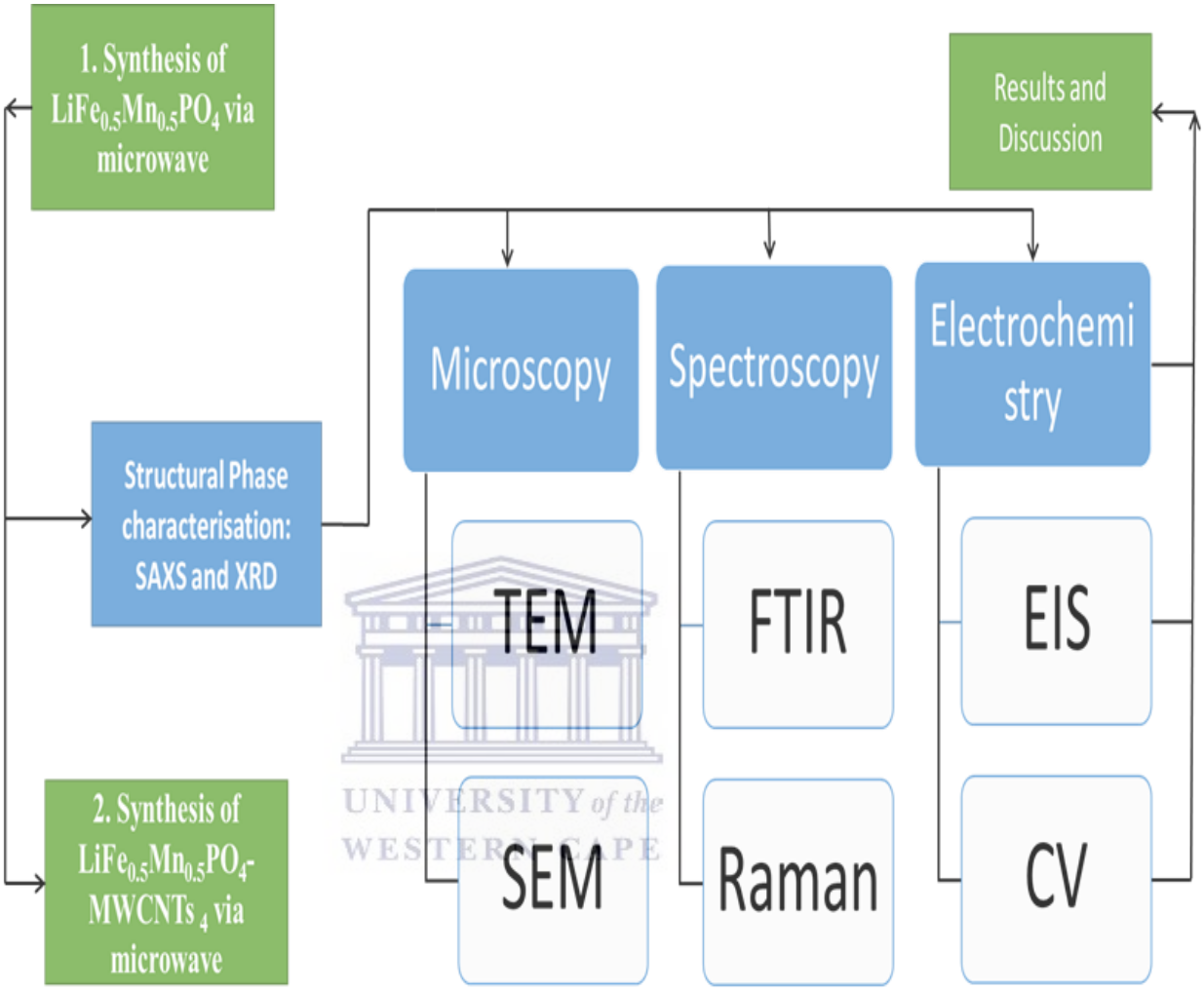

Scheme 2: Conceptual diagram of Thesis

CHAPTER 2
LITERATURE REVIEW

2. Background

Batteries can be regarded as unit cells containing chemical energy that can be converted into electrical energy (Hu *et.al,* 2013). These cells are bounded in a case to form a battery unit. A battery pack is then defined as an assembly of these separate battery units that are connected in a series and parallel grouping to deliver the expected voltage and energy to the power storage system. The stored energy in a battery is the difference in free energy between chemical components in the charged and discharged states. This available chemical energy in a cell is converted into electrical energy only on demand, using the basic components of a unit cell. The electrochemically active constituent of the positive or negative electrode is called the active material. The redox reaction takes place at the two electrodes, resulting in a bonding and releasing of electrons. The electrodes must be electronically conducting, and they are positioned at diverse sites, a separator plays the role of splitting them. Throughout battery process, electrons flow from one electrode to another (Doeff, 2013). Nevertheless, this flow of electrons in the cell is maintainable only if electrons that are generated during the chemical reaction are capable to pass through an external electrical circuit that links those two electrodes. The battery terminals are regarded as joining points among the two electrodes and the external circuit. On the other hand, external circuit make sure that most of the chemical energy that is stored is released only on demand and is used as electrical energy (Doeff, 2013). Batteries are divided into two different types: primary batteries defined as those that cannot be recharged for examples lithium batteries used in clocks, cameras etc. The other type is secondary batteries; these are rechargeable and can be reuse. The examples of these rechargeable batteries are: Lead-acid, Nickel-cadmium, Lithium-ion, Zinc-air, Lithium-polymer, Sodium-sulphur batteries**. Scheme 3** is a representation of Ragone plot showing different energy devices and their relative power and energy.

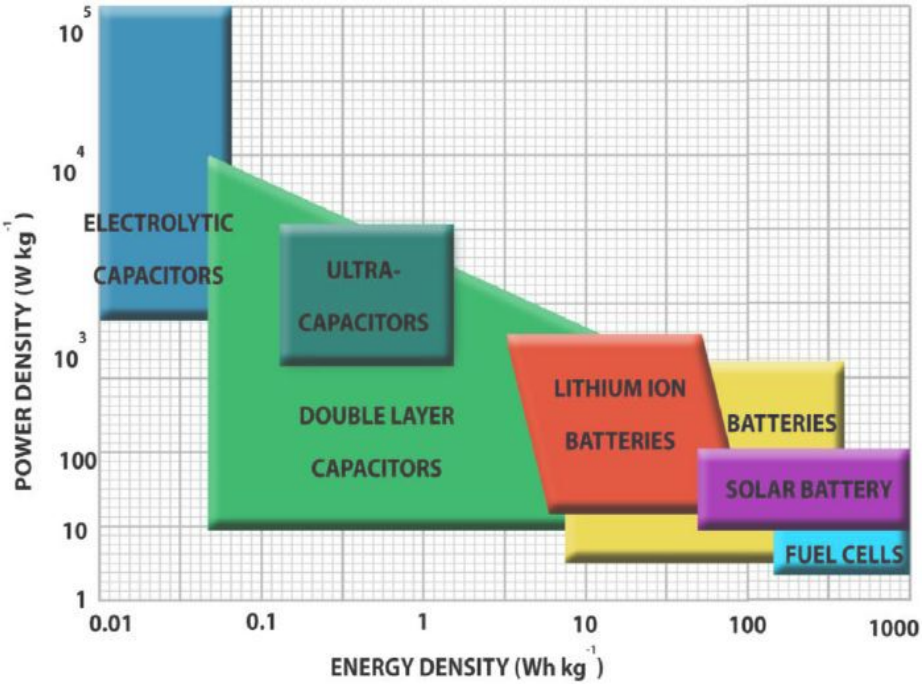

Scheme 3: Ragone plot, showing different energy storage systems and their relative power and energy (Hu *et al.,* 2013).

2.1 The operation principle and battery technology.

Batteries are electrochemical devices that produce energy by converting chemical energy into electrical energy to power a variety of applications by using electrochemical redox reactions which occur at the anode and cathode (Hadjipaschalis *et al.,* 2009). The fundamental part of a battery is the electrochemical cell which consists of three main components: the electrodes: cathode and anode; and the electrolyte. The anode is where oxidation chemical reaction takes place in a cell; electrons are donated to an external circuit, a good anode material should be efficient as a reducing agent with good conductivity, stability, easy to fabricate and at low cost. Basically, metals are used as the anode material. The cathode is where reduction chemical reactions take place in a cell; it accepts electrons from the external circuit, the cathode material must be an efficient oxidizing agent, have a useful working voltage and show good stability when in contact with the electrolyte (Winter *et al.,* 2005). Common cathode materials are metal oxides. An electrolyte is a material that provides pure ionic conductivity between the anode and cathode of a cell. Its main function is to provide a transport medium for ions to travel from one electrode to the other. It must also prevent short- circuiting by acting as a physical barrier between the electrodes. The electrolyte should not undergo any net chemical changes during the operation of the battery. Batteries are one of the electrochemical energy storage devices which have found many applications in the market (Winter *et al.,* 2005). Batteries are classified as

primary or secondary depending on their capability of being electrically recharged. The classification of batteries differs with chemicals as well as the operation of a battery. The chemical idea works by having two different chemicals in a battery which have different loads and relate to a negative (cathode) and the other with a positive electrode (anode) (Winter *et al.,* 2005). Mainly the negative electrode supplies a current of electrons that flow through the appliance and are accepted by positive electrode, which can be used in appliances.

2.2 Batteries components

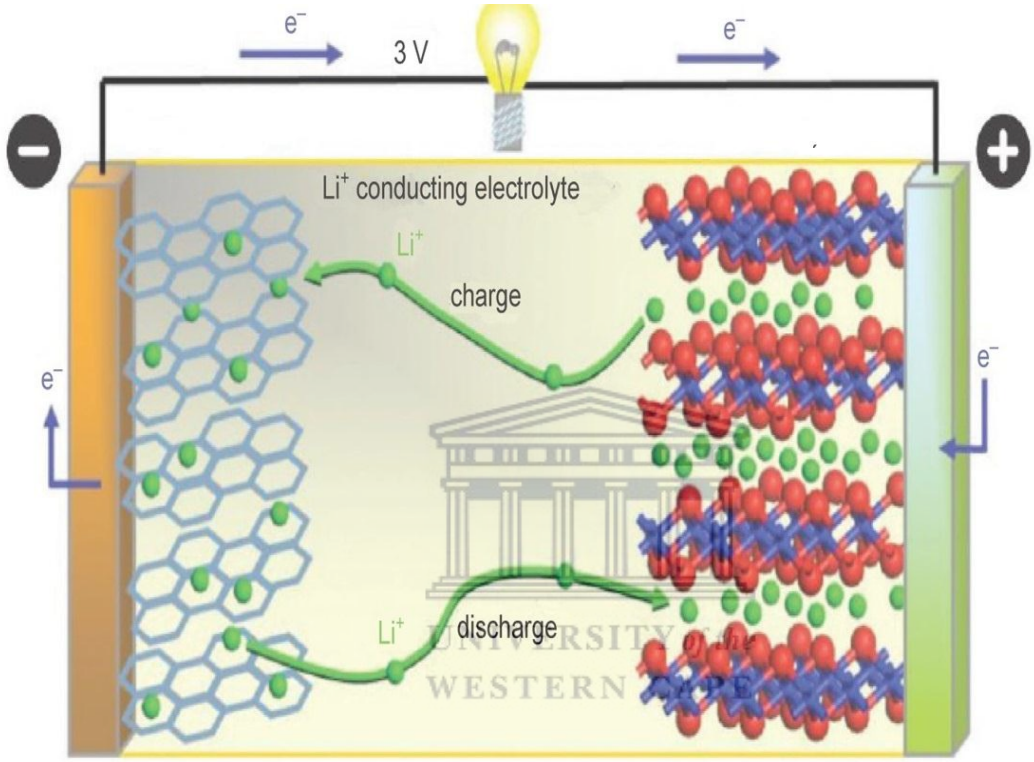

Scheme 4: Li-ion battery (Meng *et al.,* 2009)

2.2.1 Positive electrode

The positive electrode can be defined as an oxide or sulphide or some other compound that can easily be reduced through cell discharge. This electrode consumes electrons from the external circuit during cell discharge. Examples of positive electrodes are lead oxide (PbO_2) and nickel oxyhydroxide (NiOOH). The electrode materials are in the solid state (Husain., 2011).

2.2.2 Negative electrode

The negative electrode is a metal or an alloy that is adept of being oxidized through cell discharge. This electrode generates electrons in the external circuit during cell discharge.

Examples of negative electrodes are led (Pb) and cadmium (Cd). Negative electrode materials are also in the solid state within the battery cell (Husain, 2011).

2.2.3 Electrolyte

The electrolyte is the medium that allows the conduction of ions between the positive and negative electrode of a cell. The electrolyte must have high and selective conductivity for the ions that take part in electrode reactions, but it must be a non-conductor for electrons in order to avoid self-discharge of batteries. The electrolyte can either be solid material, liquid or gel. In addition, the electrolyte can be acidic or alkaline, depending on the type of battery. Traditional batteries such as lead-acid and nickel-cadmium use liquid electrolytes. In lead-acid batteries, the electrolyte is the aqueous solution of sulphuric acid [H_2SO_4(aq)]. Advanced batteries currently under development for EVs, such as sealed lead-acid, nickel-metal-hydride (NiMH), and lithium-ion batteries utilizes an electrolyte that can either be gel, paste or resin. Lithium-polymer batteries use a solid electrolyte (Husain., 2011).

2.2.4 Separator

The separator can be regarded as an electrically insulating layer of material that is able to essentially separate electrodes of opposite polarity. Separator has to allow the flow of ions of the electrolyte and may also play the role of storing or allow the electrode to immobilize easily (Husain, 2011).

2.3 Lithium-ion Batteries

Lithium as a metal is known to have a high electrochemical reduction potential (3.045 V) and the lowest atomic mass (6.94), which shows promise for a battery of 3 V cell potential when combined with a suitable positive electrode. The interest towards secondary lithium cells soared soon after the arrival of lithium primary cells in the 1970s, although the main challenge was the highly reactive nature of the lithium metal with moisture, restricting the use of liquid electrolytes. But late in the 1970s, it was revealed by researchers at Oxford University that lithium can be intercalated (absorbed) into the crystal lattice of cobalt or nickel to form $LiCoO_2$ or $LiNiO_2$ tiled the way toward the development of Li-ion batteries (Starke *et al*, 2017*)*. The use of metallic-lithium is bypassed in Li-ion batteries by using lithium intercalated (absorbed) carbons (Li_xC) in the form of graphite or coke as the negative electrode, alongside with the

lithium metallic oxides as the positive electrode. The graphite has the capacity of hosting lithium up to a composition of LiC_6. Most of Li-ion batteries make use of cobalt as positive electrode, though it is expensive but has proven to be the most adequate. Other alternative positive electrode such as nickel oxide $LiNiO_2$, is known to have a complex structure and is cost effective. Although, $LiNiO_2$ has similar performance, when compared to lithium oxide electrode. Another positive electrode is known as manganese oxide based ($LiMn_2O_4$ or $LiMnO_2$) which are also under investigation, because manganese is less toxic, cheaper, and broadly available (Doeff, 2013). **Scheme 5** displayed below is a representation of a Li-ion battery.

2.4.1 Lithium-ion batteries charge / discharge process

The charge / discharge process is illustrated below:

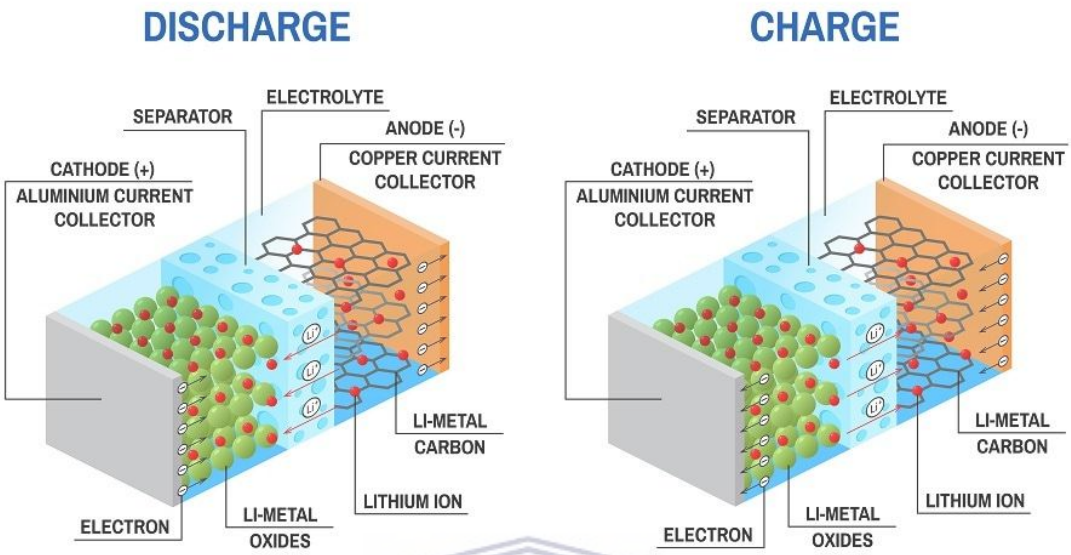

Scheme 5: Schematic representation for the charge / discharge process of Lithium-ion batteries (Bazito *et al.,* 2006)

2.4.1.1 Charge process

During cell charge, lithium ions move in the opposite direction from the positive electrode to the negative electrode. The nominal cell voltage for a Li-ion battery is 3.6 V, which is equivalent to three NiMH or NiCd battery cells.

2.4.1.2 Discharge process

During cell discharge, lithium ions (Li^+) are released from the negative electrode that travels through an organic electrolyte toward the positive electrode. In the positive electrode, the lithium ions are quickly incorporated into the lithium compound material. The process is completely reversible.

2.4.2 Primary batteries

Primary batteries are not rechargeable. They are discharged once and discarded, and this is since reactions at the electrodes are not reversible. They are convenient and cost less per battery, with the downside of costing more over the long term (Winter *et al.,* 2005). The disadvantage is that they have short lifetime with uneconomical energy sources since they only produce 2% of the power used in their manufacture. Examples include zinc-alkaline-manganese-dioxide (the leclanche' cell), zinc-mercuric-oxide, zinc-silver oxide, zinc-air, magnesium-manganese dioxide and primary lithium batteries. These types of batteries are losing market share to newer technology therefore, there is not much current research going on in this area hence the need for other alternatives that can be used time and time again. In this report the focus is on rechargeable batteries, which have found a lot of interest recently in the past decade for storing energy efficiently and having long lifetime.

2.4.3 Secondary batteries

Secondary batteries are reversible in electrochemical reactions and the cells are rechargeable. They have higher initial cost but their maintenance in terms of recharging is very cheap and they can be used many times. They have found a lot of applications in automotive and aircraft systems, emergency no-fail and standby (UPS) power sources, hybrid electric vehicles and stationary energy storage (SES) systems for electric utility load levelling. They are also used in portable consumer electronics, power tools and electric vehicles. Examples include lead-acid, nickel cadmium (NiCd), nickel metal hydride (NiMH), lithium ion (Li-ion) and lithium ion polymer (Li-ion polymer) batteries.

2.4.3.1 Lead-acid batteries

They are the oldest known type of rechargeable battery which was invented in 1959 by French physicist Gaston Plante' (Rand *et al.,* 2015). After over 150 years of the concept, lead-acid batteries are still been used due to their cost-effectiveness. Today, they are used widely in motor vehicles (automobile starter motors), wheelchairs and golf carts (Moseley *et al.,* 2009). Lead-acid batteries have large power-to weight ratio that is why they can

supply high surge current in large scale. Lead-acid designs can be used for storage backup power supplies in cell phone towers, high availability settings like hospitals, and stand-alone power systems (Moncada *et.al.,* 2014). Lead-acid batteries like any other electrochemical cell are based on chemical reactions with the use of lead dioxide as the cathode, lead as the anode electrode and sulphuric acid as the electrolyte (Brodd *et al.,* 2005) The energy density of lead-acid is around 30 Wh/kg with power density around 180 W/kg and the rated voltage is 2 V delivered from several in-series connection of the cells (Moncada *et.al.,* 2014). During the discharge operation of the lead acid battery, the anode and cathode undergo a chemical reaction with the electrolyte and yield a change to lead sulphate that releases electrical energy in the process. The reaction is completely reversed by simply supplying the electrodes with electricity, which is why lead-acid battery can be recharged. Reaction occurring at lead-acid battery:

During discharge

Anode reaction

$Pb(s) + HSO_4^-(aq) \rightarrow PbSO_4(s) + H^+(aq) + 2e^-$ (**1**)

Cathode reaction

$PbO_2(s) + HSO_4^-(aq) + 3H^+(aq) + 2e^- \rightarrow PbSO_4(s) + 2H_2O$ (**l**) (**2**)

Overall reaction

$Pb(s) + PbO_2(s) + 2H_2SO_4(aq) \rightarrow 2PbSO_4(s) + 2H_2O$ (**l**) (**3**)

During charge

Anode reaction: $PbSO_4(s) + H^+(aq) + 2e^- \rightarrow Pb(s) + HSO_4^-(aq)$ (**4**)

Cathode reaction: $PbSO_4(s) + 2H_2O(l) \rightarrow PbO_2(s) + HSO_4^-(aq) + 3H^+(aq) + 2e^-$ (**5**)

They have between 85% and 90% of energy efficiencies; require low level of maintenance and low investment cost. Self-discharged rates are around 2% of rated capacity per month (at 25 °C) (Winter *et al.,* 2005). Their drawbacks are that they have relatively low cycle life and battery operational lifetime; have a lifetime which is between 1200 and 1800 charge/discharge cycles or operate for 5-15 years. The depth of discharge and temperature negatively affect the cycle life. Electrode can be damaged by attempts to fully discharge the battery, thus reducing lifetime (Moncada *et.al.,* 2014). Regarding temperature levels, using high temperatures like 45 °C which is the maximum limit for battery operation can

improve performance of battery by increasing capacity but also, they can reduce battery lifetime as the battery energy efficiency.

2.4.3.2 Nickel based batteries

Nickel based batteries are generally the nickel-cadmium (NiCd), the nickel-metal hydride (NiMH) and the nickel-zinc (NiZn) batteries. These three nickel-based batteries that use the same material for the positive electrode which is nickel hydroxide and the electrolyte which is an aqueous solution of potassium hydroxide with lithium hydroxide, respectively (Hadjipaschalis *et al.*, 2009). They use a different material for the negative electrode, while NiCd uses cadmium hydroxide, NiMH uses a metal alloy and NiZn uses zinc hydroxide. The energy density of NiCd is 50 Wh/kg; 80 Wh/kg for NiMH and 60 Wh/kg for NiZn which is higher than lead-acid batteries and the rated voltage for the alkaline batteries is 1.2 V (1.65 V for the NiZn) (Hadjipaschalis et al., 2009). NiCd batteries life and cycle life ranges from 1500 cycle for the pocket plate vented type to 3000 cycles for the sinter vented type which is superior to lead-acid batteries but NiMH and NiZn have lower or similar to lead-acid battery (Hadjipaschalis *et.al.*, 2009). The nickel-based battery has struggled to penetrate the market in terms of industrial use or for use in supporting renewable energy power systems compared to lead-acid batteries. The cost of NiCd batteries is 10 times higher than the lead-acid battery, which works against the use of this type of battery. The energy efficiencies of nickel-based batteries are also lower than that of lead-acid. NiMH has 60 – 70% and NiZn has 80% efficiency. For the NiCd batteries, the efficiency varies depending on the type of technology used during manufacture (Shukla *et.al.*, 2001), but these values are lower than of lead-acid batteries.

2.4.3.3 Lithium ion polymer (Li-ion polymer)

Lithium ion polymer batteries are usually made up of several identical secondary cells which are arranged in parallel to increase the discharge current capability. They have high energy density which ranges from 100-150 Wh/kg and energy efficiencies which are between 90- 100%. Lithium polymer has power density which ranges from 50-250 W/kg and the lifetime is about 600 cycles (Hadjipaschalis *et.al.*, 2009). This type of battery has found wide applications in mobile phones and other portable electronics.

2.5 Cathode functionality of lithium ion batteries

A cathode in general electrochemistry is the electrode where reduction occurs. Cathodes are typically oxides of transitions metals. They are the sources of lithium ion in lithium ion batteries (Wang *et al.,* 2006). These materials can be divided into three categories: (a) layered oxides (b) Spinels and (c) Olivines. The layered transition metal oxides of formula $LiMO_2$ (M= V, Cr, Fe and Ni) consist of empty spaces between the MO_2 layers that can accommodate lithium ions (Whittingham, 2004). One example of this type of cathode material is lithium cobalt oxide ($LiCoO_2$). Layered $LiCoO_2$ is commercially used and is a successful cathode material because it has capacities which is 280 mAh/g and can be larger with 3.6 V and can have larger operating voltages when it is charged to over 4.6 V at room temperature (Kim *et.al.,* 2008). This is unstable compared to other potential electrode materials and can suffer from performance degradation or failure when overcharged. The other disadvantage is that cobalt costs more than the other transition metals. The spinel and olivine are made up of three-dimensional structures with cross-linked channels that are sufficiently large to allow insertion (Whittingham, 2004). Spinel have good structural stability; an example is lithium manganese oxide ($LiMn_2O_4$); a low cost and environmentally friendly material with a charge storage capacity which is 148 mAh/g. It has high abundance and is a promising candidate to replace layered Ni or Co oxide cathode materials for lithium ion batteries (Manthiram *et.al.,* 2008). However, its application is limited due to poor capacity retention during cycling and storage as a result of manganese dissolution in the electrolyte. The phosphates, $LiMPO_4$ (M = Fe, Mn, Co, Ni) with the olivine structure, are a very promising class of cathode materials. The commonest among them is $LiFePO_4$. This material occurs in nature as the mineral, triphylite and crystallizes in the olivine structure. It has low cost and is environment friendly (Chen, 2013) with a flat discharge potential at about 3.4 V vs. lithium and a capacity of 170 mAh/g which is higher than that of $LiCoO_2$ and comparable to stabilized $LiNiO_2$. $LiFePO_4$ is much more stable during discharge/charge and with no sign of capacity fading after several cycles (Novikora *et.al.,* 2013). However, it has a low electronic and a low ionic conductivity which hampers its electrochemical activity. Work is still ongoing in order to improve its electrochemical performance during charge/discharge cycling.

2.5.1 Lithium manganese phosphate ($LiFePO_4$) cathode material

$LiFePO_4$ occurs in nature as the mineral, crystallizes in the olivine structure with the pnmb space group (Padhi and Goodenough, 1997) having cell parameters; a = 6.008 Å; b = 10.334 Å; c = 291.392 Å with a volume of the unit lattice as 291.392 Å. The central Fe atom together with the surrounding oxygen atoms forms the FeO_6 octahedron which shares edges with two LiO_6 octahedrons and one PO_4 tetrahedron. Lithium ion reside within the octahedron channel in the three-dimensional zigzag framework formed by the corner shared FeO_6 octahedral and edge shared PO_4 tetrahedral as depicted in the **Scheme 5**. The presence of heavier PO_4 groups prevents free movement of Lithium ions to a one-dimensional pattern. $LiFePO_4$ has an exceptionally flat discharge potential at about 3.4 V vs. lithium with a capacity of 170 mAh/g, which is comparable to that of stabilized $LiNiO_2$ but higher than that obtained for $LiCoO_2$. delithiation of $LiFePO_4$ results in the $FePO_4$, in which the Fe^{2+} ions are oxidized to Fe^{3+} leaving the 3D olivine framework intact. Thus, there is no structural change upon lithium extraction/insertion. There is a slight variation in lattice parameters is observed. The excellent reversibility of the cells is due to the striking similarity of the two structures as shown in **scheme 6**.

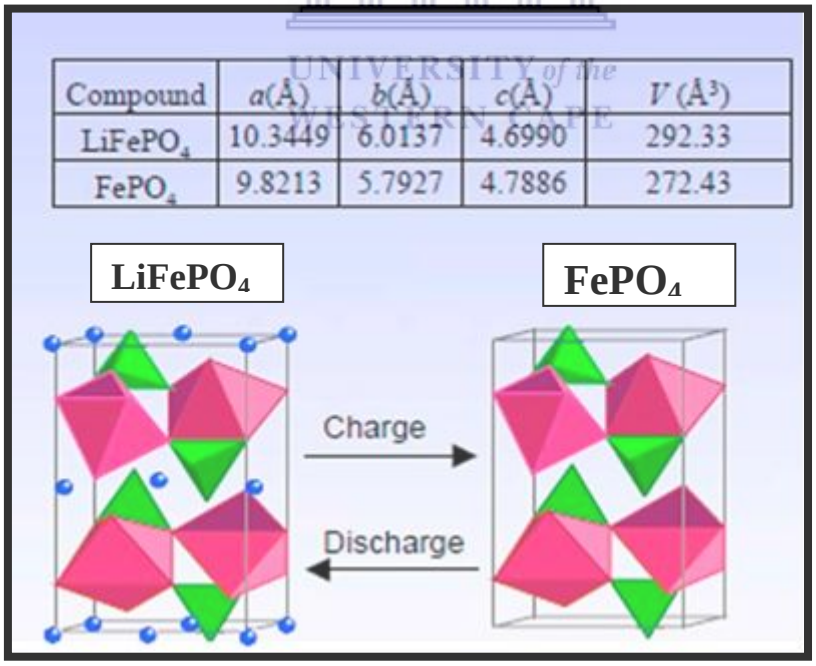

Scheme 6: Crystal structures of (a) $LiFePO_4$ and (b) $FePO_4$ consisting of FeO_6 octahedral and PO_4 tetrahedral. The circles represent lithium ions (Wang *et al.*, 2011).

This structural stability imparts a good cycle life on $LiFePO_4$ cells as there is no obvious capacity fade even after several hundred cycles (Wang *et al.*, 2011). In addition to its attractive electrochemical features, it is based on iron, an element that is naturally occurring and abundant, inexpensive and environmentally friendly.

2.5.2 Lithium manganese phosphate ($LiMnPO_4$) cathode material

Lithium manganese phosphate ($LiMnPO_4$) has received much attention for use in lithium ion batteries because it is cheap and environment friendly. South Africa has large deposits of much of the chemical raw materials such as manganese, iron, cobalt, nickel and vanadium, required for the manufacture of lithium ion battery cathode materials. The potential of $LiMnPO_4$ is compatible with $LiCoO_2$, at 4.1 V vs. Li+/Li. It has an excellent cycle performance and thermal stability when compared with the lithium transition metal oxides (Aravindan *et al.*, 2013). **Scheme 7** shows a schematic diagram of $LiMnPO_4$ olivine. It has an olivine structure, where Mn and Li occupy octahedral 4c and 4a sites, and P atom in 4c site, respectively (Bakenov *et al.*, 2011). The O atoms are in a hexagonal close-packed arrangement. The MnO6 octahedral are separated by PO_4 polyanions (Bakenov *et al.*, 2011).

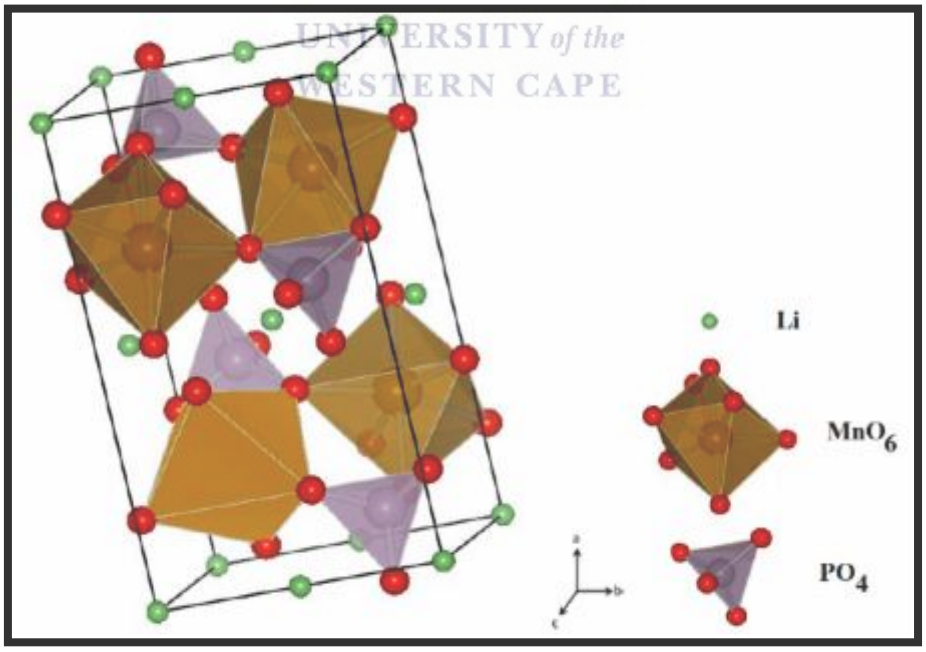

Scheme 7: Structure of the $LiMnPO_4$ with Pnma space group (Bakenov and Taniguchi, 2011).

Phospho-olivines have a makeup where all the oxygen ions form strong covalent bonds with P^{5+} to form PO_4^{3-} polyanion in the tetrahedral and stabilize the entire three-dimensional framework (Pitchai *et.al.,* 2011**).** This gives olivine cathode materials an advantage to work under abusive conditions but still maintain safety due to their improved stability (Yamada *et.al.,* 2003). However, the electrochemical reaction kinetics is restricted in phospho-olivines because of the insulating effect of the polyanion (Bakenov *et al.,* 2011). $LiMnPO_4$ has a theoretical energy density at 701.1 Wh/kg which is attributed to a higher operating voltage plateau and is much higher than that of $LiFePO_4$ at 568.5 Wh/kg. It is compatible with most liquid electrolytes presently used in lithium-ion batteries (Pan *et.al.*, 2013). However, $LiMnPO_4$ shows less or poor electrochemical performance due to slow lithium ion diffusion kinetics within the crystals and very low intrinsic electronic conductivity (Drezen *et al.*, 2007). For the Mn^{2+}/Mn^{3+} redox reaction to occur in $LiMnPO_4$ cathode, high ionic and electronic conductivities are necessary to enable Li^+ diffusion and electron transport (Yamada *et al.,* 2003).

In recent studies, it has been reported that morphology and structure significantly affect the electrochemical performance of $LiFePO_4$. With the development of $LiFePO_4$ paving way for $LiMnPO_4$, it could also be said that morphology and structure might as well affect the electrochemical performance of this material (Bakenov *et al.,* 2011). The improvement of the electrochemical kinetics has been studied and researched by many groups and it has been found that carbon coating and reduced particle size enhance the electrochemical properties of $LiMnPO_4$ (Qin *et al.,* 2012). Nano-sized $LiMnPO_4$ compared with micro-sized $LiMnPO_4$ provides shorter lithium ion diffusion path within a single particle. Several routes have been employed in the synthesis of $LiMnPO_4$ such as solid-state reaction, the polyol process, sol-gel, hydrothermal, solvothermal, precipitation, floating- zone, free-drying and electrostatic spray deposition methods.

2.6 Electrolytes

The electrolyte in electrochemical systems serves as the medium for the transfer of charges, which are in the form of ions, between a pair of electrodes (Whittingham, 2004). Normally the electrolyte is composed of one or more liquid solvents and one or more salts which dissociate and provide the ions. In lithium and lithium-ion batteries, the solvents

used are non-aqueous and aprotic (Xu, 2004). The electrolyte must be compatible with both (Whittingham, 2004) positive and negative electrodes, current collectors, and separator (Whittingham, 2004). It also must be stable in contact with the strong oxidizing / reducing surface of the electrodes (chemically / electrochemically inert) (Xu, 2004). Other important factors to consider are the cost, safety, health, and environmental compatibility. From the electrochemical point of view, electrochemical stability is required, and the ionic conductivity is the most important property, because it is directly connected with the specific power of the cell. The formulation of the electrolyte mostly used in commercially available lithium-ion batteries is a combination of linear and cyclic carbonates as solvents, with the presence of passivating additives, and $LiPF_6$ as electrolyte solute. The high dielectric constant of ethylene carbonate (EC) and its low viscosity (with respect to other cyclic carbonates), makes it a good candidate as electrolyte solvent. The most used linear carbonate is dimethyl carbonate (DMC). $LiPF_6$ is chosen as solute because it has a good balance between conductivity, safety and hazard for health (Scrosati and Garche, 2010). A 1M $LiPF_6$ solution of EC: DMC 1:1 (wt.) has a conductivity of 10.7 mS/cm and it is usable in the temperature range between -20 and 50 °C (Xu, 2004). Apart from $LiPF_6$, $LiClO_4$ can create SEI films with enhanced ionic conductivity because of its relatively low reactivity with moisture. $LiPF_6$ reacts with moisture traces and the hydrolysis gives HF, which forms LiF in the SEI, a poor ionic conductor. Unfortunately, at high current or high temperature, the ClO_4- is not stable. For the purpose of this work, aqueous $LiPF_6$ electrolyte was used.

2.6.1 Aqueous electrolyte

An aqueous electrolyte has a high conductance and makes purification and drying processes during production, less stringent. The costs of aqueous electrolytes are usually much lower than suitable organic electrolytes. It should be further pointed out that the cathode material must be developed for one or the other electrolyte and the porous structure of the electrode must be tailored to the size and the properties of the respective electrolytes. In order to avoid electrolyte depletion during charging, the electrolyte concentration must be kept high. If the electrolyte reservoir is too small compared to huge surface area of the electrodes, performance of the cathode is reduced. Hence, a concentration higher than 0.2 molar are enough (Xu, 2004).

2.6.2 Organic Electrolyte

Organic electrolytes have attracted considerable attention due to their greater electrochemical stability (>3 V) compared to aqueous systems (1 V) (Xu, 2004). The wider voltage window offered by non-aqueous electrolytes provides increased energy. However, limitation of the power capability of non-aqueous electrolyte is their inherent lower conductivity (Xu, 2004). In addition, capacitance is also sensitive to the electrolyte concentration. Ionic liquids based on immidazolium salts are solidified or crystallized at below room temperature and have been applied to numerous electrochemical, photovoltaic, and synthetic fields (Xu, 2004).

2.7 Surface modification by doping and coating

Doping is the addition of quantities of an element of a semiconductor for modulating the electrical properties of the material being modified or to change its characteristics. Lightly doped semiconductors are referred to as extrinsic, while semiconductors doped to such high levels that act more like a conductor than a semiconductor is called a degenerate (Chen, 2012). Doping can also be referred to as the activation of a material. The surface of a material can be modified through surface doping. Doping helps to reduce manganese dissolution in $LiMnPO_4$ by decreasing the apparent contact area with the electrolyte **(**Liu *et al.,* 2013). Surface coating is effective in improving the capacity retention, rate capability and even thermal stability of cathode materials for lithium ion batteries (Chen *et al.*, 2010). Different coating materials have been used for cathode materials such as carbon, metal oxide, metal carbonates, and metal phosphates as well as cathode materials with lower reactivity towards non-aqueous electrolytes (Fu *et al.,* 2006). Carbon coating has shown ability to improve performance, mostly for phosphate-based materials. Coating the surface of cathode materials can give improved electron transfer through the interface of the material's particles and therefore accelerate the heterogeneous charge transfer process on the cathode surface Coating also provides extra electro conducting pathways in the cathode material (Pitchai *et al.,* 2011). The surface coating acts as a protective layer to prevent direct contact of the active core material with the electrolyte solution (Chen *et al.,* 2010).

2.8. Nanomaterials and toxicity

Nanomaterials are structures with dimensions in the nanoscale range, normally between 1 and 100 nm. The chemical and physical properties of substances can be considerably altered and fine-tuned when they exist on a nanoscopic scale. An increase in the specific surface area is one of such changes that could occur when the particle size of a material is scaled down to nanometer dimensions (Zhang *et al.*, 2013). Nanotechnology has made it possible to control the particle size and apply electrically conductive coatings to improve the property of the material (Pei *et al.*, 2013). Typical applications of nanomaterials include energy conversion, electrochemistry, catalysis and environmental chemistry, where the use of nanomaterials increases efficiency, sensitivity and response time. There are several potential advantages of nanomaterials in lithium ion battery such as: significant increase in the rate of lithium insertion/removal due to the reduced dimensions of nanomaterials; enhancement in the rate capacity as well as the cycle life (Zhang *et al.*, 2013). Electron transport is also enhanced by nanometer-sized particles; the high surface area of nanosized species allow active material to absorb lithium ions more effectively hence increase capacity with decrease in size; the chemical potentials for lithium ions and electrons may be modified resulting in a change of electrode potential (thermodynamics of the reaction) **(**Kwon *et al*, 2012). As much as there are greater advantages of using the nanomaterials, not much attention is given to the toxicity of the nanomaterials, Table 1 shows the toxicity pathway of the nanomaterial used.

Toxicological Pathway	Example Nanomaterials
Membrane damage/leakage/thinning	Cationic NPs
Protein binding/unfolding responses/loss of function/fibrillation	Metal oxide NPs, polystyrene, dendrimer, carbon nanomaterials
DNA cleavage/mutation	Nano-Ag
Mitochondrial damage: e-transfer/ATP/ PTP opening/apoptosis	UFPs, Cationic NPs
Lysosomal damage: proton pump activity/lysis/ frustrated phagocytosis	UFPs, Cationic NPs, CNTs
Inflammation: signaling cascades/cytokines/ chemokines/adhesion	Metal oxide NPs, CNTs
Fibrogenesis and tissue remodeling injury	CNTs
Blood platelet, vascular endothelial and clotting abnormalities	SiO_2
Oxidative stress injury, radical production, GSH depletion, lipid peroxidation, membrane oxidation, protein oxidation	UFPs, CNTs, Metal oxide NPs, Cationic NPs

Table 1. Experimental examples of major toxicological pathways that could lead to nanomaterial (ENM) toxicity (NPs = Nanoparticles, UFPs = Ultra-Fine Particles) (Xia, T *et al.*, 2010).

2.9 Carbon nanotubes

Carbon nanotubes (CNTs) are well ordered graphitic nanomaterial with lengths ranging from several hundred nanometres. They are classiefied as either single-wall carbon nanotubes (SWCNTs) with internal diameter of 0.7 nm to 2.0 nm (Eder., 2010**;** Iijima *et al.*, 1993) or multi-wall carbon nanotubes (MWCNTs) which typically have inner diameter of 2.0 nm to 30 nm as reported by (Iijima *et al.*, 1991). Conceptually, the nanotubes are viewed as rolled-up structures of one or multiple layers of graphene sheets for SWCNTs and MWCNTs respectively. As for the MWCNTs, the number of centric graphene sheets can range from 2.0 nm to ~100 nm (Dillon, 2010). These are one dimensional carbon allotropes have high electrical conductivity, high surface area, high mechanical strength and excellent thermal and chemical stability. As a result, CNTs are highly attractive for fundamental research and the commercial of application. **Scheme 7** shows the size of (A) single walled carbon nanotube (SWCNTs) and (B) the multi-walled carbon nanotubes (MWCNTs).

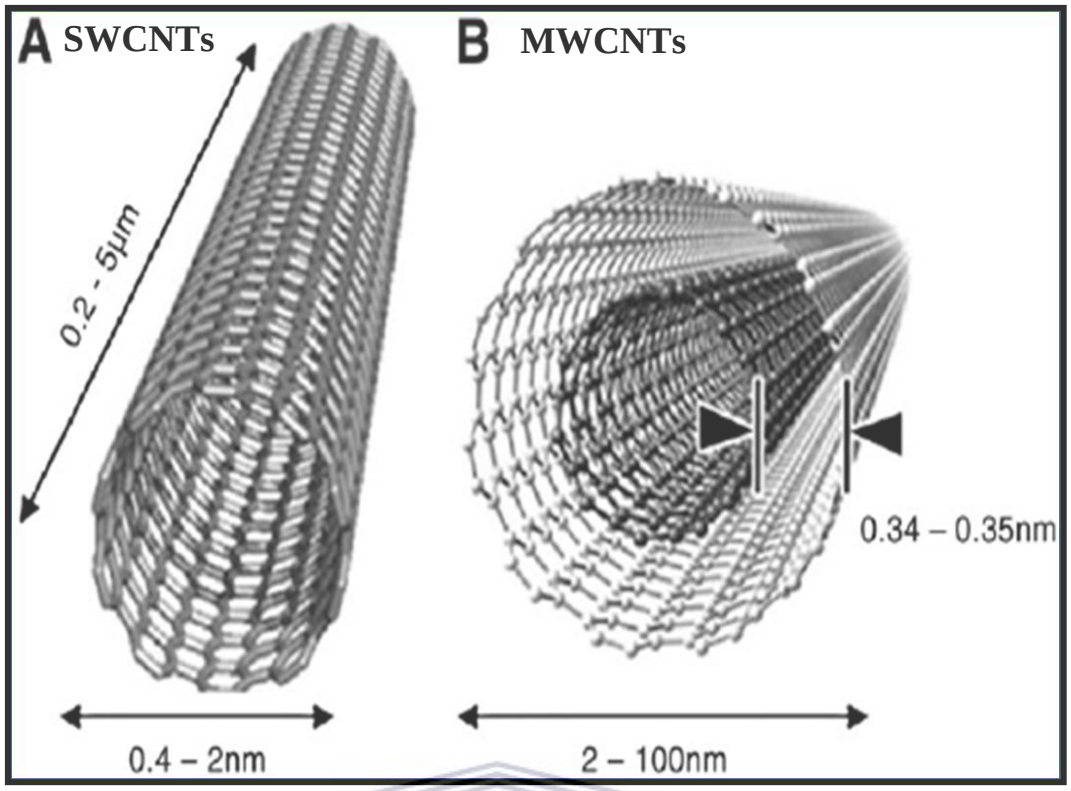

Scheme 8: Shows the images and the size of (**A**) single walled carbon nanotube (SWCNTs) and (**B**) the multi-walled carbon nanotubes (MWCNTs).

CHAPTER 3

RESULTS AND DISCUSSION

Part I

Morphological analysis and characterization of a novel $LiFe_{0.5}Mn_{0.5}PO_4$ and multi-walled carbon nanotubes.

Chapter overview: *This chapter describes the general experimental synthesis of $LiFe_{0.5}Mn_{0.5}PO_4$ which was synthesized using simple facile microwave synthesis, and was sintered at high temperatures (500˚C), via microwave synthesis method, using a stoichiometric amount of 1:1 Fe:Mn nanocomposite as well as the instruments and characterizations techniques used. The multi-walled carbon nanotubes (MWCNTs) were commercially purchased at Sigma. They were used without any preparation.*

Abstract

Lithium-ion (Li-ion) batteries have been widely used in various kinds of electronic devices in our daily life. In this work, the lithium iron manganese phosphate ($LiFeMnPO_4$) cathode was prepared by simple facile microwave method. A recent technological innovation has been the development of lithium ion capacitor (LIC). The LIC combines the advantages of the high-power density of electric double-layer capacitators (EDLC) and high energy density of lithium ion batteries (LIB), by using one EDLC electrode and one LIB electrode in constructing the LIC device. $LiFeMnPO_4$ has received much attention as cathode material in lithium-ion batteries due to its inexpensive and ecofriendly nature. In order to achieve high energy and power densities, a high-voltage LIC has been developed in this study, with activated carbon (AC) as the negative electrode. Physical properties of synthesized electrode materials were investigated using (TEM), (XRD), (EDX), (SAXS), Raman spectroscopy, SS-NMR and (FTIR). The XRD, SEM, and SAXS results show that the composition of $LiFePO_4$ and $LiMnPO_4$ to form a $LiFeMnPO_4$ composite was achieved with olivine structure and the average size of 100 nm. The ss-NMR was used to confirm the structure of $LiFeMnPO_4$.

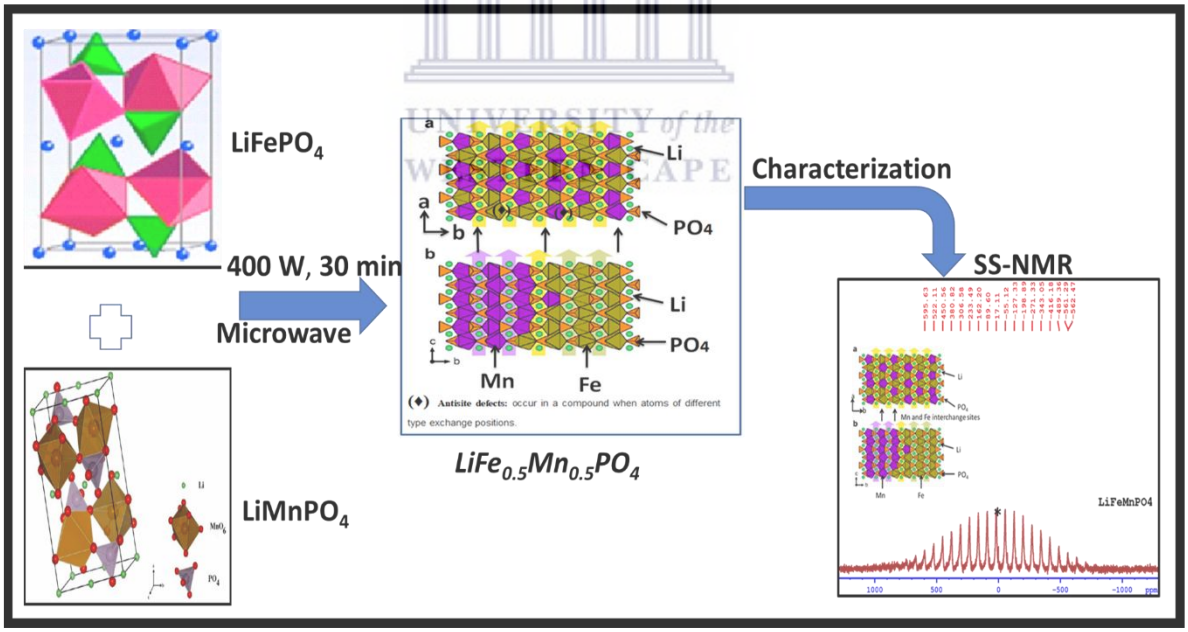

Scheme 9: Synthesis of $LiFeMnPO_4$ composite via microwave synthesis.

3. Introduction

Lithium-ion batteries (LIB) are considered as the most promising energy storage technology. Nowadays, consumer demand is motivating tremendous efforts for high capacity, high power density, fast recharging rate, and great cycling performance. However, these demands bring many challenges to material stability, especially when they are used in electric vehicles (EV). Compared with other cathode materials, olivine-type $LiFePO_4$ draws extensive attention because of its high theoretical capacity, environmental acceptability, and low cost, especially superior thermal stability and safety. The major drawback for $LiFePO_4$ is the intrinsically poor conductivity, which is currently being overcome by coating them with conductive carbon. Carbon coating is a critical component in $C/LiFePO_4$, and $C/LiMnPO_4$ composites. A deep and comprehensive understanding of carbon coating and its effects as well as the synthesis process to control carbon coating on $LiFePO_4$ will contribute to the LIB industry and accelerate the commercialization of EV. Over the last decades of intensive research, phospho-olivine type Lithium manganese iron phosphate ($LiMPO_4$) electrode materials, pioneered by (Padhi and Goodenough *et al.,* 1997), have been identified as serious contenders for high power electrode series. Apart from $LiMPO_4$, other most notable electrode materials are layered $LiMnO_2$ by (Bruce *et al., 2008*) and $LiMSO_4OH$ by (Tarascon *et al.,* 2001) to name a few. Among the phospho-olivines, $LiFePO_4$ (triphylite) and $LiMnPO_4$ (lithiophilite) are well known to form a series of solid-solutions, adopting an orthorhombic crystal structure with Pbnm (62) space group symmetry. Most distinctively, LiFePO4 with a redox potential of 3.4 V versus Li/Li+ is extremely interesting due to its reversible topotactic Li-ion extraction, cyclability, exceptional stability, and flat-voltage characteristics. The main reason for such stability stems from the structural features of $LiFePO_4$, being built by stitching of sheets of FeO_6 octahedra and PO_4 tetrahedra. In such a structure, the strong covalency of the P_{tet}−O bonds in the PO_4^{3-} tetrahedral polyanion uniquely stabilizes the Fe(3d) −O(2p) antibonds (via an inductive effect).

3.1 Experimental Procedure

3.1.1 Reagents and Materials

Analytical reagent grade Lithium sulphate (99.9%), Lithium hydroxide monohydrate (99.995%) trace metal basis, Manganese (II) Sulfate monohydrate, Diethylene gycol (99.0%), magnesium acetate tetrahrate (≥99%), Phosphoric acid (85%) trace metal basis, N-methyl-2-pyrrolidone, anhydrous (99.5%). phosphoric acid (H_3PO_4) and (NH_4) H_2PO_4. Alumina micro polishing pads were obtained from Buehler and urea (99.5%) was obtained from Fluka. (H_3PO_4) and (NH_4) H_2PO_4, (1.5 M) $LiOH.H_2O$ and H_3PO_4 + (NH_4) H_2PO_4 (0.5 M) $MnSO_4.H_2O$ aqueous solution (0.5 M), $FeSO_4.7H_2O$, (0.5M) and acetic acid (1M).

3.1.2. Synthesis of Lithium iron manganese phosphate ($LiFe_{0.5}Mn_{0.5}PO_4$).

The $LiFe_{0.5}Mn_{0.5}PO_4$ powder was synthesized with the complexing agent using a simple and facile microwave-assisted process (Zhang *et al.*, 2017), with minor modifications. To make the $LiFe_{0.5}Mn_{0.5}PO_4$ with low concentration of antisite defects, the pH of the precursors was controlled by using P-source consisting of phosphoric acid (H_3PO_4) and (NH_4) H_2PO_4. Aqueous solution of (1.5M) of $LiOH.H_2O$ and H_3PO_4 + (NH_4) H_2PO_4 aqueous solution (0.5M) were mixed by strong magnetic stirring at room temperature for 5 min. Then $MnSO_4.H_2O$ aqueous solution (0.5M), $FeSO_4.7H_2O$ aqueous solution (0.5M) and acetic acid aqueous solution (1M) were added into the above mixture. The mixed solution was then deposited in the 100 ml XQ quartz vessel, which was then sealed and placed in the microwave reaction system (Multiwave PRO Microwave Reaction from Anton Paar). The power of 400 W was applied to heat the mixture for 30 min. The final product was washed 3 times with acetone and distilled water by centrifugation removing all the excess H_3PO_4, then the product was dried at 70˚C for overnight in the convention oven. To provide a uniform and crystal structure the mixture was sintered at 600˚C for 6 h under the Ar-H_2 (95/5 vol%) atmosphere.

3.2 Instrumentation

The surface morphology, particle size and size distribution of nanomaterial were examined through SEM, TEM and SAXS obtained from JOEL JSM-7500F Scanning Electron Microscope (US), Tecnai G2 F20X-Twin MAT 200 kV Field Emission Transmission Electron Microscope (FEI Eindhoven, Netherlands) and Small Angle X-rays Scattering was obtained from Anton Paar GmbH (Anton-Paar Str 20 A-8054 Graz). X-ray diffraction (XRD) patterns were recorded on a Rigaku Smart Lab 3 kW diffractometer with Cu Kα radiation (λ = 1.5418 Å), with the corresponding operation voltage and current at 40 kV and 100 mA, respectively. The Raman spectra were obtained with a Raman Micro 200, Perkin Elmer precisely Spectrometer LabRAM HR800 (Spectrum software), using an output laser power of 50%. Raman analysis was conducted on powdered samples without any prior sample preparation. The spectra were recorded over a range of 50 to 3270 cm^{-1} using an operating spectral resolution of 2.0 cm^{-1}. The spectra were averaged with 20 scans, at an exposure time of 4 s, with a laser excitation wavelength of 532 nm. Fourier transform infrared (FTIR) spectroscopy was collected on a Nexus 670 spectrometer by using a KBr wafer technique.

3.3 Electron microscopy studies

3.3.1 High resolution scanning electron microscopy (HRSEM)

The particle size and surface morphology of $LiFe_{0.5}Mn_{0.5}PO_4$ are shown in (**Fig. 3. 1a and b**) in which spherically shaped pristine $LiFe_{0.5}Mn_{0.5}PO_4$ had primary particles size of ~ 50 nm. The secondary particles of $LiFe_{0.5}Mn_{0.5}PO_4$ that formed from agglomeration of the primary particles were random in size and range between 100 - 200 nm indicating that the crystals of the phosphor-olivine $LiFe_{0.5}Mn_{0.5}PO_4$ grow very well and have inter-particles boundaries that have an effect in the chemistry of the material, its reactivity due to its porous nature (Chen *et al.*, 2008).

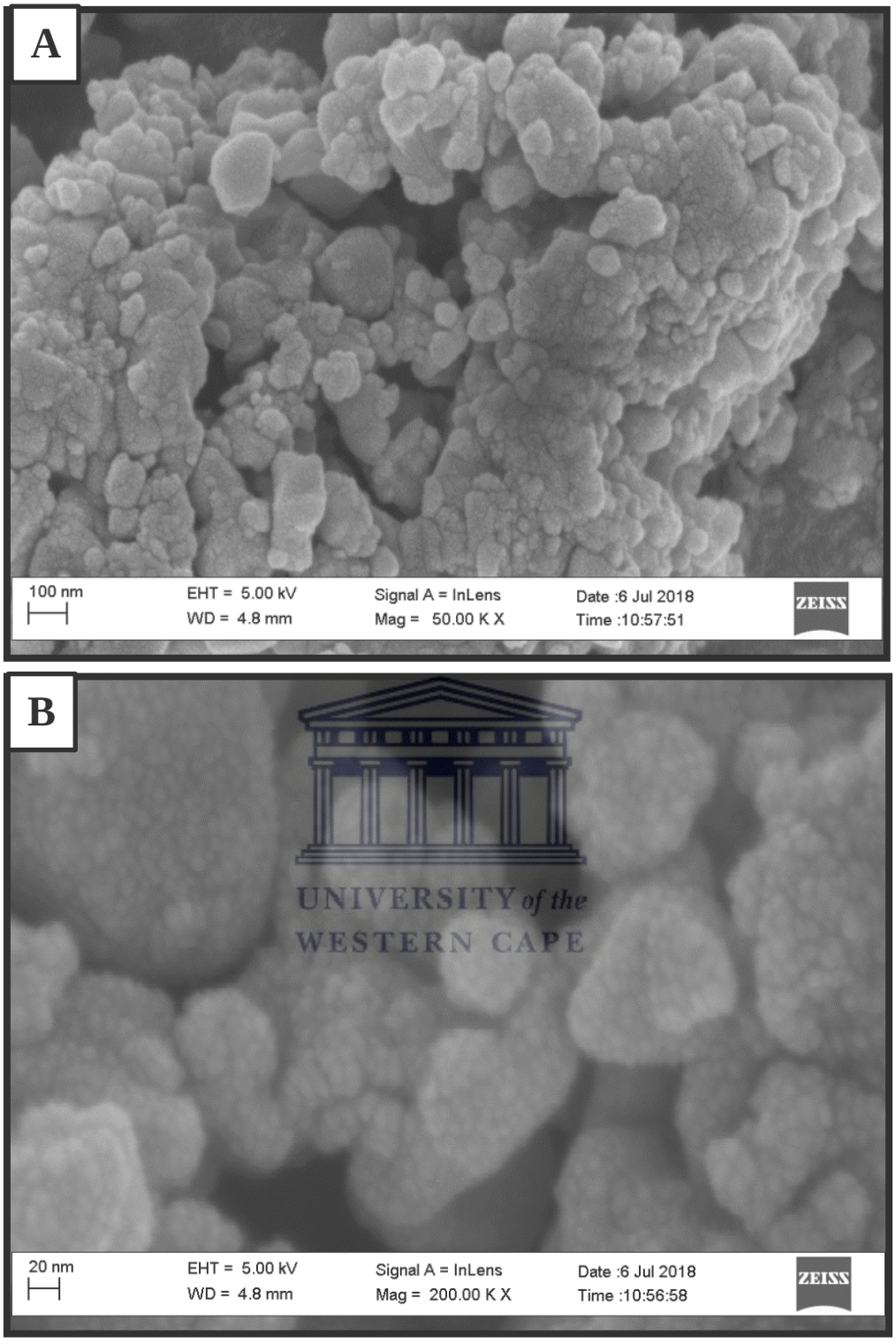

Figure 3.1: HRSEM micrographs of (a) $LiFe_{0.5}Mn_{0.5}PO_4$ nanoparticles and (b) enlarged image, which reveals agglomeration of the $LiFe_{0.5}Mn_{0.5}PO_4$ nanoparticles.

3.3.2 High resolution transmission electron microscopy (HRTEM)

HRTEM micrographs (**Fig 3.2a**) of the synthesized $LiFe_{0.5}Mn_{0.5}PO_4$ nanoparticles shows the structure of ~ 4.0 to 12.0 nm diameters connected in chain of beads due to electronic and magnetic interaction between the particles (Ding, Su and Tian, 2016). Similar HRTEM micrographs images have been reported for $LiFe_{0.5}Mn_{0.5}PO_4$ nanoparticles (Kumar *et al.*, 2017; Novikova *et al*., 2015). The insert of selected area energy dispersive (SAED) on **Fig 3.2b** and HRTEM of $LiFe_{0.5}Mn_{0.5}PO_4$ nanoparticles (**Fig 3.2a and b**), revealed the highly ordered crystalline particles. They also revealed clear lattice fringes indicating formation of pure crystallites of $LiFe_{0.5}Mn_{0.5}PO_4$ nanoparticles. The observed d-spacing at 2.6 nm of neighboring lattice fringes corresponded to the (131) plane of $LiFe_{0.5}Mn_{0.5}PO_4$, which indicated highly ordered crystallites were formed. The histogram on the insert of **Fig 3.2a** of the prepared $LiFe_{0.5}Mn_{0.5}PO_4$ showed the obtained particle size = 6±1.753 nm, which was calculated using image J and was confirmed by Sherrer equation on SAXS. The diffraction patterns were indexed (PDF Card No: **00-013-0336**) according to the Pmnb (62) space group of the selected area (SAD). The pattern corresponding to the presence of the peak in the EDX profile (**Fig 3.3**) could be as a result of the oxidation of the $LiFe_{0.5}Mn_{0.5}PO_4$ nanoparticles during sample preparation and characterization. The peak from carbon and copper were from carbon-coated grid used during the analysis. Analysis of the EDX indicated a stoichiometry of Mn = 0.45640 and Fe = 0.58624. The slight difference in composition inferred from the techniques can be ascribed to the overlap of the Mn-Lβ line with the Fe-Lα line due to the energy resolution (about 140 eV), which can give a systematic overestimation of the Fe signal in EDS (Kumar *et al.*, 2017).

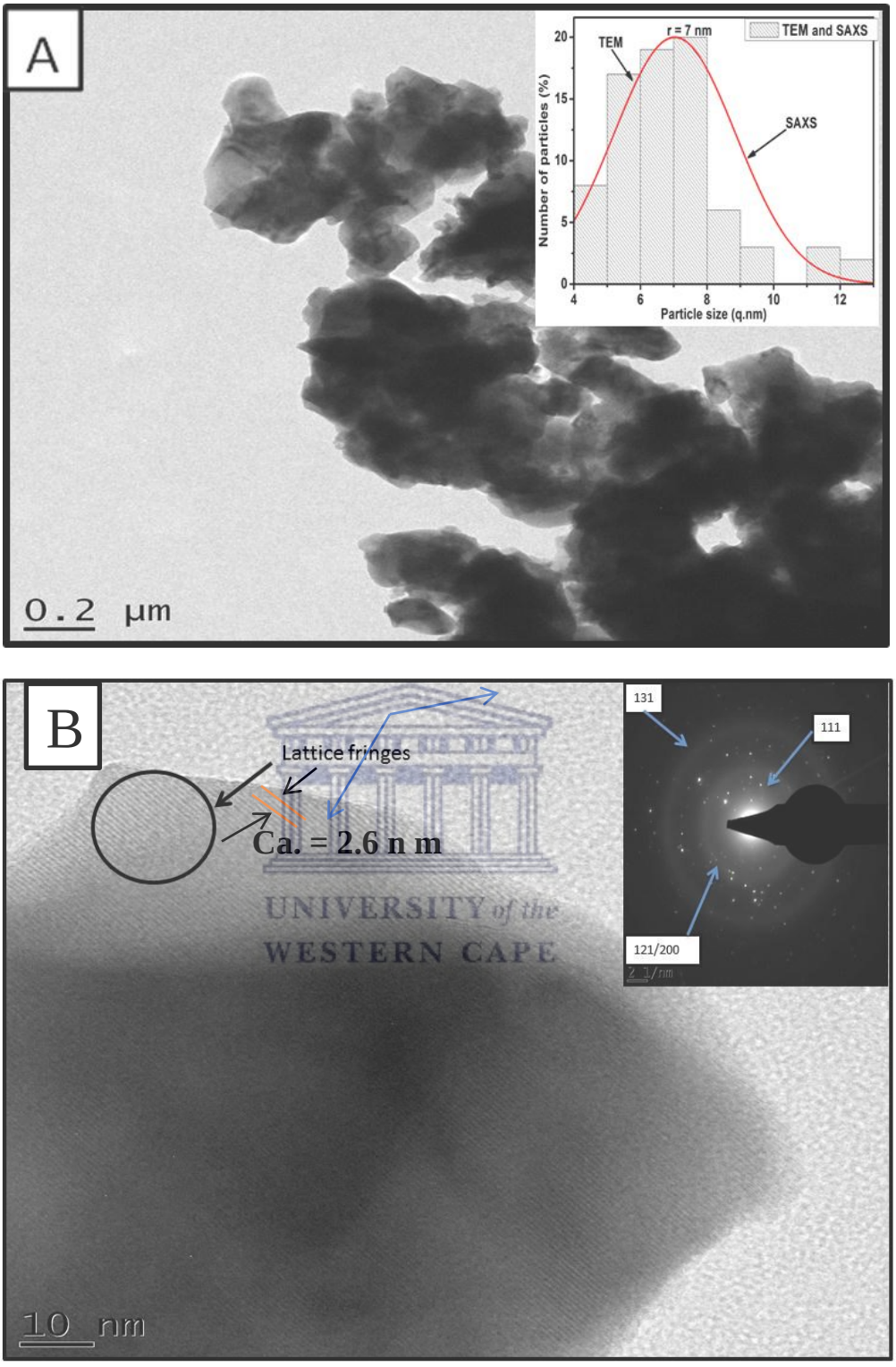

Figure 3.2: HRTEM micrographs of $LiFe_{0.5}Mn_{0.5}PO_4$ nanoparticles and (insert) the histogram showing the size particle on SAXS on (a) and HRTEM micrographs at larger magnification with SAED showing the lattice fringes (b).

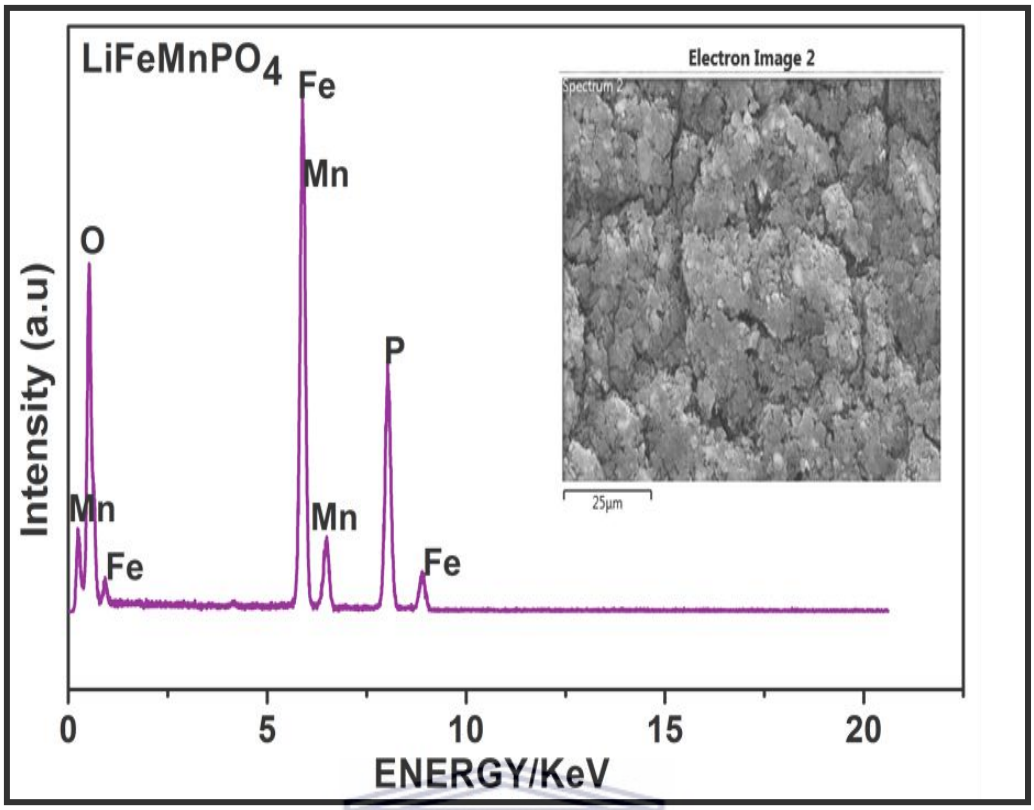

Figure 3.3: EDX profile of $LiFe_{0.5}Mn_{0.5}PO_4$ nanoparticles.

3.4. Analysis of phase composition and crystal structure.

3.4.1 X-ray difraction (XRD) of $LiFe_{0.5}Mn_{0.5}PO_4$

The synthesis of $LiFe_{0.5}Mn_{0.5}PO_4$ nanoparticles with ~7 nm elongated shape long and ~12 nm wide on average, was carried out via micro-wave synthesis is shown on (**Fig 3.4**.). According to Bragg formula and Scherrer equation, the average crystalline size of the sample can be calculated from the full width at half maximum (FWHM). The corresponding parameters of the main peak of the lattice constant as calculated from the XRD spectrum are a = 6.050 Å, b = 10.320 Å and c = 4.710 Å, very close to the structure of lithiophilite (PDF Card No: **01-073-7355**) with Pbnm (62) space group (Paolella *et.al*, 2014**)**. The low intensity of the (020) reflection with respect to the bulk spectrum is due to the small thickness of the nanoparticles along the b-direction (Ding, Su and Tian, 2016). The EDX of the insert on **Fig 3.4**, confirm the corresponding peaks on the XRD, showing the crystalline structure of $LiFe_{0.5}Mn_{0.5}PO_4$. The XRD peaks observed at 18.2°, 25.7°, 28.2°, 28.8°, and 32.7° correspond to 011, 111, 121, 200, and 131 XRD crystal planes of $LiFe_{0.5}Mn_{0.5}PO_4$ which agree with reported reflections (JCPDS 71-0636) (Ding, Su and

Tian, 2016). The intensely sharp XRD peaks of $LiFe_{0.5}Mn_{0.5}PO_4$ signify that the sample is highly crystalline

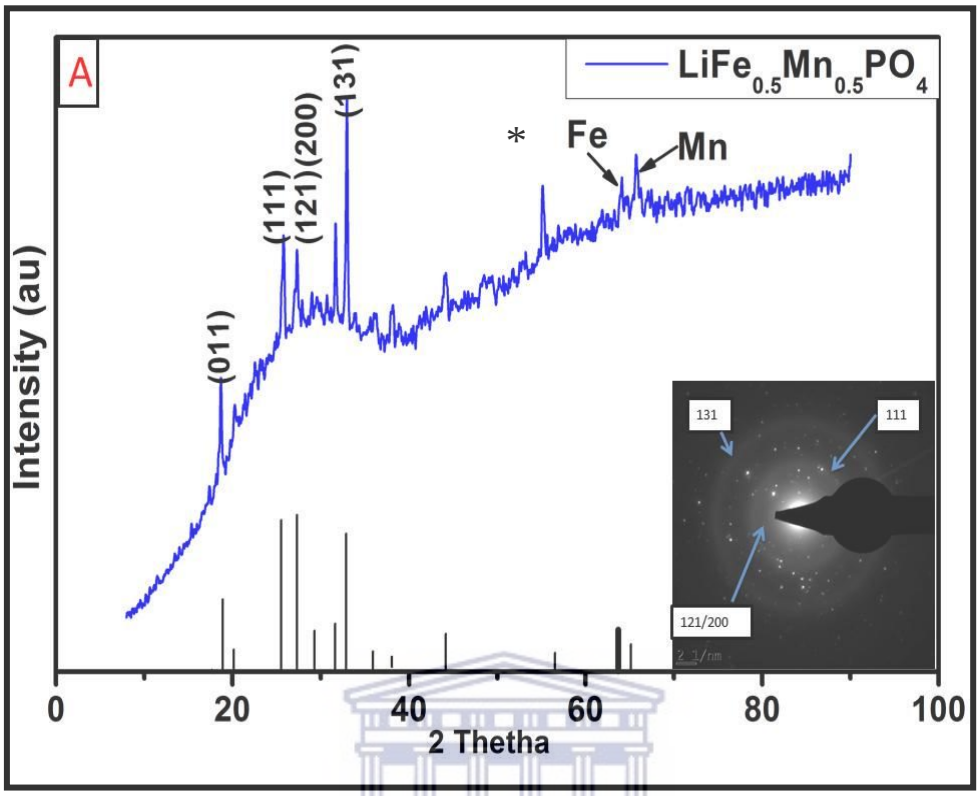

Figure 3.4: XRD pattern of $LiFe_{0.5}Mn_{0.5}PO_4$ nanoparticles (a) and the selected area electron diffraction (SAED) of the $LiFe_{0.5}Mn_{0.5}PO_4$ (b).

3.4.2 Small angle X-ray scattering (SAXS) of $LiFe_{0.5}Mn_{0.5}PO_4$

SAXS is a useful and straight forward technique that is used to determine the size distribution of relatively monodisperse or poly-dispersed nanoparticles. SAXS is used to observe the internal structure of the materials, it uses the same principle used by XRD. SAXS is measured on the small scale from 0˚ to 10˚ while XRD measures from large scale 10˚ to 100˚. **Fig. 3.5** shows the characteristic SAXS curves of $LiFe_{0.5}Mn_{0.5}PO_4$ nanoparticle suspensions: The $LiFe_{0.5}Mn_{0.5}PO_4$ shows a poly-dispersed sample distribution. The $LiFe_{0.5}Mn_{0.5}PO_4$ has semi-crystallinity lattice of the pristine material and it has particle size from 6±1.753 nm which were calculated using image J and was confirmed by Sherrer equation on SAXS. The SAXS reflection appears in similar positions with those observed on XRD but there is slight shit observed. The reflections are a bit weaker and broader. Upon addition of carbon nanotubes, it decreases the size and shape.

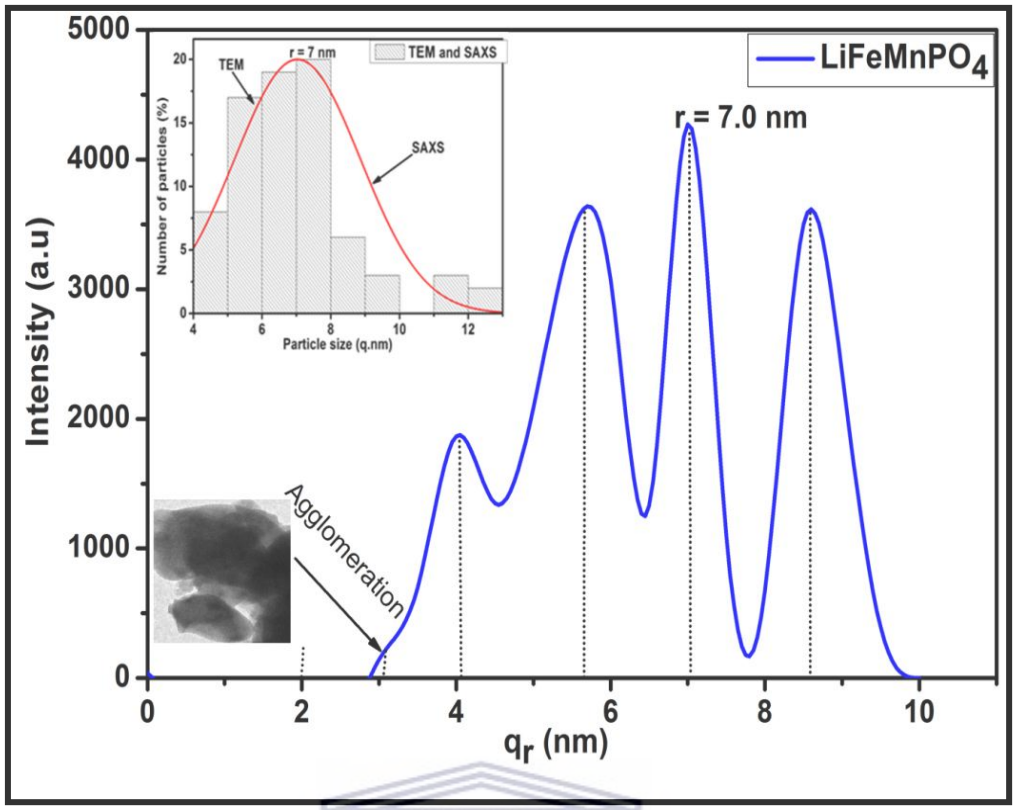

Figure 3.5: SAXS of olivine $LiFe_{0.5}Mn_{0.5}PO_4$ nanoparticles

3.5 Spectroscopy analysis

3.5.1 Fourier transform infrared spectroscopy (FTIR) of $LiFe_{0.5}Mn_{0.5}PO_4$

Fig 3.6 shows the FTIR spectra $LiFe_{0.5}Mn_{0.5}PO_4$ prepared via microwave synthetic route. fourier transform infrared spectroscopy (FTIR) was used to investigate structural information and specific molecule-groups information of the obtained powder in the range 500 - 4000 cm^{-1}. The presence of different types of oxygen functionalities in $LiFe_{0.5}Mn_{0.5}PO_4$ was observed at 3386 cm^{-1} (O-H stretching vibrations), at 1626 cm^{-1} (C=O stretching vibrations), at 1145 cm-1 (C-OH stretching vibrations) (Burba *et al.*, 2006). The IR spectral features of $LiFe_{0.5}Mn_{0.5}PO_4$ have been previously assigned based on group theory analysis, isotope studies, and direct comparison to similar olivine structures ($LiMePO_4$; Me = Fe, Mg, Ni, Mn) (Burba *et al.*, 2006). The spectra are dominated by the intramolecular vibrations of the PO_4^{3-} anion which confirm the presence of phospho-olivine phase in $LiFe_{0.5}Mn_{0.5}PO_4$. These internal vibrations consist of three components;

the antisymmetric PO_4^{3-} stretching mode at 1145 cm^{-1} which is due to OH stretching vibration, the symmetric PO_4^{3-} stretching mode around 965 cm^{-1} and the antisymmetric bending mode between 650 cm^{-1} and 530 cm^{-1} (Norberg *et al*, 2001; Kumar *et al.*, 2011).

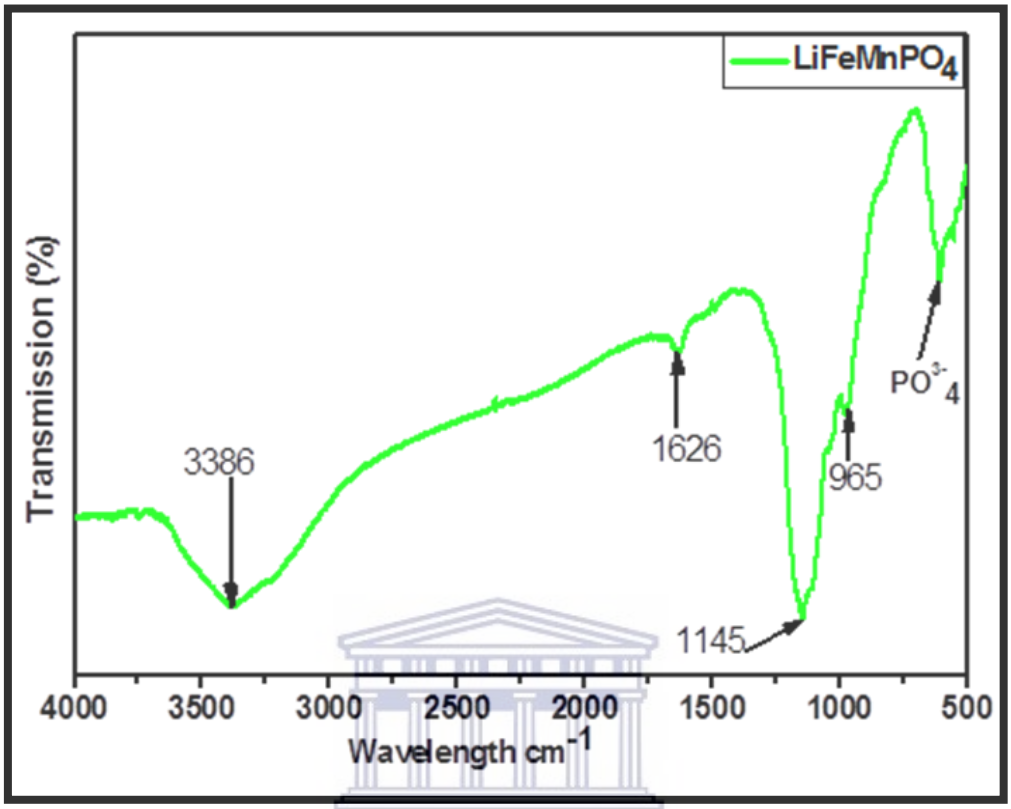

Figure 3.6: FTIR spectra of olivine $LiFe_{0.5}Mn_{0.5}PO_4$ nanoparticles

3.5.2 Raman spectroscopy analysis

Fig 3.7 shows the Raman spectra of the $LiFe_{0.5}Mn_{0.5}PO_4$ nanoparticles measured at wavelength 532 nm. The $LiFe_{0.5}Mn_{0.5}PO_4$ is dominated by a strong and broad band at 493 cm^{-1} corresponding to the symmetric mode of PO_4^{3-}, and the two are intensity bands at 1450 cm^{-1} and 1567 cm^{-1} denoted by a squares that is due to oxidation of the $LiFe_{0.5}Mn_{0.5}PO_4$ (Kumar *et al.*, 2011). The intensity peak at 1654 cm^{-1} is due to the asymmetric stretching modes of the PO_4^{3-} anion (Kumar *et al.*, 2011). The results obtained from XRD, FTIR correspond with Raman spectroscopy which confirmed that olivine $LiFe_{0.5}Mn_{0.5}PO_4$ was obtained.

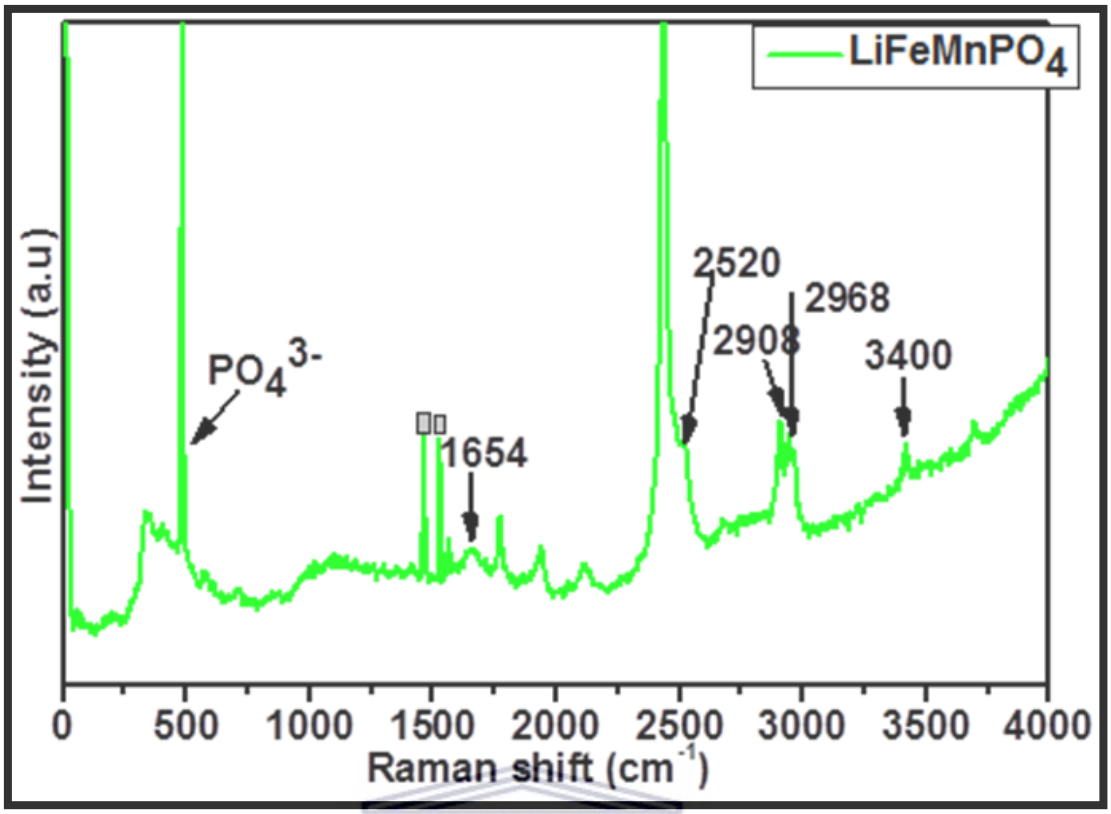

Figure 3.7: Raman spectra of $LiFe_{0.5}Mn_{0.5}PO_4$ nanoparticles

3.6 Solid-state Nuclear Magnetic Rotation of $LiFe_{0.5}Mn_{0.5}PO_4$

The ^{7}Li MAS NMR spectra of $LiFe_{0.5}Mn_{0.5}PO_4$ is shown in **Fig 3.8**. The composition gave rise to a single isotropic ^{7}Li resonance, as expected for the olivine structure. The isotropic ^{7}Li peak arising from the $LiFe_{0.5}Mn_{0.5}PO_4$ sample is considerably broad. The large line width arises from the chemical shift dispersion, suggesting that there is considerable local disorder in the coordination sphere of Li in $LiFe_{0.5}Mn_{0.5}PO_4$, perhaps in the form of site vacancies or Li/Fe and Li/Mn site mixing (Popov *et al.*, 2016). The spin-lattice (T_1) and spin-spin (T_2) relaxation times were measured, and are presented in Table I. The short (T_1) times are typical of nuclei in paramagnetic materials due to the coupling of nuclei to unpaired electrons is an efficient relaxation mechanism. This fast relaxation allows the use of short NMR recycle delays and acquisition of high-quality spectra in a short period of time. The T_2 times measured for these materials are also quite short, more than three times shorter than those observed for ^{7}Li in $LiMn_2O_4$ (Tucker *et al.*, 2002).

Sample	$\Delta_{isotropic}$(ppm)	T_1(ms)	T_2 (µs)	δ (ppm)	η
$LiFe_{0.5}Mn_{0.5}PO_4$	41	2.6	330	1370	0.90

Table 2: The NMR parameters measured for $LiFe_{0.5}Mn_{0.5}PO_4$.

There is no change in the shape of the NMR spectrum was observed, probably because the bulk susceptibility of the sample powders was too high to be effectively matched. The following analysis was therefore performed on the unmatched spectra. We estimated the anisotropic shift and asymmetry parameter that describe the paramagnetic coupling using Herzfeld-Berger analysis (HBA), a widely available program for applying Herzfeld-Berger analysis to MAS spectra. The anisotropic shift, d, and the asymmetry parameter, h, are defined:

$$\delta = \delta 33 - \delta iso \quad \textbf{(6)}$$

$$\eta = \frac{\delta 22 - \delta 11}{\delta} \quad \textbf{(7)}$$

Where δiso is the isotropic chemical shift, and δ11, δ22, and δ33 are the principal components of the paramagnetic interaction tensor. δ represents the linewidth of the paramagnetic broadening, while h indicates the deviation of the interaction symmetry from the extremes of axial symmetry (η = 0) or spherical symmetry (η = 1). This analysis does not account for the effects of susceptibility broadening, which masks the paramagnetic anisotropy. The calculated values are presented in Table 1. A similar extent of paramagnetic broadening ~1360-1380 ppm is observed for both compositions. The calculated asymmetry parameter indicates a nearly spherically symmetric paramagnetic interaction for $LiFe_{0.5}Mn_{0.5}PO_4$. This is consistent with elongation of the unit cell in a and b directions and contraction in the c direction observed upon replacement of Fe with Mn (Tucker *et al.*, 2002).

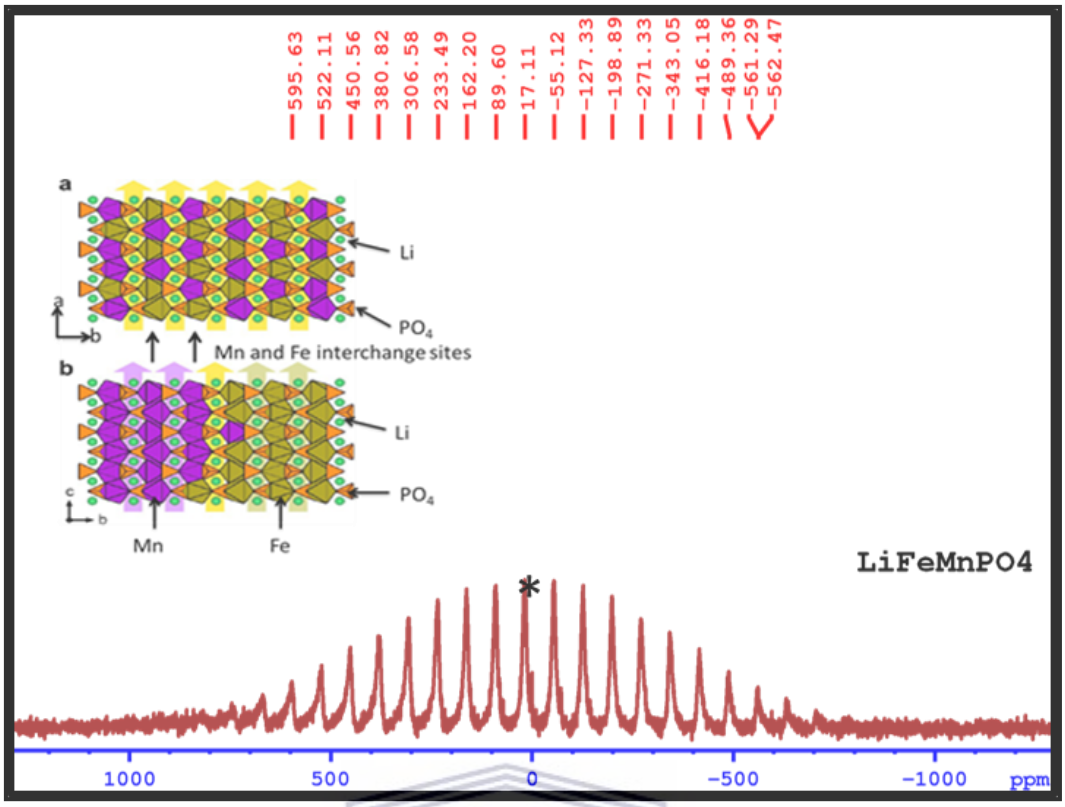

Figure 3.8: The ^{7}Li MAS NMR spectroscopy has been used to study the changes in the local environments of lithium during the preparation of $LiFe_{0.5}Mn_{0.5}PO_4$ cathode material using solid-sate method.

CHAPTER 4

RESULTS AND DISCUSSION

PART II

Analysis of electrochemical and structural enhanced $LiFe_{0.5}Mn_{0.5}PO_4$-MWCNTs cathode system

Chapter overview: This section displays electrochemistry and discussion obtained for the novel MWCNTs coated $LiFe_{0.5}Mn_{0.5}PO_4$. The method used for the synthesis of multi-walled carbon nanotubes (MWCNTs) coated lithium iron manganese phosphate ($LiFe_{0.5}Mn_{0.5}PO_4$), as well as the instrumentations and characterization used, are fully detailed in this section. The results were obtained; for the synthesized cathode material are presented and discussed in this chapter.

Abstract

This paper explores the synergistic and catalytic properties of a newly developed lithium ion battery (LIB) composite cathode of the $LiFe_{0.5}Mn_{0.5}PO_4$ and MWCNTs nanoparticle. Spinel phase the $LiFe_{0.5}Mn_{0.5}PO_4$ was doped with multi-walled carbon nanotubes. This $LiFe_{0.5}Mn_{0.5}PO_4$/MWCNTs composite architecture accommodates the structural transformation that occurs during Li+ ion charge and discharge. X-ray diffraction studies showed doped material retained well-developed octahedral structures bounded by (111) planes.

4. Introduction

The of the intensive research on phosphor-olivine type lithium manganese phosphate (LMP) and lithium iron phosphate (LFP) electrode materials, pioneered by (Padhi *et al.*, 1997), have been labelled as serious contenders for high power electrode series. In comparison with lithium cobalt oxide (LCO) they provide very good-safely characteristics in terms of thermal runaway (Paolella *et al.*, 2013). It also features various advantages such as very good cyclability, cost effective and environmentally friendly due to the absence of cobalt (Paolella *et al.,* 2013). By partial substitution of Fe by Mn atoms, the isostructural is obtained $LiFe_{0.5}Mn_{0.5}PO_4$. In addition to the above-mentioned advantages of $LiFe_{0.5}Mn_{0.5}PO_4$, it provides a higher cell voltage due to the presence of Mn. The influence of Mn in $LiFe_{0.5}Mn_{0.5}PO_4$ is visible in the typical charge and discharge curve of $LiFe_{0.5}Mn_{0.5}PO_4$. In contrast to $LiFePO_4$, two voltage plateaus can be observed which correspond to the redox couples Fe^{2+}/Fe^{3+} at approximately 3.6 V vs. Li/Li^+ and $Mn^{2+/}Mn^{3+}$ at approximately 4.1 V vs. Li/Li+. High reversible capacities of up to 164 mAh_g^1 are reachable over a wide range of Mn content (Starke *et al.,* 2017). Despite all the advantages, $LiFePO_4$ and $LiFe_{0.5}Mn_{0.5}PO_4$ have been reported to be sensitive to moisture and water. Direct contact to water causes a loss of active lithium from the olivine structure under formation of Li_3PO_4 on the particle surface and thus reduces the material's energy density (Wu *et al.,* 2016). Exposure to air and moisture causes similar effects and a disordered crystal structure as it was investigated for $LiFePO_4$ (Wu *et al.,* 2016), and it is expected to be similar for $LiFe_{0.5}Mn_{0.5}PO_4$. In addition, $LiFe_{0.5}Mn_{0.5}PO_4$ is known for the problem of manganese dissolution like other Mn-containing cathode materials (e.g.,

LMNO) as well (Wu *et al.,* 2016). For $LiFe_{0.5}Mn_{0.5}PO_4$, a relation between the presence of traces of water in the battery and manganese dissolution has been found (Ali *et al., 2016).* These facts indicate that $LiFe_{0.5}Mn_{0.5}PO_4$ must be treated with care in the production process of batteries and that an environmentally friendly water-based cathode production tends to result in poor electrochemical characteristics. However, water-based cathodes could significantly improve a battery's eco-balance by avoiding solvents such as N-methyl-2-pyrrolidone (NMP), which are hazardous to the environment and health (Wu *et al.,* 2016). However, if the amount of NMP is controlled, it cannot cause too much harm, and it also gives great improvement of the battery performance.

4.1 Experimental procedure

4.1.1 Characterization techniques of MWCNTs coated $LiFe_{0.5}Mn_{0.5}PO_4$ nanoparticles

The surface morphology, particle size and size distribution of nanomaterial were examined through SEM, TEM images and SAXS obtained from JOEL JSM-7500F Scanning Electron Microscope (US), Tecnai G2 F20X-Twin MAT 200 kV Field Emission Transmission Electron Microscope (FEI Eindhoven, Netherlands) and Small Angle X-rays Scattering was obtained from Anton Paar GmbH (Anton-Paar Str 20 A-8054 Graz). X-ray diffraction (XRD) patterns were recorded on a Rigaku Smart Lab 3 kW diffractometer with Cu Kα radiation (λ = 1.5418 Å), with the corresponding operation voltage and current at 40 kV and 100 mA, respectively. The Raman spectra were obtained with a Raman Micro 200, Perkin Elmer precisely Spectrometer LabRAM HR800 (Spectrum software), using an output laser power of 50%. Raman analysis was conducted on powdered samples without any prior sample preparation. The spectra were recorded over a range of 50 to 3270 cm^{-1} using an operating spectral resolution of 2.0 cm^{-1}. The spectra were averaged with 20 scans, at an exposure time of 4 s, with a laser excitation wavelength of 532 nm. Fourier transform infrared (FTIR) spectroscopy was collected on a Nexus 670 spectrometer by using a KBr wafer technique.

4.1.2 Synthesis of $LiFe_{0.5}Mn_{0.5}PO_4$-MWCNTs nanoparticles composite

The $LiFe_{0.5}Mn_{0.5}PO_4$ powder was synthesized using a facile microwave-assisted process previously reported (Zhang *et al.,* 2017) with minor modifications. To make the $LiFe_{0.5}Mn_{0.5}PO_4$ with low concentration of antisite defects, the pH of the precursors was controlled by using P source consisting of phosphoric acid (H_3PO_4) and (NH_4) H_2PO_4. Aqueous solution of (1.5M) of $LiOH.H_2O$ and H_3PO_4 + (NH_4) H_2PO_4 aqueous solution (0.5 M) were mixed by a strong magnetic stirring at room temperature for 5 min. Then $MnSO_4.H_2O$ aqueous solution (0.5 M), $FeSO_4.7H_2O$ aqueous solution (0.5 M) and acetic acid aqueous solution (1M) were added into the above mixture. Then 2 grams of commercially purchased multi-walled carbon nanotubes was added. The mixed solution was then sonicated for 10 min, to mix well since multi-walled carbon nanotubes are insoluble to aqueous solution. The mixture was deposited in the 100 ml XQ quartz vessel, which was then sealed and placed in the microwave reaction system (Multi-wave PRO Microwave Reaction from Anton Paar). The power of 400 W was applied to heat the mixture for 30 min. The final product was washed 3 times with acetone and distilled water by centrifugation removing all the excess H_3PO_4, then the product was dried at 70˚C for overnight in the convention oven. To provide a uniform and crystal structure the mixture was sintered at 600˚C for 6 h under the Ar-H_2 (95/5 vol%) atmosphere.

Results and Discussion

4.2. Electron microscopic studies

4.2.1 High resolution scanning electron microscopy (HRSEM)

High resolution scanning electron microscopy (HRSEM) is a versatile imaging technique capable of producing three-dimensional images of material surfaces**.** HRSEM was used to determine the morphology, the particle size distribution and the elemental composition of $LiFe_{0.5}Mn_{0.5}PO_4$-MWCNTs. The crystallized size of the as prepared particles was calculated by use of the Scherrer's equation:

$$d = \frac{0.9\lambda}{B\cos\theta} \quad \textbf{(8)}$$

Where λ represents the wavelength, d is the mean crystallite in volume; B is the width at the maximum hump of the broadened diffraction peak. The morphology of the $LiFe_{0.5}Mn_{0.5}PO_4$-MWCNTs composite cathode showed by **Fig 4.1** revealed nanoclusters of long stranded carbon nanotubes which facilitate movement of electrons during extraction and insertion of lithium within 3D framework between nanotubes and adjacent $LiFe_{0.5}Mn_{0.5}PO_4$ particles. The porous nanostructure of the $LiFe_{0.5}Mn_{0.5}PO_4$ is lamented by the carbon nanotubes, providing wider electrode surface area that helps to minimize energy loss due to both activation and concentration of polarizations at the electrode surface and increase the electrode efficiency or utilization. The synthesized $LiFe_{0.5}Mn_{0.5}PO_4$ particles were subsequently attached to the ends and walls on the nanotubes. The strands have uniform diameter of 0.5-5 nm which agree with the one observed in TEM.

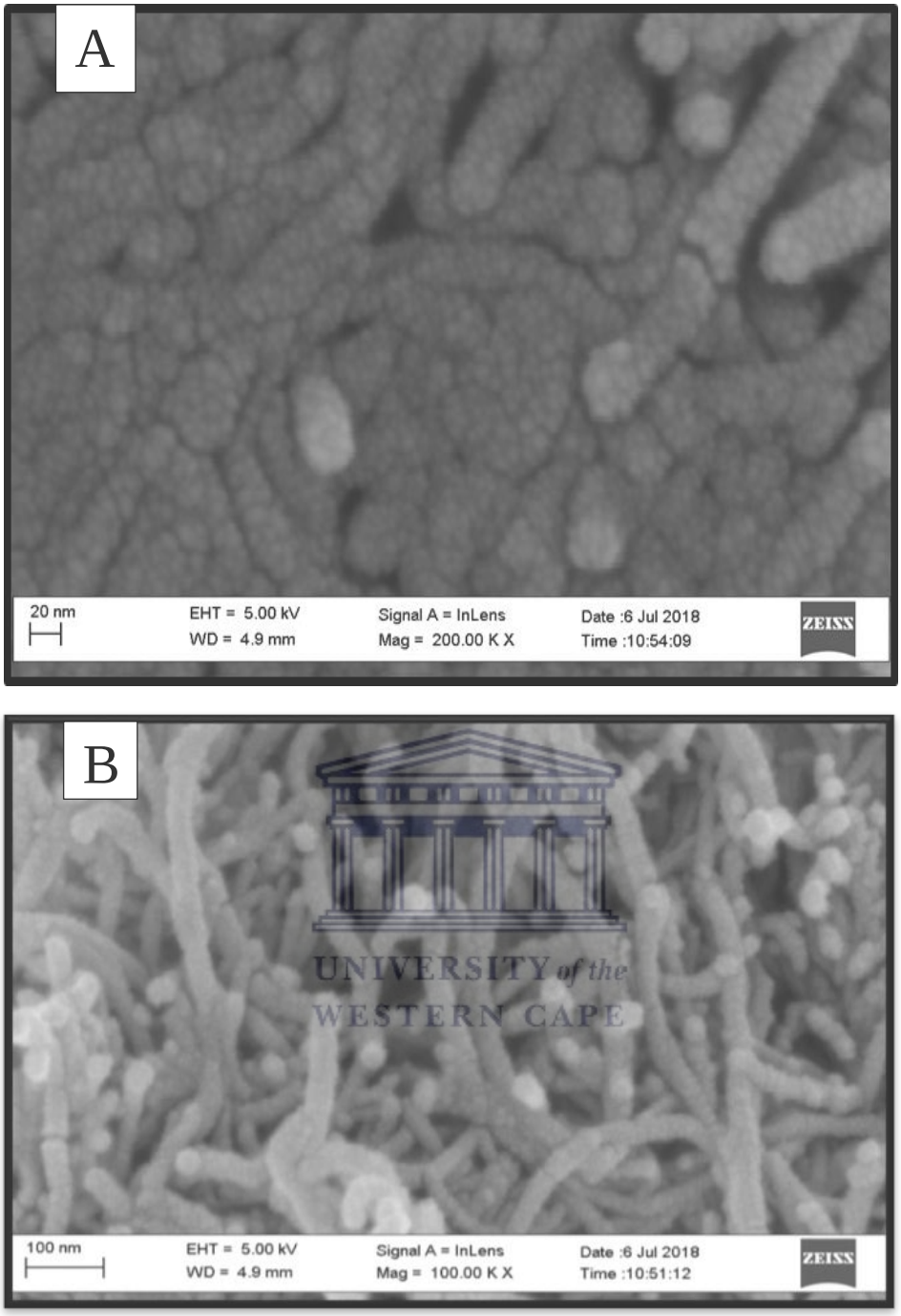

Figure 4.1: High resolution scanning electron microscopy (HRSEM) of $LiFe_{0.5}Mn_{0.5}PO_4$-MWCNTs.

4.2.2 High resolution transmission electron microscopy (HRTEM)

Synthesis method	Crystallite size (nm)	Particle size (nm)	References
Solid state	90±5*	200-300*	Curtis *et al.*, 2004
Sol-gel	80±5*	10-200*	Churikov *et al*, 2009
Xerogel	50±5*	10-150*	Tay *et al.*, 2010
AIM	30±5*	10-50*	Wu *et al.*, 2017
Micro-wave	>20±5	>5-20	

Table 3: Crystallite sizes and particle sizes as obtained from the (111) peak via the Scherrer equation and using TEM analysis, respectively. Reported by other researchers (*), SAXS was not reported.

Table 3 shows synthetic routes that were performed and gave the smallest size of nanoparticles, (Tay *et al.*, 2010), however they also showed the largest difference in the lattice parameters. The different crystallite sizes and particle sizes obtained via the Scherrer equation and measured by TEM, respectively, are summarized in **Table 3.**

Note that in XRD and SAXS the crystallite size is being measured and that with TEM it is the particle size. However, by closer analysis of the TEM image, it is also possible to obtain the crystallite size. Calculations of the crystallite size dimensions were performed using the Scherrer formula (**Eq. 8**), which links the full width at half maximum (FWHM), of a peak with the size of the plane responsible of that diffraction peak (Wu *et al.*, 2017*)*.

$$T = \frac{Ks.\ \lambda}{\sqrt{L-l.}} \quad (9)$$

Where, (T) is the size of the diffractive domain in the hkl direction (Å), Ks is the shape factor[3], (λ) is the X-ray wavelength (1.548_A for Cu K); L (rad) is the FWHM of a peak due to the diffraction domain; l (rad) is the contribution of the apparatus to the FWHM and

(θ) is the diffraction angle. The Scherrer equation analysis of the FWHM of the most intense peaks was collected. It is stressed that the calculation has been done only on the (111) peak for $LiFe_{0.5}Mn_{0.5}PO_4$-MWCNTs composite cathode. The $LiFe_{0.5}Mn_{0.5}PO_4$-MWCNTs micrographs of TEM are shown in the **Fig 4.2**, indicating that the $LiFe_{0.5}Mn_{0.5}PO_4$-MWCNTs are relatively poly-dispersed (same shape but different sizes) with uniform diameter of 0.5-5 nm. On the insert on **Fig 4.2a** are high resolution transmission electron (HRTEM) micrographs with an in-plane (0-110) lattice spacing of Ca. 0.14 nm, revealing the high crystallinity of the bulk $LiFe_{0.5}Mn_{0.5}PO_4$-MWCNTs. On **Fig 4.2b** shows the prepared composite of SAXS, which were calculated, showing the (particle sizes = 3.7±0.957 nm) of the $LiFe_{0.5}Mn_{0.5}PO_4$-MWCNTs. Upon addition of the MWCNTs on the $LiFe_{0.5}Mn_{0.5}PO_4$ the particle size is reduced, when compared with $LiFe_{0.5}Mn_{0.5}PO_4$ (particle size = 6±1.752 nm) and the particle size correspond with the SAXS size distribution as shown on **Fig 4.2b**. HR-TEM and SAXS are agreement to each other in terms of the size of nanoparticles.

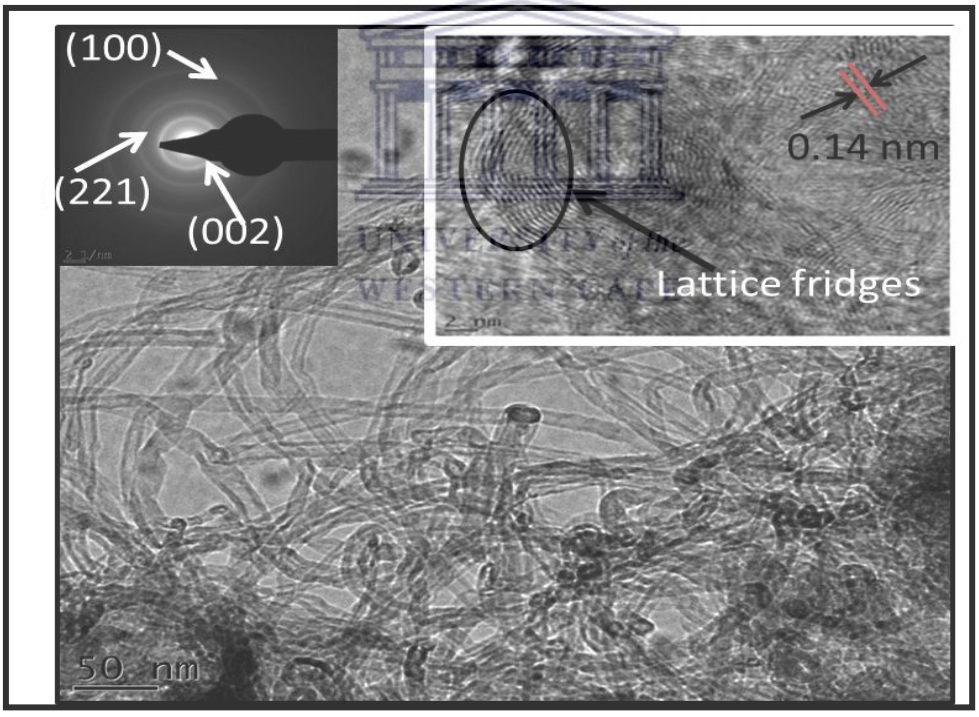

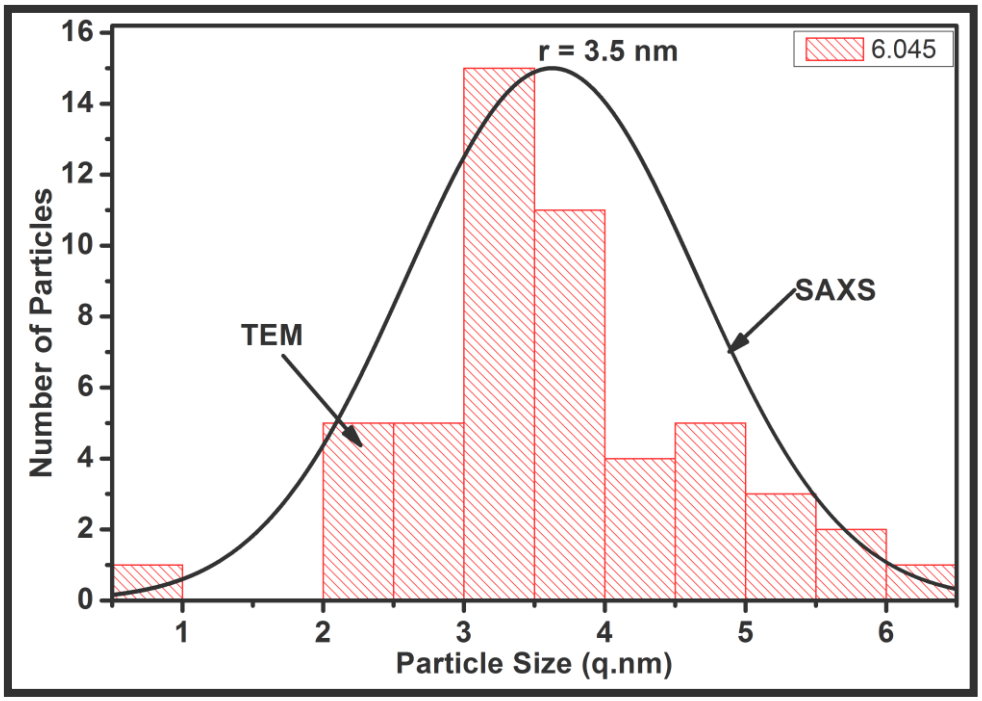

Figure 4.2: Shows the (a) $LiFe_{0.5}Mn_{0.5}PO_4$-MWCNTs micrographs of TEM and (b) SAXS showing the obtained particle size.

4.3 Analysis of phase composition and crystal structure

4.3.1 X-ray difraction (XRD) of $LiFe_{0.5}Mn_{0.5}PO_4$

The Crystalline structure of $LiFe_{0.5}Mn_{0.5}PO_4$-MWCNTs, on **Fig 4.3** shown 3 different diffraction patterns, this is evident by the appearance of the 002, 211 and 100, at 30˚, 40˚ and 50˚, respectively. The hexagonal crystalline carbon was indexed to (JCPDS No. 41-1487), (Elder, 2010. Lin *et.al*, 2004) which complement the preferential growth of MWCNTs. SAXS reflections appears in similar positions with those observed on XRD. The reflections are a bit weaker and broader this evidences that stack-like structure similar to present in the $LiFe_{0.5}Mn_{0.5}PO_4$-MWCNTs nanocomposites. The intensity peaks of the pure carbon nanotubes are more intense but upon adding the $LiFe_{0.5}Mn_{0.5}PO_4$, the peaks shift from 50° and 34° to 44° and 26° respectively. These peaks are in correspondence with the one obtained from SAXS. This indicates that the multi-walled carbon nanotubes fully covered the composite material. The singe peaks for $LiMn_xFe_{1-x}PO_4$ ($0 < x < 1$) illustrate completed solid-reaction between $LiMnPO_4$ and $LiFePO_4$ precursors even under the

condition of carbon-coating. Moreover, the shift in the XRD patterns is related with the molar ratio of Mn and Fe in the as-prepared $LiFe_{0.5}Mn_{0.5}PO_4$-MWCNTs composites

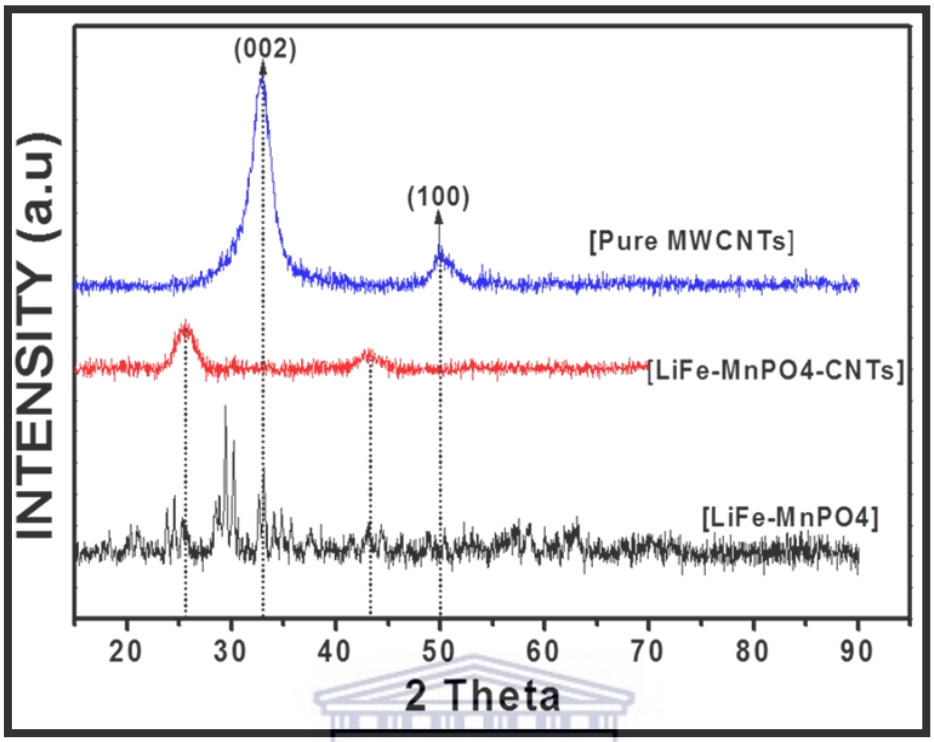

Figure 4.3: XRD patterns of pure multi-walled carbon nanotubes (a), $LiFe_{0.5}Mn_{0.5}PO_4$-MWCNTs (b), and $LiFe_{0.5}Mn_{0.5}PO_4$ (c).

4.3.2 Small angle x-ray scattering analysis

The homogenous, spatial distribution of the multi-walled carbon nanotubes across the $LiFe_{0.5}Mn_{0.5}PO_4$ sample on the microscopic scale is one key factor which determines the structural property relationship of the nanocomposite. On **Fig 4.4** the $LiFe_{0.5}Mn_{0.5}PO_4$-MWCNTs shows a poly-dispersed sample distribution, the MWCNTs on the $LiFe_{0.5}Mn_{0.5}PO_4$ increases the crystallinity lattice of the composite material and it also reduced the particle size from 6±1.753 nm of $LiFe_{0.5}Mn_{0.5}PO_4$ to 3.7±0.957 nm of $LiFe_{0.5}Mn_{0.5}PO_4$-MWCNTs, which were calculated using image J and was confirmed by Sherrer equation on SAXS. The Crystalline structure of $LiFe_{0.5}Mn_{0.5}PO_4$-MWCNTs, showed 3 different diffraction patterns, this is evident by the appearance of the 002, 211 and 100, at 30˚, 40˚ and 50˚, respectively. The hexagonal crystalline carbon was indexed to (JCPDS No. 41-1487), (Elder, 2010; Lin *et.al*, 2004) which complement the preferential growth of MWCNTs. SAXS reflections appears in similar positions with those observed

on XRD. The reflections are a bit weaker and broader this evidences that stack-like structure like that are also present in the $LiFe_{0.5}Mn_{0.5}PO_4$-MWCNTs nanocomposites.

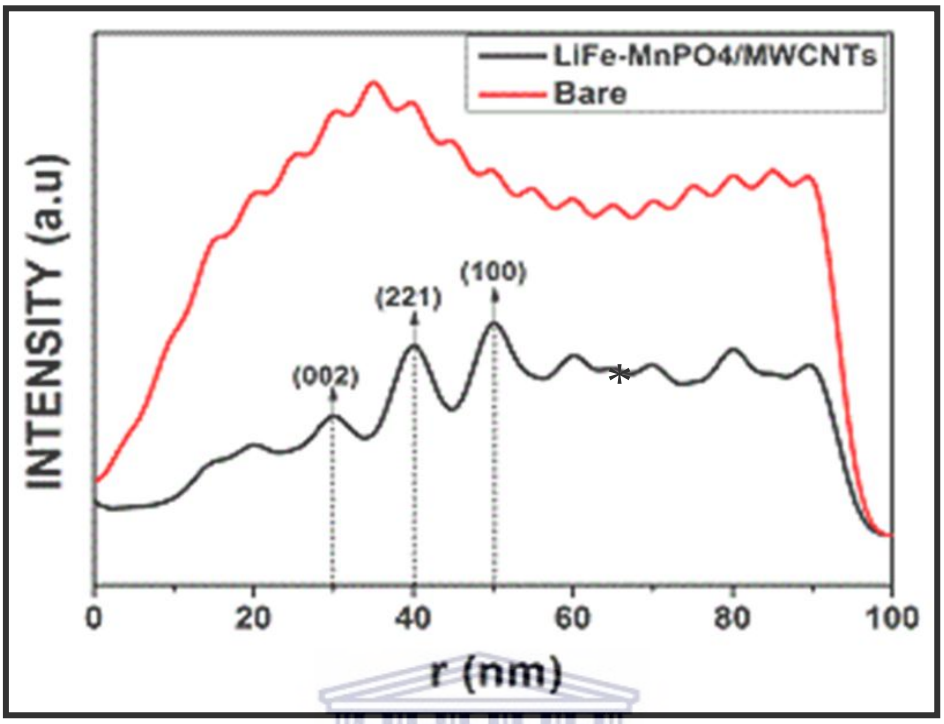

Figure 4.4: SAXS pattern of the $LiFe_{0.5}Mn_{0.5}PO_4$-MWCNTs showing sample distribution and the crystallinity of the composite.

4.4 Spectroscopy Analysis

4.4.1 Fourier-transform infrared spectroscopy (FTIR) of $LiFe_{0.5}Mn_{0.5}PO_4$-MWCNTs

Fig 4.5 shows the FTIR spectra of prepared $LiFe_{0.5}Mn_{0.5}PO_4$, pure MWCNTs and the modified $LiFe_{0.5}Mn_{0.5}PO_4$-MWCNTs. Fourier transform infrared spectroscopy (FTIR) was used to investigate structural information and specific molecule-groups information of the obtained powder in the range 500 - 4000 cm^{-1}. The presence of different types of oxygen functionalities in $LiFe_{0.5}Mn_{0.5}PO_4$ was observed at 3386 cm^{-1} (O-H stretching vibrations), at 1626 cm^{-1} (C=O stretching vibrations), at 1145 cm-1 (C-OH stretching vibrations) (Ali *et al.*, 2016*)*. It is observed that $LiFe_{0.5}Mn_{0.5}PO_4$-MWCNTs and MWCNTs a few similarities in their structures, the oxygen functionalities in $LiFe_{0.5}Mn_{0.5}PO_4$-MWCNTs and pure MWCNTs were observed at 3386 cm^{-1} (O-H stretching vibrations), at 1400 cm^{-} and 1626 cm^{-1} (C=O stretching vibrations), at 1145 cm-1 (C-OH stretching vibrations). There is a strong (C=H stretching), due to the presence of carbon nanotubes (Panchal *et al.*,

2018). The IR spectral features of $LiFe_{0.5}Mn_{0.5}PO_4$ have been previously assigned based on group theory analysis, isotope studies, and direct comparison to similar olivine structures ($LiMePO_4$; Me = Fe, Mg, Ni, Mn) (Burba *et al.*, 2006). The $LiFe_{0.5}Mn_{0.5}PO_4$-MWCNTs spectra were dominated by the intramolecular vibrations of the PO_4^{3-} anion and G and D band which confirm the presence of carbon phase in $LiFe_{0.5}Mn_{0.5}PO_4$. These internal vibrations consist of three components; the antisymmetric PO_4^{3-} stretching mode at 1145 cm^{-1} which is due to OH stretching vibration , the symmetric PO_4^{3-} stretching mode around 965 cm^{-1} and the antisymmetric bending mode between 650 cm^{-1} and 530 cm^{-1} (Norberg *et al.*, 2001; Kumar *et al.*, 2011; Panchal *et al.*, 2018). The FTIR results, and Raman confirmed the presence of carbon nanotubes, was still maintained and this implies that the material is stable as was also observed in the XRD result.

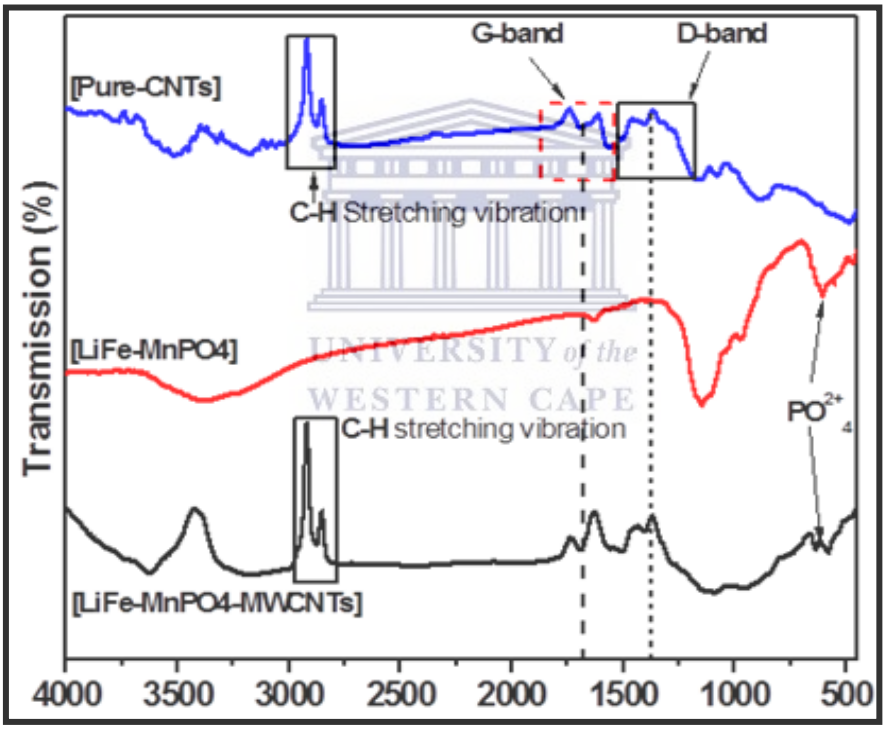

Figure 4.5: IR spectra of $LiFe_{0.5}Mn_{0.5}PO_4$-MWCNTs (a), $LiFe_{0.5}Mn_{0.5}PO_4$ (b), and MWCNTs (c).

4.4.2 Raman spectroscopy of $LiFe_{0.5}Mn_{0.5}PO_4$-MWCNTs

Raman spectroscopy is a nondestructive technique, and high-resolution tool for the characterization of the lattice structure and the electronic, optical, and phonon properties of carbon materials, including three-dimensional (3-D) (Schulz, 2018). **Fig 4.6** shows the Raman spectra of the $LiFe_{0.5}Mn_{0.5}PO_4$-MWCNTs nanoparticles and pure MWCNTs measured at wavelength 532 nm. From **Fig 4.6** the Raman spectra of the $LiFe_{0.5}Mn_{0.5}PO_4$-MWCNTs is dominated by strong and sharp peaks at 1465 cm^{-1} and 1530 cm^{-1} due to the presence of carbon. The strong and sharp peak reveals the crystallinity of the $LiFe_{0.5}Mn_{0.5}PO_4$-MWCNTs and the two are intensity representing D-band at 1450 cm^{-1} and G-band at 1567 cm^{-1} for MWCNTs. The peak intensity at 1657 cm^{-1} is due to the asymmetric stretching modes of the PO_4^{3-} anion (Kumar *et al*, 2011). The results from XRD, FTIR and Raman spectroscopy confirmed that olivine $LiFe_{0.5}Mn_{0.5}PO_4$-MWCNTs was obtained.

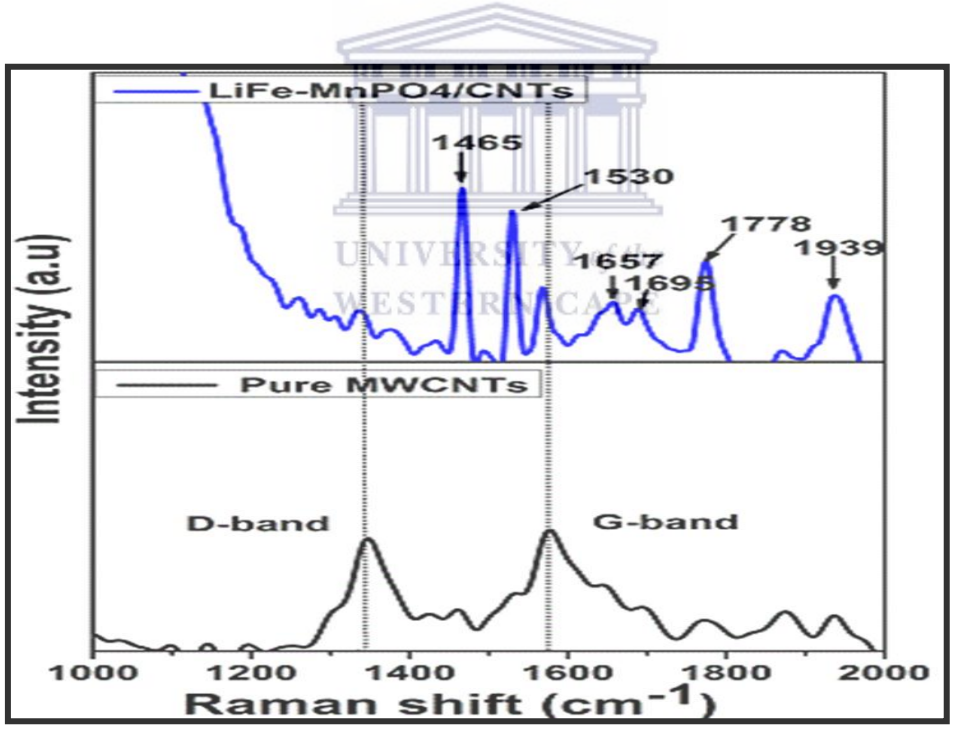

Figure 4.6: Shows the Raman spectra of the $LiFe_{0.5}Mn_{0.5}PO_4$-MWCNTs nanoparticles and pure MWCNTs measured at wavelength 532 nm.

4.5 Solid-state NMR of $LiFe_{0.5}Mn_{0.5}PO_4$-MWCNTs

Solid-state NMR was used to locate the local environment of ^{13}C in high surface area product. A ^{13}C MAS NMR spectrum of $LiFe_{0.5}Mn_{0.5}PO_4$-MWCNTs after thermal treatment at 600 ˚C is shown in **Fig 4.7.** The ^{13}C MAS NMR spectrum of $LiFe_{0.5}Mn_{0.5}PO_4$-MWCNTs is compared with the pure MWCNTs to observe any shifts that occurred. Spectra's isotropic line position specify one carbon sites as expected in composite structure and a degree of disorder in the local electronic structure due to ratio of Mn^{3+}/Mn^{2+} and Fe^{3+}/Fe^{2+} around carbon atoms. The sharp peak is due to the MWCNTs, and there is a slight shift of the peak from 110 ppm to 107 ppm from that of the MWCNTs which was reported (Kleist *et al.,* 2006). The sharp and narrow peak was observed on the $LiFe_{0.5}Mn_{0.5}PO_4$-MWCNTs due to the high temperatures, also indicating the crystallinity of the cathode composite. This clearly indicates that the stoichiometric ratio of carbon used to coat the $LiFe_{0.5}Mn_{0.5}PO_4$ is higher (2:1). Therefore, the $LiFe_{0.5}Mn_{0.5}PO_4$ has a slight effect on the carbon. The XRD, SAXS and TEM also confirmed these findings.

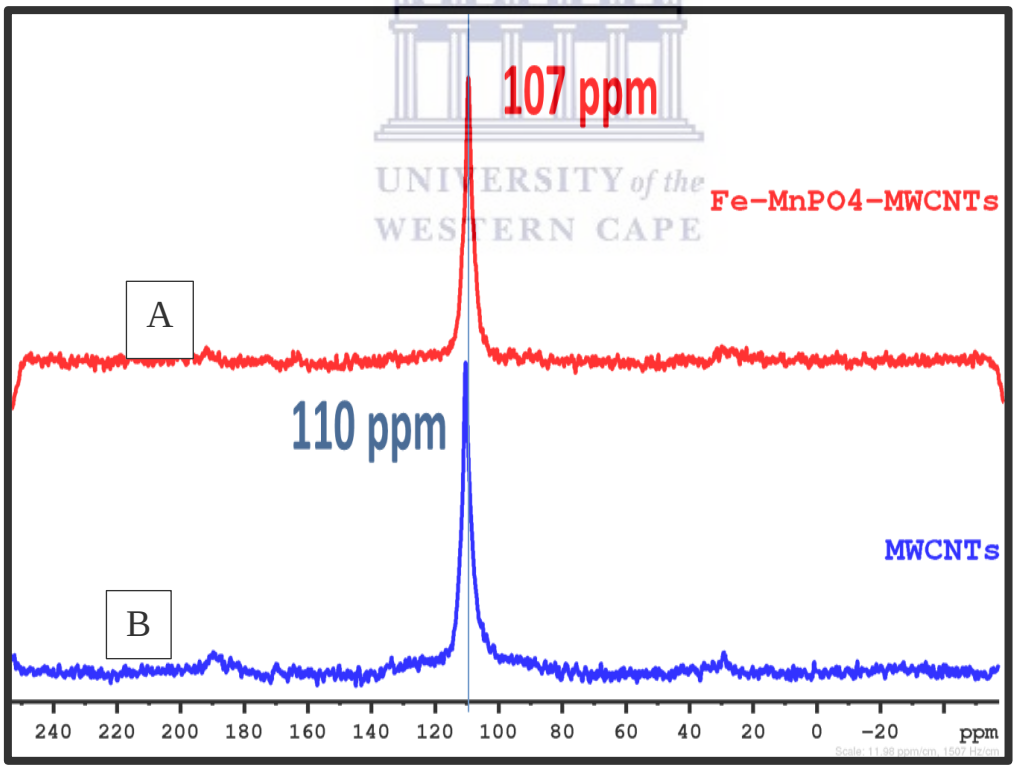

Figure 4.7: The ^{13}C MAS-NMR spectroscopy has been used to study the changes in the local environments of ^{13}C during the preparation of $LiFe_{0.5}Mn_{0.5}PO_4$-MWCNTs cathode material using solid-sate method. ^{13}C MAS-NMR spectrum of $LiFe_{0.5}Mn_{0.5}PO_4$-MWCNTs (a), and MWCNTs (b).

CHAPTER 5
RESULTS AND DISCUSSION

Electrochemical studies of $LiFeMnPO_4$ and $LiFeMnPO_4$-MWCNTs

Chapter review: *This section displays electrochemistry and discussion obtained for the novel $LiFe_{0.5}Mn_{0.5}PO_4$, and MWCNTs coated $LiFe_{0.5}Mn_{0.5}PO_4$, the cyclic voltammetry and electrochemical impedance is explained also the charge and discharge of both cathode material.*

Abstract

In this work, the phase evolution and Lithium transport of doped Lithium iron manganese phosphate ($LiFe_{0.5}Mn_{0.5}PO_4$) and pristine $LiFe_{0.5}Mn_{0.5}PO_4$ system was examined using cyclic voltammetry and galvanostatic-potentiostatic curve analysis. The phosphor-olivine $LiFe_{0.5}Mn_{0.5}PO_4$, was synthesized via microwave synthesis using $LiFePO_4$ and $LiMnPO_4$ as precursors, which were prepared via microwave synthesis. The ratio by mass of the precursors was 1:1 Mn: Fe. Cyclic voltammetry was used to evaluate the electrochemical parameters (electron transfer and ionic diffusivity) of the $LiFe_{0.5}Mn_{0.5}PO_4$ redox couple in 1 M $LiPF_6$ in organic electrolyte solution. The bulky $LiFe_{0.5}Mn_{0.5}PO_4$ contains mixed cations, which both has octahedral structures M1 (Fe) and M2 (Mn) sites and has the charge/discharge capacity for $LiFe_{0.5}Mn_{0.5}PO_4$-MWCNTs composite were 259.9 mAh/g and 177.6 mAh/g, respectively, at 0.01 V/s. The corresponding values for pristine $LiFe_{0.5}Mn_{0.5}PO_4$ were 115 mAh/g and 44.75 mAh/g, respectively. The structures dictate the degree of the intersites order or disorder which plays a key role in determining electrochemical redox potentials. The redox potentials show two separate distinct redox centers that correspond to Fe^{2+}/Fe^{3+} (3.5 V vs Li/Li^+) and Mn^{2+}/Mn^{3+} (4.1 V vs Li/Li^+) due to interaction arrangement of Mn-O-Fe in the olivine lattice, which are commonly observed in the electrochemistry measurements. Nyquist plots of the electrochemical impedance spectroscopy (EIS) results showed $LiFe_{0.5}Mn_{0.5}PO_4$, /MWCNTs having increased conductivity with lower resistance of charge. Scheme 10 shows the semicircle diameter of $LiFe_{0.5}Mn_{0.5}PO_4$/MWCNTs composite electrode is much smaller than that of pristine $LiFe_{0.5}Mn_{0.5}PO_4$, which indicates that the ternary composite has the lowest

electrochemical charge-transfer resistance. This result demonstrates that $LiFe_{0.5}Mn_{0.5}PO_4$/MWCNTs can allow faster electron transport in the composite and faster charge transfer in the parallel $LiFe_{0.5}Mn_{0.5}PO_4$/MWCNTs solution interface. for $LiFe_{0.5}Mn_{0.5}PO_4$-MWCNTs showed improved capacity retention, having better cyclability, especially at high C rate. It was found that the improvement of cycling performance is greatly ascribed to the enhanced physical structure and good electrical conductivity of MWCNTs incorporated $LiFe_{0.5}Mn_{0.5}PO_4$.

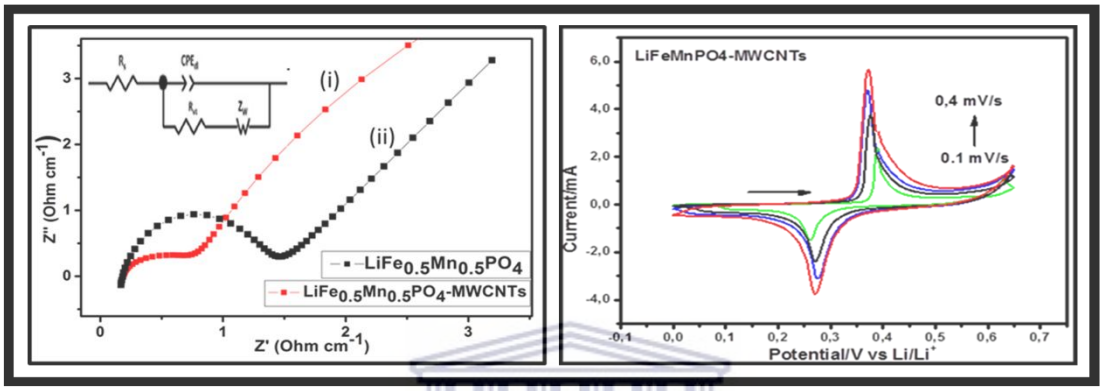

***Scheme 10**. EIS Nyquist plot of $LiFe_{0.5}Mn_{0.5}PO_4$* **(ii)** *and $LiFe_{0.5}Mn_{0.5}PO_4$-MWCNTs* **(i)** *and cyclic voltammetry of $LiFe_{0.5}Mn_{0.5}PO_4$-MWCNTs composite.*

5. Introduction

Carbon nanotubes form conductive composites with inorganic nanocrystals (Hemery *et al.*, 2014). Compared to single-wall carbon nanotubes (SWNT) the multi-walled carbon nanotubes (MWNT) are cheaper, mechanically more robust and their electrical conductivity is less affected by chemical functionalization. Composite materials of MWNT with titanium dioxide have been investigated for application in photocatalysis (Hemery *et al.*, 2014) including photocatalytic hydrogen generation (Xu *et al.*, 2014) and dye-sensitized solar cells (Xu., 2014; Hemery., 2014). In these applications, the beneficial role of MWNT is assumed to consist in improved separation of photogenerated charges, but very low MWNT concentrations (<1 wt%) are required to avoid charge recombination with the electrolyte in dye-sensitized solar cells (He *et al.*, 2015). Improved separation of photogenerated electrons/holes was also demonstrated in solar cells based on band-gap excitation of TiO2 dispersed on SWNT (Javani *et al.*, 2014). The electrochemical lithium storage in carbon $LiFe_{0.5}Mn_{0.5}PO_4$-MWCNTs composites has been studied, too (Wang *et al.*, 2014), reflecting the fact that $LiFe_{0.5}Mn_{0.5}PO_4$ belong to the top interesting host structures for lithium insertion. These studies confirmed in unison that the electrochemical activity of the composite $LiFe_{0.5}Mn_{0.5}PO_4$/MWCNTs is improved compared to that of the pristine $LiFe_{0.5}Mn_{0.5}PO_4$ (Person *et al.*, 2002). Some authors reported on significantly enhanced Li-storage capacity of the $LiFe_{0.5}Mn_{0.5}PO_4$/MWNTs nanocomposite (Persan *et al.*, 2002), but others (churikov *et al.*, 2009) did not support this observation. From the viewpoint of electrochemical lithium storage, the phosphate olivine's (Doeff, 2013), viz. LiMPO4 (M= Fe, Mn) have been extensively studied in the past. They are promising cathode materials for Li-ion batteries due to high safety, low cost and environmental tolerability. However, their poor electrical conductivity is a crucial issue to be addressed (Doeff, 2013) either by doping (Fergus., 2010) or by surface coating with elemental carbon (Chan, 2005). The conductivity problem is considerably more significant for $LiMnPO_4$ (conductivity of $\sim 10^{-14}$ Scm^{-1} compared to $\sim 10^{-9}$ Scm^{-1} for $LiFePO_4$), but optimization of the synthesis, that is the formation of carbon coating via microwave synthesis, provided reasonably active materials, too (Wang *et al.*, 2014). The effect of MWNT on improvement of the performance of $LiFePO_4$ has been reported by several studies in the past (He *et al.*, 2015).

5.1 Instrumentation

5.1.1 Characterization and analysis

The electrochemistry experiment measurements were recorded with Zahnner IM6 electrochemical workstation from MeBtechnik at a bias potential of 0.222 V, amplitude of 5 mV and frequency range of 100 mHz to 100 kHz. The experiments were conducted at room temperature using a conventional three-electrode compartment cell. Glassy carbon (3 mm diameter, BAS, MF-2012) was used as the working electrode; Ag/AgCl couple and platinum wire as the reference electrode and auxiliary electrode respectively. The cell was enclosed in a rounded Faraday cage and kept under flowing oxygen and nitrogen gases. Potassium hydroxide (KOH) was used as the electrolyte for the reaction medium. A potential range of -2.0 to 2.0 V and 0.1 – 0.8 mV/s scan rates were used for CV while for EIS measurements were recorded at formal potential of 0.071 V and perturbation amplitude of 5 mV within the frequency range of 100 mHz -100 KHz. Ethylene carbonate/dimethyl carbonate/ethyl methyl carbonate (EC: DMC 1:1:1 by volume) solution containing 1 $mol \cdot L^{-1}$ $LiPF_6$ was used as the electrolyte. Charge discharge data were recorded from MTI 8 Channels Battery Analyser between 3.0 – 4.0 V at 0.1 C rates.

5.2 Results and Discussion

5.2.1 Electrochemical studies

The prepared of $LiFe_{0.5}Mn_{0.5}PO_4$-MWCNTs composite were investigated by cyclic voltammetry (CV) and electrochemistry impendence (EIS) to identify or confirm the cathode composition with a better performance.

5.2.2 Cyclic voltammograms (CV)

The CV profiles of $LiFe_{0.5}Mn_{0.5}PO_4$-MWCNTs and $LiFe_{0.5}Mn_{0.5}PO_4$ are shown on **Fig 7:**

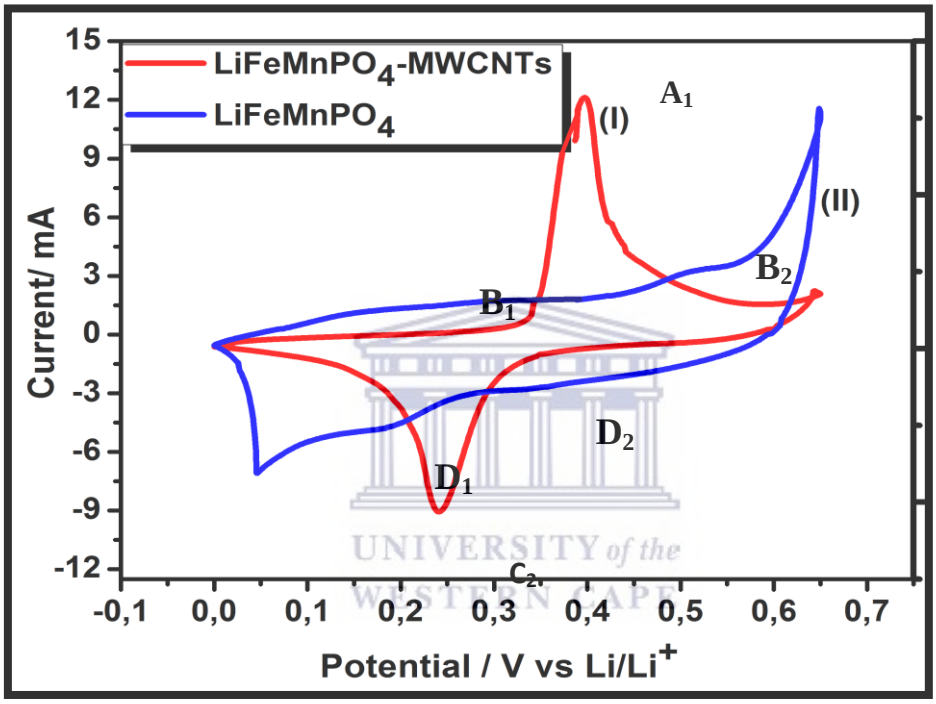

Figure 5.1: Cyclic voltammograms of (i) $LiFe_{0.5}Mn_{0.5}PO_4$-MWCNTs and (ii) $LiFe_{0.5}Mn_{0.5}PO_4$ in 1 M $LiPF_6$ containing 1:1 v/v ethylene carbonate solvent mixture. Scan rate 0.1 mV/s (Voltage range: -0.1 – 0.8 V)

Fig 5.1: Shows the cycle voltammograms of $LiMn_{0.}5Fe_{0.5}PO_4$-MWCNTs (i) and $LiFe_{0.5}Mn_{0.5}PO_4$ (ii). The cyclic voltammograms (i) are characterized by well-defined pair redox peaks which are associated with the electrochemical lithium ion deinsertion/insertion within the octerhedral sites of $LiFe_{0.5}Mn_{0.5}PO_4$ structure upon the two phase oxidation/reduction of $Fe^{2+/3+}$ and $Mn^{2+/3+}$ redox couple, indicating a good crystallinity of the cathode material (Hu *et al.*, 2013-Li *et al.*, 2008-Lu *et al.*, 2001). In $LiFe_{0.5}Mn_{0.5}PO_4$-MWCNTs the sharp peaks were observed and indicate a more facile lithium ion transfer resulting in better kinetic reaction when compared with $LiFe_{0.5}Mn_{0.5}PO_4$ (ii). Again, the

peak separation in $LiFe_{0.5}Mn_{0.5}PO_4$-MWCNTs (E_{pa} - E_{pc}), ΔEp = 0.21 V) is less than that of $LiFe_{0.5}Mn_{0.5}PO_4$ (ii) Mn^{2+}/ Mn^{3+} consists of reduction peak C_1 at -0.47 V which correspond with anodic peak A_1 at 0.74 V, at a formal potential, E° = 0.14 V. The peak to peak separation (E_{pa} - E_{pc}), ΔEp = 1.21 V. Whereas for Fe^{2+}/ Fe^{3+} the reduction peak C_1 = 0.019 V which correspond with anodic peak A_1 at 0.09 V, at a formal potential, E° = -0.071 V. The peak to peak separation (E_{pa} - E_{pc}), ΔEp = 0.071 V. These sets of peaks were due to the redox reaction of Mn^{2+}/Mn^{3+} and Fe^{2+}/ Fe^{3+} couple. The two ambipolar electron reactions were due to result of mixed metal centers in the MO_6 octahedrons $Fe^{2+/3+}$ and $Mn^{2+/3+}$. (Liu *et al.,* 2019; Nayak *et al.,* 2018) The $LiFe_{0.5}Mn_{0.5}PO_4$ shapes of voltammograms show diminished and broadened peaks revealed more sluggish lithium deinsertion/insertion behavior (Bo Ding *et al.,* 2013). The slight shifts in the Mn^{3+}/Mn^{2+} and Fe^{3+}/Fe^{2+} oxidation peaks in $LiMn_{0.5}Fe_{0.5}PO4$ relative to $LiMnPO_4$ and $LiFePO_4$ were the results of mixed metal centers in the MO_6 octahedrons. The similar ionic radii of Fe^{2+} and Mn^{2+} and similar structures of $LiMnPO_4$ and $LiFePO_4$ enabled the Fe-substituted $LiMn_{0.5}Fe_{0.5}PO_4$ to be formed as a solid solution of $LiMnPO_4$ and $LiFePO_4$. This solid solution will, however, have an average metal−oxygen bond length longer than that of $LiFePO_4$ but shorter than that of $LiMnPO_4$. The decrease in the average metal−oxygen bond length to $LiMn_{0.5}Fe_{0.5}PO_4$ as well as the higher electronegativity of Fe will reduce the ionic character of the Mn−O bond, causing a negative shift in the $Mn^{3+/2+}$ equilibrium electrode potential. As a result, the Fe^{3+}/Fe^{2+} redox couple would shift to a slightly higher potential and the Mn^{3+}/Mn^{2+} redox couple, to a slightly lower potential. In comparison with reported work (Xu, 2004-Xia, 2008-Yang *et al.,* 2013-Zhu *et al.,* 2008; Doeff, 2013; Bo Jang *et al.,* 2016). The $LiFe_{0.5}Mn_{0.5}PO_4$-MWCNTs suggest a better electrochemical reversibility in the former than in the latter. The electrochemical deinsertion/insertion of lithium ions into $LiFe_{0.5}Mn_{0.5}PO_4$ can be described as:

Oxidation: $2\,LiFe^{2+}_{0.5}Mn^{2+}_{0.5}PO_4 - Li^+ - e^+ \rightarrow 2\,Li_{0.5}\,Fe^{3+}_{0.5}Mn^{2+}_{0.5}PO_4$ **(10)**

Reduction: $2\,Li_{0.5}\,Fe^{3+}_{0.5}Mn^{2+}_{0.5}PO_4 - Li^+ - e^+ \rightarrow 2\,Fe^{3+}_{0.5}Mn^{2+}_{0.5}PO_4$ **(11)**

Cyclic voltammetry was also used to calculate the charge and discharge for $LiFe_{0.5}Mn_{0.5}PO_4$ and $LiFe_{0.5}Mn_{0.5}PO_4$-MWCNTs composite so to compare it with the one

obtained from galvanostatic-potentiostatic curve. The charge/discharge capacities obtained from the integrated area under the anodic peak at the scan rate of 10 mV/s indicate that the composite $LiFe_{0.5}Mn_{0.5}PO_4$-MWCNTs cathode exhibited a charge capacity of 259 mAh/g and a discharge capacity of 177 mAh/g for the insertion of lithium and reduction of Mn^{3+} to Mn^{2+}, Fe^{2+} to Fe^{2+} and the corresponding values for $LiFe_{0.5}Mn_{0.5}PO_4$ were for charge capacity 115 mAh/g and discharge capacity 44 mAh/g respectively. The calculated capacities show that $LiFe_{0.5}Mn_{0.5}PO_4$-MWCNTs composite has higher capacity compared with $LiFe_{0.5}Mn_{0.5}PO_4$. For the purpose of this research work, the cathodic capacity is our main interest and it was found out to be 177 mAh/g this was close to the reported theoretical capacity of 170 mAh/g for $LiMnPO_4$ (Wu *et al.,* 2012). Therefore $LiMn_{0.5}Fe_{0.5}PO_4$-MWCNTs composite exhibits better electrochemical performance and it can be proposed to be used in lithium ion batteries as cathode material. The capacities were calculated according to the following steps:

The integration of the Area peak obtained at 10 mV/s scan rate from $LiMn_{0.5}Fe_{0.5}PO_4$-MWCNTs nanocomposite gave the area under the current-potential curve as 9.7 $x10^{-4}$ Ampere-Volt (AV).

The charge, $$Q = \frac{\text{Area (AV)}}{\text{Scan rate } (\frac{V}{S})} \quad \textbf{(12)}$$

Thus: $$Q = \frac{9.7x10^{-4}\ (AV)}{0.01\ (\frac{V}{S})} \quad \textbf{(13)}$$

$$Q = 0.097\ As = 0.097\ coulombs$$

In a battery system the capacity units are Ampere-hour (Ah). Since 3600 As = 1 Ah.

Therefore: $$Q = (\frac{0.097\ As}{3600})Ah \quad \textbf{(14)}$$

$$Q = 2.7\ x10^{-5}\ Ah$$

For specific capacity to be calculated, the Q (electric charge) was obtained. Specific capacity is defined as capacity per gram of the active cathode material. The active mass = $1.52x10^{-5}$ g.

$$\text{Specific capacity} = \frac{Q}{\text{active mass}} \quad (15)$$

$$= \frac{2.7\ x10^{-5}\ \text{Ah}}{1.52x10^{-5}\ \text{g}}$$

$$= 0.177\ \text{Ah/g}$$

Specific capacity is usually expressed in mAh/g. therefore, the specific capacity becomes 0.177 Ah/g x 1000 = 177 mAh/g, the same procedure was adopted for all other capacity calculations with data obtained from cyclic voltammetry.

5.3. The scan studies

Fig 5.2 shows the obtained kinetic parameters of $LiFe_{0.5}Mn_{0.5}PO_4$-MWCNTs and $LiFe_{0.5}Mn_{0.5}PO_4$ from cyclic voltammetry at room temperature (298 K).

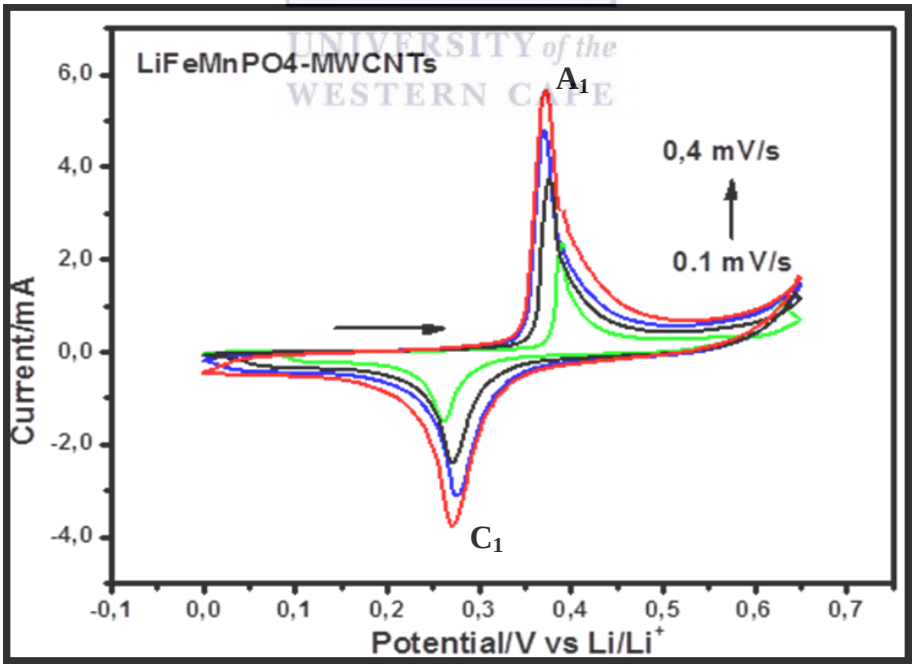

Figure 5.2: The effect of potential scan rate on the cyclic voltammograms of composite $LiFe_{0.5}Mn_{0.5}PO_4$-MWCNTs in 1 M $LiPF_6$ containing 1:1 v/v ethylene carbonate – dimethyl carbonate solvent mixture between 0.1 – 0.8 mV/s. Voltage range: 0.0 – 0.80 V.

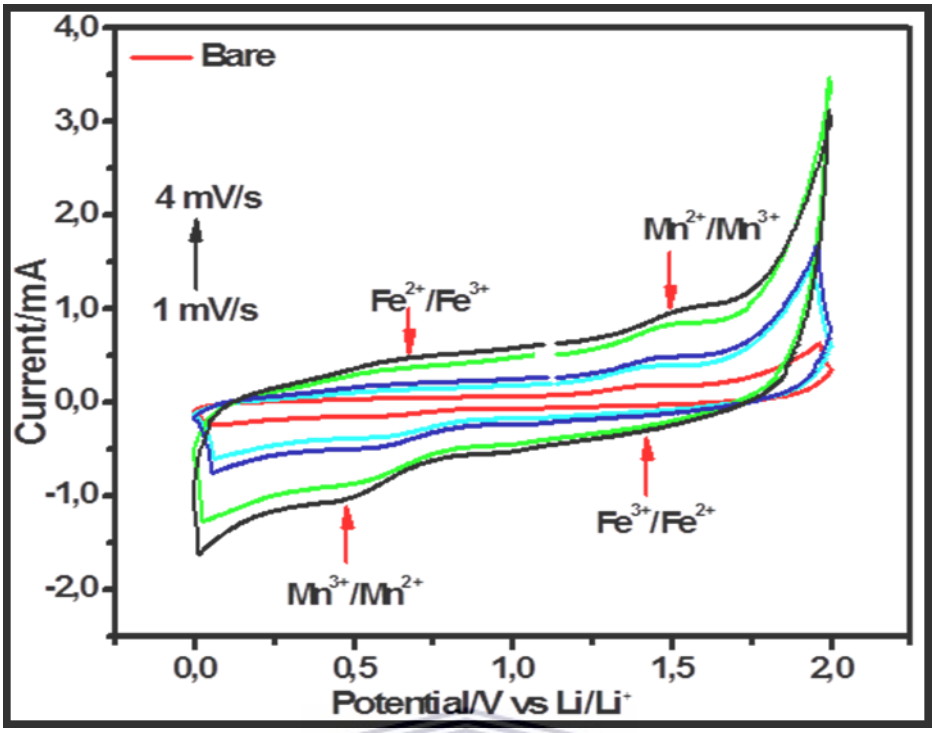

Figure 5.3: The effect of potential scan rate on the cyclic voltammograms of pristine $LiFe_{0.5}Mn_{0.5}PO_4$ in 1 M $LiPF_6$ containing 1:1 v/v ethylene carbonate – dimethyl carbonate solvent mixture between 0.1 – 0.8 mV/s. Voltage range: 0.0 – 3.0 V.

From **Fig. 5.2** There is a linear relationship between peak current and scan rates, the peak separation increases with increase in scan rate. All the CV profiles overlap regardless of the scan rate at the beginning of charging and discharging. $LiFe_{0.5}Mn_{0.5}PO_4$-MWCNTs composite electrode presents a larger peak current and a larger enclosed area as well as a smaller peak potential difference compared with those of the $LiFe_{0.5}Mn_{0.5}PO_4$ (**Fig. 5.3**) electrode at the same scan rate. These results indicate that the $LiFe_{0.5}Mn_{0.5}PO_4$-MWCNTs composite electrode has better reversibility and higher specific capacity in comparison with the $LiFe_{0.5}Mn_{0.5}PO_4$ electrode. The improvement of the composite electrode over pristine is due to the kinetic effects of the conductive multi-walled carbon nanotubes additive on the surface of $LiFe_{0.5}Mn_{0.5}PO_4$, which increases its electrochemical activity. The infused carbon nanotubes on the crystal lattice tend to have good effects by increasing the surface area of the electrode. Carbon nanotubes in these manner works as the host for lithium ion intercalation and extraction and provides good electronic contact between the electrode which has $LiFe_{0.5}Mn_{0.5}PO_4$ particles and the current collector through an overlap of the electrochemically active energies of the conductive gold particles (Chae *et al.*, 2009). Carbon nanotubes being in the nanoscale will help in enhancing the mobility of

electrons between the adjacent $LiFe_{0.5}Mn_{0.5}PO_4$ particles during the lithiation/delithiation process (Gyu-Chul *et al.,* 2005). The MWCNTs will interact with $LiFe_{0.5}Mn_{0.5}PO_4$ nanoparticles to form a 3D network which will easily facilitate lithium ion transport. Having a linear relationship between current and scan rates proves that $LiFe_{0.5}Mn_{0.5}PO_4$ and $LiFe_{0.5}Mn_{0.5}PO_4$-MWCNTs composite are both electroactive. However, $LiFe_{0.5}Mn_{0.5}PO_4$-MWCNTs composite has better conductivity.

A linear dependence of peak current on square root of scan rate was investigated. **Fig. 5.4** and **Fig. 5.5** were taken from the redox reactions of $Mn^{2+/3+}$ and $Mn^{2+/3+}$ which illustrate the scan rate dependence of the peak potentials (E_{pa} and E_{pc}) and peak currents (I_{pa} and I_{pc}) for $LiFe_{0.5}Mn_{0.5}PO_4$ and $LiFe_{0.5}Mn_{0.5}PO_4$-MWCNTs composite. E_{pa} and E_{pc} increases as scan rate increases. **Fig. 5.4** and **5.5** were used to calculate the Li^+ diffusion coefficient. For reversible reaction, the concentration is related to peak current by the Randles-Sevčik equation (at 25 °C). The Randles –Sevcik equation (Monk, 2001):

$$I_p = (2.69\text{x}10^5)\, n^{3/2} A D^{1/2} C V^{1/2} \qquad \textbf{(16)}$$

where n (1) is the number of electrons transferred, A (0.071 cm^2) is the area of the electrode, C (1 x 10^{-3} mol/cm^3) is the concentration of the bulk electrolyte solution and $I_p/v^{1/2}$ (0.7616 x 10^{-6}A $s^{1/2}$/ $V^{1/2}$) is the slope of the I_p versus $v^{1/2}$ linear plot (cathodic plots of **Fig. 5.4**) for $LiFe_{0.5}Mn_{0.5}PO_4$ and 0.9809 x 10^{-6}A $s^{1/2}$/ $V^{1/2}$) is the slope of the I_p versus $v^{1/2}$ linear plot (cathodic plots of **Fig. 5.5**) for $LiFe_{0.5}Mn_{0.5}PO_4$-MWCNTs composite. The diffusion coefficient, D, calculated for $LiFe_{0.5}Mn_{0.5}PO_4$ and $LiFe_{0.5}Mn_{0.5}PO_4$-MWCNTs composite was found to be 4.81 x 10^{-10} cm^2/s and 2 x 10^{-9} cm^2/s respectively which is close to the reported data for $LiFe_{0.5}Mn_{0.5}PO_4$ in organic electrolyte (Molenda *et al*., 2006). Hence, the electrochemical processes are diffusion controlled. The diffusion coefficient between the pristine and modified showed little difference even though the $LiFe_{0.5}Mn_{0.5}PO_4$-MWCNTs composite showed higher diffusion by an order of magnitude, meaning diffusion of lithium ions does not change much since it occurs in the solid bulk of the electrode materials which remains the same $LiFe_{0.5}Mn_{0.5}PO_4$ in the modified and pristine and in aqueous and non-aqueous electrolyte.

Table 4: The data represented on the table was obtained from the cyclic voltammetry of the $LiFe_{0.5}Mn_{0.5}PO_4$. The data was used to calculate coefficient diffusion.

Square root of Scan rates (V/s)	**Current (I_{Pa})**		**Current (I_{Pc})**	
	Fe^{2+}/ Fe^{3+}	**Mn^{2+}/ Mn^{3+}**	**Mn^{3+}/ Mn^{2+}**	**Fe^{3+}/ Fe^{2+}**
0.032	**0.121**	**0.369**	**-0.338**	**-0.179**
0.045	**0.175**	**0.493**	**-0.516**	**-0.268**
0.055	**0.369**	**0.829**	**-0.834**	**-0.444**
0.063	**0.458**	**1.007**	**-1.028**	**-0.533**

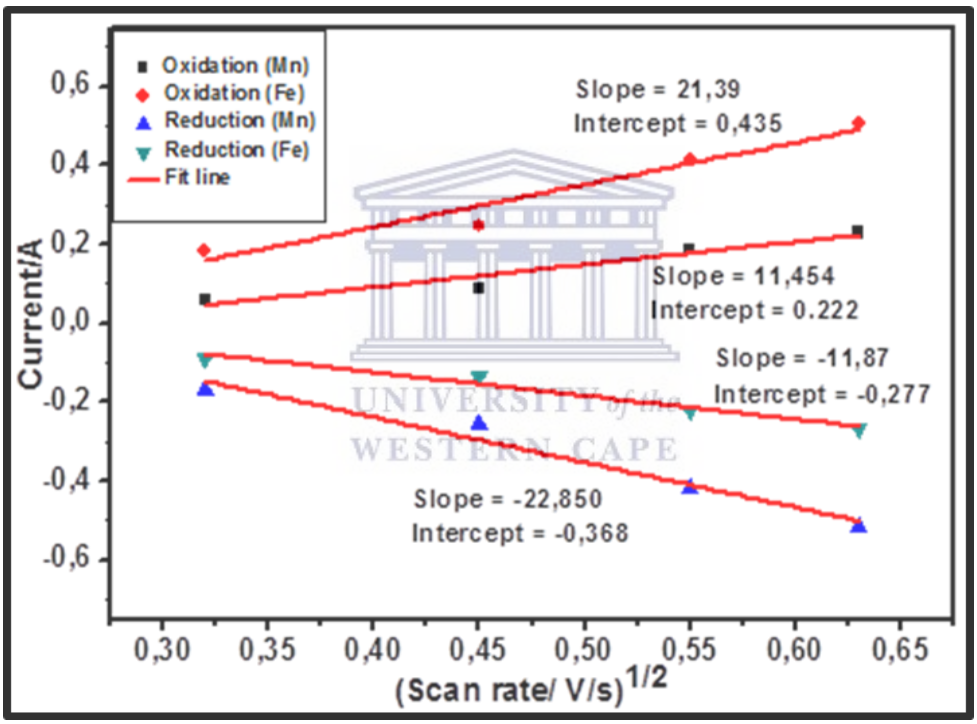

Figure 5.4: The plots of the (i) anodic peak potential as a function of potential scan rate (ii) cathodic peak potential as a function of potential scan rate for $LiFe_{0.5}Mn_{0.5}PO_4$.

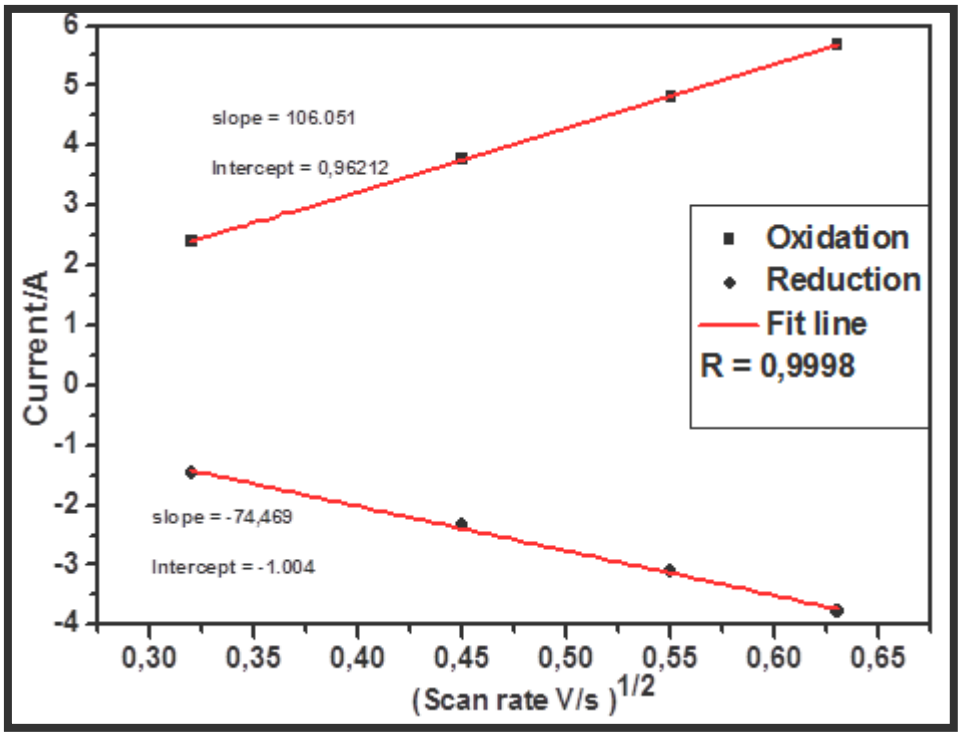

Figure 5.5: The plots of the (i) anodic peak potential as a function of potential scan rate (ii) cathodic peak potential as a function of potential scan rate for $LiFe_{0.5}Mn_{0.5}PO_4$-MWCNTs.

Table 5: The data represented on the table was obtained from the cyclic voltammetry of the $LiFeMnPO_4$-MWCNTs. The data was used to calculate coefficient diffusion.

Square root of Scan rates (V/s)	**Current (I_{Pa})**	**Current (I_{Pc})**
0.032	**2.395**	**-1.459**
0.045	**3.767**	**-2.341**
0.055	**4.811**	**-3.094**
0.063	**5.690**	**-3.779**

5.4. Electrochemical impedance spectroscopy (EIS)

EIS tests were conducted to evaluate the interfacial properties as well as the Li^+ migration activity of the two composite electrodes. The Nyquist plots are presented in **Fig 8:**

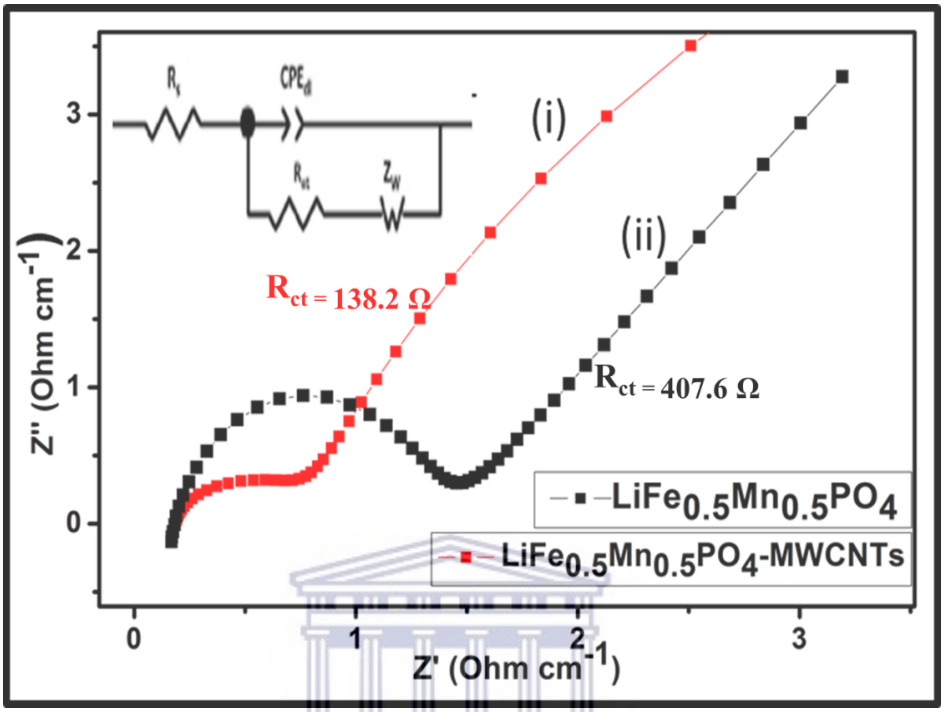

Figure 5.6: Comparative Nyquist plots (**i**) $LiFe_{0.5}Mn_{0.5}PO_4$-MWCNTs and (**ii**) $LiFe_{0.5}Mn_{0.5}PO_4$ at formal potential of 0.71 V vs. Li/Li^+ and perturbation amplitude of 10 mV.

Each plot have a well-defined, single semi-circle at high frequency and an inclined line at low frequency cause by the Warburg impedance related with lithium ion diffusion in the bulk of electrode, which illustrate that during lithium deinsertion/insertion, the kinetics of the electrode process is controlled by the diffusion process in the low frequency region and the charge transfer in the high frequency region (Hashambhoy *et al.*, 2011). An intercept of the semi-circle with *Z′*-axis in the very high frequency region identifies the Ohmic resistance (R_s) of the electrolyte and electrodes. The semicircle diameter at high frequency region on the *Z′*-axis is related to the charge transfer resistance (R_s) which controls the transfer kinetics at the electrode interface. Extrapolation of the semicircle to lower frequency regions gives intercept corresponding to (R_s + R_{ct}) from the R_{ct} value, which is extrapolated by subtracting the value of R_s. Impedance parameters were obtained by fitting from a modified Randles equivalent electrical circuit. CPE is the constant phase element

that models the double layer capacitance (C_d) which is due to surface roughness. The time constant (ɽ); exchange current (I_o) it measures the rate of charge exchange between oxidized and reduced species at any equilibrium potential without net overall charge (Husain, 2011), and heterogenous rate constant of electron transfer (K_{et}) were calculated according to the equation (Park *et al.,* 2003-Greef, *et al.,*1990-Bard *et al.,* 2001):

$$ɽ = \frac{1}{\omega} \quad \textbf{(17)}$$

$$\mathrm{Ret} = \frac{RT}{nF\mathrm{I}_{\circ}} \quad \textbf{(18)}$$

$$I_{\circ} = nFAKC \quad \textbf{(19)}$$

$$\mathrm{ket} = \frac{I_{\circ}}{nF\mathrm{AC}} \quad \textbf{(20)}$$

Where, ω_{max} is the angular frequency at the maximum impedance; R is the gas constant = 8.314 J/mol K (Greef *et al.,* 1990); T is the room temperature = 298 K; n is the number of electrons transferred per molecule of lithium = 1; F is the Faraday's constant = 96485 C/mol; A is the geometric area of electrode (16 mm diameter; measured from experiment) = 2.01 cm^2; C is the concentration of lithium ion in $LiFe_{0.5}Mn_{0.5}PO_4$ = 0.0228 mol/cm^3 (Hu *et al.,* 2013). The other parameters have their usual meanings. The calculated values are shown in **Table 6**.

Table 6: Obtained kinetic parameters of $LiFe_{0.5}Mn_{0.5}PO_4$-MWCNTs and $LiFe_{0.5}Mn_{0.5}PO_4$ from electrochemical impedance spectroscopy at room temperature (298 K).

Parameters	**$LiFe_{0.5}Mn_{0.5}PO_4$**	**$LiFe_{0.5}Mn_{0.5}PO_4$-MWCNTs**
τ/ s/rad	2.35 x 10^{-4}	1.21 x 10^{-5}
R_{ct}/ Ω	407.6	138.2
I_o/ A	6.30 x 10^{-5}	1.86 x 10^{-4}
K_{et}/ cm/s	9.2 x 10^{-6}	2.72 x 10^{-5}
σ/ Ω/$S^{1/2}$	22.65 2.21 x 10^{-17}	14.18 1.4 x 10^{-13}

Due to initial assumptions that $LiFe_{0.5}Mn_{0.5}PO_4$-MWCNTs, will perform better that the pristine $LiFe_{0.5}Mn_{0.5}PO_4$. According to the calculations which are referred as diffusion

coefficient (D), as indicated on table 6; above. It is evident from the table that the composite with lower value of σ has higher D value. The calculated D values are in good agreement with reported values by Prosini *et al* using similar technique. The superiority of the $LiFe_{0.5}Mn_{0.5}PO_4$-MWCNTs cathode composite over $LiFe_{0.5}Mn_{0.5}PO_4$ is further illustrated by the Bode plot phase shown in **Fig 5.7:**

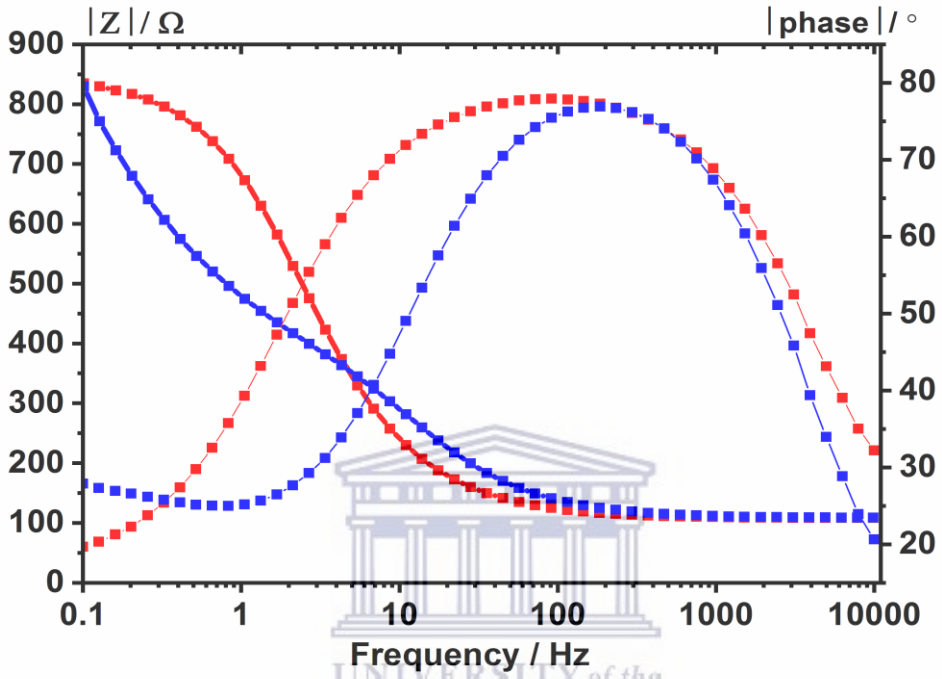

Figure 5.7: Comparative Bode phase-impedance diagrams of (i) $LiFe_{0.5}Mn_{0.5}PO_4$-MWCNTs and (ii) $LiFe_{0.5}Mn_{0.5}PO_4$ at perturbation amplitude of 5 mV.

At low frequencies (100 mHz) where the electronics of the electrode system are minimal perturbed and electrochemical equilibrium is almost maintained, the $LiFe_{0.5}Mn_{0.5}PO_4$-MWCNTs was observed to give lower impedance at 80.56 Ω with higher phase angle at 35.6˚ which indicates that it exhibit better conductive properties and faster kinetics than the $LiFe_{0.5}Mn_{0.5}PO_4$ with impedance and phase angle at 150.3 Ω and 19.7˚, respectively. This shows that the composite $LiFe_{0.5}Mn_{0.5}PO_4$-MWCNTs cathode gave better electrochemical reversibility and kinetics towards lithium ion transport within the electrode/electrolyte interface than the $LiFe_{0.5}Mn_{0.5}PO_4$.

5.5. Charge and discharge

The constant current charge and discharge modes was applied to evaluate the parameters; cell specific capacitance, specific energy, coulombs efficiency and cell stability. 0.01 A was used during the test as an average charge/discharge current. The charge and discharge were done within the potential range of 0.0 V - 2.0 V. The choice of potential range is informed from the electrolyte that was used, and the electrolyte that was $LiPF_6$. The decomposition voltage limit is theoretically 1.23 V or practically, in kinetic terms, between 1.3 V and 1.4 V (Panchal, *et al.,* 2018). $LiPF_6$ is soluble in water, high purity electrolytes are a core component of li-ion batteries. The most commonly used electrolyte is comprised of lithium salt, such as $LiPF_6$ in an organic solution. They are used since they have a very good conductivities and advantageously high equivalent conductivities in aqueous medium owing to the special mechanism of proton transport (proton hopping) that determine their conductance.

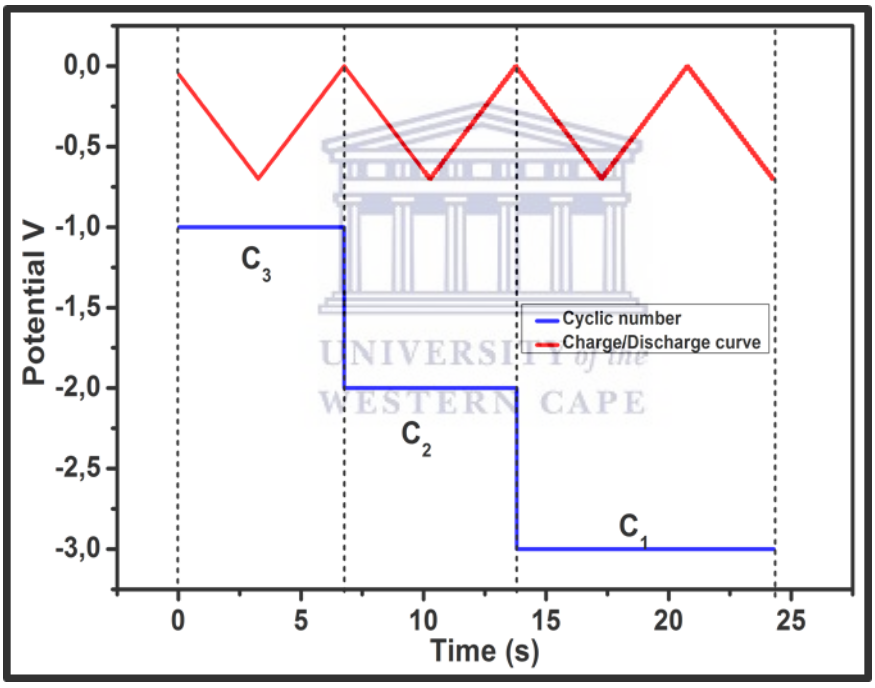

Figure 5.8: Charge/discharge curve of with the number of cycles

Figure 5.8; represent charge/discharge curves (a) $LiFe_{0.5}Mn_{0.5}PO_4$-MWCNTs and (b) $LiFe_{0.5}Mn_{0.5}PO_4$. The asymmetric lithium ion cell configuration assembled using the composite as cathode material and activated carbon as anode material for the first 10 cycles. Each branch of the circle starts with a voltage drop signifying the *IR* drop, due to the internal resistant of the cell. The different behavior of the first cycle is always due to the initial starting point where the whole system needs time to reach steady-state behavior.

When cyclic voltammetry charge is used specific capacitance, values depend on the scan rates and increases with increase in scan rates. When charge/discharge technique is used like galvanostatic-potentiation, the values reported depend on current densities. The values reported in literature (Yang *et al.*, 2013; khavan *et al.*, 2010), are therefore unique to the method used, conditions of measurements and whether a three or two electrode system was used. The material was found to be relatively very stable over many cycles. This simple means the material does not degrade when cycled numerous times. The (a) $LiFe_{0.5}Mn_{0.5}PO_4$-MWCNTs composite cathode was found that to have longer life cycle than $LiFe_{0.5}Mn_{0.5}PO_4$ (b).

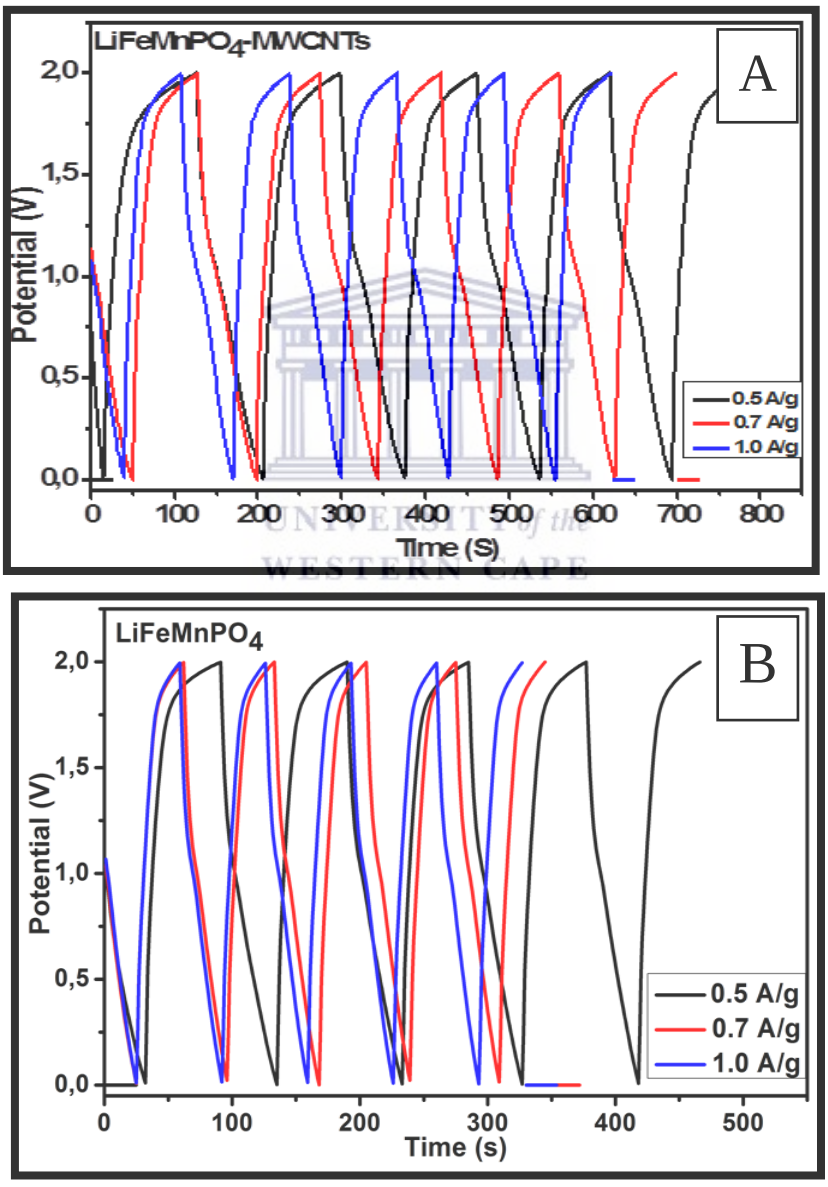

Figure 5.9: charge/discharge curves of (a) $LiFe_{0.5}Mn_{0.5}PO_4$-MWCNTs and (b) $LiFe_{0.5}Mn_{0.5}PO_4$.

CHAPTER 6
CONCLUSION AND RECOMMENDATIONS

6. Conclusion

The goal of this project was to explore lithium iron manganese phosphate ($LiFe_{0.5}Mn_{0.5}PO_4$) functionalized with MWCNTs as cathode material and study the conductivity of the $LiFe_{0.5}Mn_{0.5}PO_4$ vs. $LiFe_{0.5}Mn_{0.5}PO_4$-MWCNTs composite for possible use as cathode material in lithium ion batteries. Lithium iron manganese phosphate ($LiFe_{0.5}Mn_{0.5}PO_4$) was synthesized via simple facile microwave approach which formed nanomaterials in a range 10-50 nm. The nanoscale dimensions enhanced the electrochemical performance and the Li-ion diffusion. The smaller dimension facilitated short diffusion length of Li ion in the discharge and charge procedures to improve ion conductivity of the material. The formation of the nanocrystalline phase pristine and MWCNTs coated $LiFe_{0.5}Mn_{0.5}PO_4$ nanoparticles were confirmed from the analysis of the XRD and FTIR results. Both $LiFe_{0.5}Mn_{0.5}PO_4$ and $LiFe_{0.5}Mn_{0.5}PO_4$-MWCNTs composite samples were identified as a double-phase olivine, confirming that the $LiFe_{0.5}Mn_{0.5}PO_4$ olivine structural integrity was maintained after modification. Further XRD analysis revealed that $LiFe_{0.5}Mn_{0.5}PO_4$-MWCNTs could not retain its orthorhombic structure in the presence of MWCNTs diffraction peaks, which confirms that the MWCNTs has been coated onto $LiFe_{0.5}Mn_{0.5}PO_4$ with a tread-like topography showing the presence of carbon nanotubes. The diffraction results demonstrate a high degree of crystallinity and uniformity. Raman and FTIR confirmed that the material contains phosphate group which is present in the structure of olivine cathode material $LiFe_{0.5}Mn_{0.5}PO_4$. EIS and CV results revealed that $LiFe_{0.5}Mn_{0.5}PO_4$-MWCNTs composite exhibited better electrochemical activity shown by low charge-transfer resistance and well-defined redox couples. From the CV, it was observed that $LiFe_{0.5}Mn_{0.5}PO_4$ and $LiFe_{0.5}Mn_{0.5}PO_4$-MWCNTs composite can be described as reversible reaction systems with resistive behavior. The diffusion coefficients as well as the charge/discharge capacities were calculated using cyclic voltammetry and it showed that $LiFe_{0.5}Mn_{0.5}PO_4$-MWCNTs composite has higher diffusion coefficient. The charge and discharge capacities of $LiFe_{0.5}Mn_{0.5}PO_4$-MWCNTs

composite and $LiFe_{0.5}Mn_{0.5}PO_4$ were calculated using CV at 10 mV/s scan rates and it proved that $LiFe_{0.5}Mn_{0.5}PO_4$-MWCNTs composite possesses higher charge/discharge capacities. The discharge capacity is about ~93% closer to the value reported for theoretical $LiFe_{0.5}Mn_{0.5}PO_4$ cathode material. This study suggests that the modification of $LiFe_{0.5}Mn_{0.5}PO_4$ with MWCNTs provides a new facile approach for producing alternative $LiFe_{0.5}Mn_{0.5}PO_4$ cathode material for lithium ion batteries with improved electrochemical properties. $LiFe_{0.5}Mn_{0.5}PO_4$ properties have been influenced by carbon coating in the previous studies of $LiFe_{0.5}Mn_{0.5}PO_4$, but carbon tends to not be electrochemically active depending on the amount of carbon used. Carbon amount must be in equal amounts with the material used in order to increase the loading of active material within a given volume of lithium ion batteries, so to increase the energy density. The novelty of this work is mainly in the use of MWCNTs as surface coating materials for the enhancement of the electrochemical performance $LiFe_{0.5}Mn_{0.5}PO_4$ cathode material. The carbon works as the host for lithium ion intercalation and extraction and provides good electronic contact between the electrode which has $LiFe_{0.5}Mn_{0.5}PO_4$ particles and the current collector through an overlap of the electrochemically active energies of the conductive carbon particles. The surface coating acts as a protective layer to prevent cathode corrosion during cycling. This is the first time that $LiFe_{0.5}Mn_{0.5}PO_4$-MWCNTs composite is reported on.

6.1 Recommendations and future work

1) In this work the three electrodes system was used which does not provide the consistent information although it is applicable for battery testing. In order to get good and consistent results for a battery testing, a coin cell must be assembled.
2) The use of other electrolyte in cyclic voltammetry and electrochemical impedance spectroscopy is necessary for further comparison with the worked that has been done.
3) Furthermore, this research work has however not explored the electronic configurations in olivine structure and Multi-walled carbon nanotubes were not synthesized they were commercially purchased without modifications; hence SEM, TEM and XRD only were reported.
4) In future work, X-ray photoelectron spectroscopy (XPS) which can measure the elemental composition at the parts per thousand range, empirical formula, chemical state and electronic state of the elements that exist within a material, will be

employed. Which will be helpful when compared with results obtained from SAXS. Results obtained may be further used to verify the present proposed mechanism for enhanced electronic conductivity, and to provide more insight for new cathode material design.

REFERENCE

ABELA, R., BRAUN, H., MING, P., PEDROZZI, M., QUITMANN, C., REICHE, S., DAALEN, M. V., VAN DER VEEN, J., MESOT, J. & SHIROKA, T. **2009**. Ultrafast phenomena at the nanoscale: science opportunities at the SwissFEL X-ray laser. Paul Scherrer Institute (PSI), Villigen (Switzerland).

ALONSO, J., DIAMANT, R., CASTILLO, P., ACOSTA–GARCÍA, M., BATINA, N. & HARO-PONIATOWSKI, E. **2009**. Thin films of silver nanoparticles deposited in vacuum by pulsed laser ablation using a YAG: Nd laser. Applied Surface Science, 255**,** 4933-4937.

AMATUCCI, G., TARASCON, J. & KLEIN, L. **1996**. Cobalt dissolution in LiCoO2 non-aqueous rechargeable batteries. Solid State Ionics, 83**,** 167-173.

AMDOUNI, N., ZAGHIB, K., GENDRON, F., MAUGER, A. & JULIEN, C. **2006**. Structure and insertion properties of disordered and ordered LiNi0.5Mn1.5O4 spinels prepared by wet chemistry. Ionics, 12**,** 117-126.

ARICÒ, A. S., BRUCE, P., SCROSATI, B., TARASCON, J.-M. & VAN SCHALKWIJK, W. **2005**. Nanostructured materials for advanced energy conversion and storage devices. Nature materials, 4**,** 366-377.

ARIGA, K., KROTO, H. & O'BRIEN, P. **2012**. Manipulation of Nanoscale Materials: An Introduction to Nanoarchitectonics, Royal Society of Chemistry.

AURBACH, D., EIN-ELY, Y. & ZABAN, A. **1994**. The surface chemistry of lithium electrodes in alkyl carbonate solutions. Journal of the Electrochemical Society, 141**,** L1-L3.

AURBACH, D., ZABAN, A., EIN-ELI, Y., WEISSMAN, I., CHUSID, O., MARKOVSKY, B., LEVI, M., LEVI, E., SCHECHTER, A. & GRANOT, E. **1997**. Recent

studies on the correlation between surface chemistry, morphology, three-dimensional structures and performance of Li and Li-C intercalation anodes in several important electrolyte systems. Journal of Power Sources, 68**,** 91-98. 107.

AUTENBOER, W. **2006**. SUBAT: An assessment of sustainable battery technology. Journal of Power Sources, 162**,** 913-919.

BALAJI, S., MANICHANDRAN, T. & MUTHARASU, D. **2012**. A comprehensive study on influence of Nd3+ substitution on properties of LiMn2O4. Bulletin of Materials Science, 35**,** 471-480.

BALAYA, P., BHATTACHARYYA, A. J., JAMNIK, J., ZHUKOVSKII, Y. F., KOTOMIN, E. A. & MAIER, J. **2006**. Nano-ionics in the context of lithium batteries. Journal of Power Sources, 159**,** 171-178.

BARD, A. J. & FAULKNER, L. R. **1980**. Electrochemical methods: fundamentals and applications, Wiley New York.

BAZITO, F. F. & TORRESI, R. M. **2006**. Cathodes for lithium ion batteries: the benefits of using nanostructured materials. Journal of the Brazilian Chemical Society, 17**,** 627-642.

BENBOW, E., KELLY, S., ZHAO, L., REUTENAUER, J. & SUIB, S. **2011**. Oxygen reduction properties of bifunctional α-manganese oxide electrocatalysts in aqueous and organic electrolytes. The Journal of Physical Chemistry C, 115**,** 22009-22017.

BESENHARD, J. & EICHINGER, G. **1976**. High energy density lithium cells: Part I. Electrolytes and anodes. Journal of Electroanalytical Chemistry and Interfacial Electrochemistry, 68**,** 1-18.

BRUCE, P. G., SCROSATI, B. & TARASCON, J. M. **2008**. Nanomaterials for rechargeable lithium batteries. Angewandte Chemie International Edition, 47**,** 2930-2946.

CAO, G. **2004**. Synthesis, Properties and Applications, World Scientific.

CHAN, H. W., DUH, J. G. & SHEEN, S. R. **2003b**. LiMn2O4 cathode doped with excess lithium and synthesized by co-precipitation for Li-ion batteries. Journal of Power Sources, 115**,** 110-118.

CHAN, H., DUH, J. & SHEEN, S. **2003a**. LiMn2O4 cathode doped with excess lithium and synthesized by co-precipitation for Li-ion batteries. Journal of Power Sources, 115**,** 110-118.

CHAN, H.-W., DUH, J.-G. & LEE, J.-F. **2006**. Valence change by in situ XAS in surface modified LiMn2O4 for Li-ion battery. Electrochemistry Communications, 8**,** 1731-1736.

CHAN, H.-W., DUH, J.-G., SHEEN, S.-R., TSAI, S.-Y. & LEE, C.-R. **2005**. New surface modified material for LiMn2O4 cathode material in Li-ion battery. Surface and Coatings Technology, 200**,** 1330-1334.

CHANG, S. H., RYU, K. S., KIM, K. M., KIM, M. S., KIM, I. K. & KANG, S. G. **1999**.

CHERSTIOUK, O., SIMONOV, P. & SAVINOVA, E. **2003**. Model approach to evaluate particle size effects in electrocatalysis: preparation and properties of Pt nanoparticles supported on GC and HOPG. Electrochimica Acta, 48**,** 3851-3860.

CHURIKOV, A., KACHIBAYA, E., SYCHEVA, V., IVANISHCHEVA, I., IMNADZE, R., PAIKIDZE, T. & IVANISHCHEV, A. **2009**. Electrochemical properties of LiMn2−yMeyO4 (Me= Cr, Co, Ni) spinels as cathodic materials for lithium-ion batteries. Russian Journal of Electrochemistry, 45**,** 175-182.

CURTIS, C. J., WANG, J. & SCHULZ, D. L. **2004**. Preparation and Characterization of LiMn2O4 Spinel Nanoparticles as Cathode Materials in Secondary Li Batteries. Journal of the Electrochemical Society, 151**,** A590-A598.

DAHN, J., FULLER, E., OBROVAC, M. & VON SACKEN, U. **1994**. Thermal stability of LixCoO2, LixNiO2 and λ-MnO2 and consequences for the safety of Li-ion cells. Solid State Ionics, 69**,** 265-270.

DANIEL, M.-C. & ASTRUC, D. **2004**. Gold nanoparticles: assembly, supramolecular chemistry, quantum-size-related properties, and applications toward biology, catalysis, and nanotechnology. Chemical Reviews, 104**,** 293-346.

DEVARAJAN, S., VIMALAN, B. & SAMPATH, S. **2004**. Phase transfer of Au–Ag alloy nanoparticles from aqueous medium to an organic solvent: effect of aging of surfactant on the formation of Ag-rich alloy compositions. Journal of Colloid and Interface Science, 278**,** 126- 132.

DOEFF, M. M. **2013**. Battery Cathodes. Batteries for Sustainability. Springer.

DRESSELHAUS, M., THOMAS, I., GRÄTZEL, M., STEELE, B. C., HEINZEL, A., SCHLAPBACH, L., ZÜTTEL, A., TARASCON, J. & ARMAND, M. **2001**. Materials for clean energy. Nature, 414**,** 332-337.

DU, G., SHARMA, N., PETERSON, V. K., KIMPTON, J. A., JIA, D. & GUO, Z. **2011**. Br-Doped Li4Ti5O12 and Composite TiO2 Anodes for Li-ion Batteries: Synchrotron X-Ray and in situ Neutron Diffraction Studies. Advanced Functional Materials, 21**,** 3990-3997.

EFTEKHARI, A. **2003**. Mixed-Metals Codeposition as a Novel Method for the Preparation of LiMn2O4 Electrodes with Reduced Capacity Fades. Journal of the Electrochemical Society, 150**,** A966-A969.

EICHINGER, G. & BESENHARD, J. O. **1976**. High energy density lithium cells: Part II. Cathodes and complete cells. Journal of Electroanalytical Chemistry and Interfacial Electrochemistry, 72**,** 1-31.

EIN-ELI, Y., URIAN, R., WEN, W. & MUKERJEE, S. **2005**. Low temperature performance of copper/nickel modified LiMn2O4 spinels. Electrochimica Acta, 50**,** 1931-1937.

Electrochemical properties of cobalt-exchanged spinel lithium manganese oxide. Journal of Power Sources, 84**,** 134-137.

FERGUS, J. W. **2010**. Recent developments in cathode materials for lithium ion batteries. Journal of Power Sources, 195**,** 939-954.

FERRANDO, R., JELLINEK, J. & JOHNSTON, R. L. **2008**. Nanoalloys: From theory to applications of alloy clusters and nanoparticles. Chem. Rev., 108**,** 845-910.

FEY, G., WANG, K. & YANG, S. **1997**. New inverse spinel cathode materials for rechargeable lithium batteries. Journal of Power Sources, 68**,** 159-165.1-27.

GOSSER, D. K. **1993**. Cyclic voltammetry: simulation and analysis of reaction mechanisms, VCH New York.

GUMMOW, R., DE KOCK, A. & THACKERAY, M. **1994**. Improved capacity retention in rechargeable 4 V lithium/lithium-manganese oxide (spinel) cells. Solid State Ionics, 69**,** 59- 67.

GUYOMARD, D. & TARASCON, J. **1994**. The carbon/Li1+xMn2Osystem. Solid State Ionics, 69**,** 222-237.

HA, H.-W., YUN, N. J. & KIM, K. **2007**. Improvement of electrochemical stability of LiMn2O4 by CeO2 coating for lithium-ion batteries. Electrochimica Acta, 52**,** 3236-3241.
Hallam, S. Infrared Absorption Spectroscopy-Theoritical Principles. University Biosciences Online Learning, **2010**. March 12, **2014**.

HEBIÉ, S., KOKOH, K. B., SERVAT, K. & NAPPORN, T. **2013**. Shape-dependent electrocatalytic activity of free gold nanoparticles toward glucose oxidation. Gold Bulletin, 46**,** 311-318.

HU, M. Z. & EASTERLY, C. E. **2009**. A novel thermal electrochemical synthesis method for production of stable colloids of “naked” metal (Ag) nanocrystals. Materials Science and Engineering: C, 29**,** 726-736.

HU, M., PANG, X. & ZHOU, Z. **2013**. Recent progress in high-voltage lithium ion batteries. Journal of Power Sources, 237**,** 229-242.

HUANG, X. & EL-SAYED, M. A. **2010**. Gold nanoparticles: optical properties and implementations in cancer diagnosis and photothermal therapy. Journal of Advanced Research, 1**,** 13-28.

HUNTER, J. C. **1981**. Preparation of a new crystal form of manganese dioxide: λ-MnO2. Journal of. Solid State Chemistry, 39**,** 142-147.

HUSAIN, I. **2011**. Electric and hybrid vehicles: design fundamentals, CRC press.

JANG, D. H., SHIN, Y. J. & OH, S. M. **1996**. Dissolution of Spinel Oxides and Capacity Losses in 4 V Li/LxMn2O4 Cells. Journal of the Electrochemical Society, 143**,** 2204-2211.

JIANG, Z. & ABRAHAM, K. **1996**. Preparation and Electrochemical Characterization of Micron-Sized Spinel LiMn2O4. Journal of the Electrochemical Society, 143**,** 1591-1598.

KAKUDA, T., UEMATSU, K., TODA, K. & SATO, M. **2007**. Electrochemical performance of Al-doped LiMn2O4 prepared by different methods in solid-state reaction. Journal of Power Sources, 167**,** 499-503.

KAMARULZAMAN, N., YUSOFF, R., KAMARUDIN, N., SHAARI, N., ABDUL AZIZ, N., BUSTAM, M., BLAGOJEVIC, N., ELCOMBE, M., BLACKFORD, M. & AVDEEV, M. **2009**. Investigation of cell parameters, microstructures and electrochemical behaviour of LiMn2O4normal and nano powders. Journal of Power Sources, 188**,** 274-280.

KIANI, M., MOUSAVI, M. & RAHMANIFAR, M. **2011**. Synthesis of Nano-and Micro-Particles of LiMn2O4: Electrochemical Investigation and Assessment as a Cathode in Li Battery. Int. J. Electrochem. Sci, 6**,** 2581-2595.

KIM, K. W., LEE, S.-W., HAN, K.-S., CHUNG, H. J. & WOO, S. I. **2003**. Characterization of Al-doped spinel LiMn2O4 thin film cathode electrodes prepared by

Liquid Source Misted Chemical Deposition (LSMCD) technique. Electrochimica Acta, 48**,** 4223-4231.

KIRKLAND, A. & HUTCHISON, J. **2007**. Nanocharacterisation, Royal Society of Chemistry.

KURIBAYASHI, I., YOKOYAMA, M. & YAMASHITA, M. **1995**. Battery characteristics with various carbonaceous materials. Journal of Power Sources, 54**,** 1-5.

LANGILLE, M. R., PERSONICK, M. L., ZHANG, J. & MIRKIN, C. A. **2012**. Defining rules for the shape evolution of gold nanoparticles. Journal of the American Chemical Society, 134**,** 14542-14554.

LENG, Y. **2008**. X-Ray Diffraction Methods. Materials Characterization. John Wiley & Sons (Asia) Pte Ltd.

LI, X. & XU, Y. **2008**. Enhanced cycling performance of spinel LiMn2O4 coated with ZnMn2O4 shell. Journal of Solid State Electrochemistry, 12**,** 851-855.

LIANG, R.-F., WANG, Z.-X., GUO, H.-J., LI, X.-H., PENG, W.-J. & WANG, Z.-G. **2008**. Fabrication and electrochemical properties of lithium-ion batteries for power tools. Journal of Power Sources, 184**,** 598-603.

LIU, D.-Q., HE, Z.-Z. & LIU, X.-Q. **2007a**. Synthesis and characterization of LiGaxMn2−xO4 (0≤< i> x</i>≤ 0.05) by triethanolamine-assisted sol–gel method. Journal of Alloys and Compounds, 440**,** 69-73.

LIU, D.-Q., LIU, X.-Q. & HE, Z.-Z. **2007b**. The elevated temperature performance of LiMn2O4 coated with Li4Ti5O12 for lithium ion battery. Materials Chemistry and Physics, 105**,** 362-366.

LIU, H., WU, Y., RAHM, E., HOLZE, R. & WU, H. **2004**. Cathode materials for lithium ion batteries prepared by sol-gel methods. Journal of Solid State Electrochemistry, 8**,** 450-466.

LIU, Q., WANG, S., TAN, H., YANG, Z. & ZENG, J. **2013**. Preparation and Doping Mode of Doped LiMn2O4 for Li-Ion Batteries. Energies, 6**,** 1718-1730.

LIU, Y., FUJIWARA, T., YUKAWA, H. & MORINAGA, M. **2001**. Electrochim. Acta, 46**,** 1151.

Liu, Y., Yao, W., Lei, C., Zhang, Q., Zhong, S. and Yan, Z., **2019**. Ni-Rich Oxide LiNi0. 85Co0. 05Mn0. 1O2 for Lithium Ion Battery: Effect of Microwave Radiation on Its Morphology and Electrochemical Property. *Journal of The Electrochemical Society*, *166*(8), pp.A1300-A1309.

LU, Z., MACNEIL, D. & DAHN, J. **2001**. Layered cathode materials Li[NixLi(1/3−2x/3)Mn(2/3−x/3)]O2 for lithium-ion batteries. Electrochemical and solid-state letters, 4**,** A191-A194.

MACDONALD, D. D. **2006**. Reflections on the history of electrochemical impedance spectroscopy. Electrochimica Acta, 51**,** 1376-1388.

MARTIN, L. **2013**. Etude de l'oxyde de cuivre CuO, matériau de conversion en film mince pour microbatteries au lithium: caractérisation des processus électrochimiques et chimiques en cyclage. Pau.

MCFARLAND, A. D., HAYNES, C. L., MIRKIN, C. A., VAN DUYNE, R. P. & GODWIN, H. A. **2004**. Color my nanoworld. Journal of Chemical Education, 81**,** 544A.

MENG, Y. S. & ARROYO-DE DOMPABLO, M. E. **2009**. First principles computational materials design for energy storage materials in lithium ion batteries. Energy & Environmental Science, 2**,** 589-609.

MOHAMEDI, M., TAKAHASHI, D., UCHIYAMA, T., ITOH, T., NISHIZAWA, M. & UCHIDA, I. **2001**. Explicit analysis of impedance spectra related to thin films of spinel LiMn2O4. Journal of Power Sources, 93**,** 93-103.

MONK, P. M. **2008**. Fundamentals of electro-analytical chemistry, John Wiley & Sons.

NAGAURA, T. & TOZAWA, K. **1990**. Lithium ion rechargeable battery. Prog. Batteries Solar Cells, 9**,** 209.

NAGHASH, A. & LEE, J. Y. **2000**. Preparation of spinel lithium manganese oxide by aqueous co-precipitation. Journal of Power Sources, 85**,** 284-293.

Nayak, P.K., Erickson, E.M., Schipper, F., Penki, T.R., Munichandraiah, N., Adelhelm, P., Sclar, H., Amalraj, F., Markovsky, B. and Aurbach, D., **2018**. Review on challenges and recent advances in the electrochemical performance of high capacity Li- and Mn- rich cathode materials for Li- ion batteries. *Advanced Energy Materials*, *8*(8), p.1702397.

ODANI, A., NIMBERGER, A., MARKOVSKY, B., SOMINSKI, E., LEVI, E., KUMAR, V., MOTIEI, M., GEDANKEN, A., DAN, P. & AURBACH, D. **2003**. Development and testing of nanomaterials for rechargeable lithium batteries. Journal of Power Sources, 119**,** 517-521.

OH, S. W., MYUNG, S.-T., BANG, H. J., YOON, C. S., AMINE, K. & SUN, Y.-K. **2009**. Nanoporous structured LiFePO4 with spherical microscale particles having high volumetric capacity for lithium batteries. Electrochemical and solid-state letters, 12**,** A181-A185. 114.

OKADA, M., LEE, Y.-S. & YOSHIO, M. **2000**. Cycle characterizations of LiMxMn2-xO4 (M = Co, Ni) materials for lithium secondary battery at wide voltage region. Journal of Power Sources, 90**,** 196-200.

Panchal, S., Mathew, M., Fraser, R. and Fowler, M., **2018**. Electrochemical thermal modeling and experimental measurements of 18650 cylindrical lithium-ion battery during discharge cycle for an EV. *Applied Thermal Engineering*, *135*, pp.123-132.

PAL, A., SHAH, S., KULKARNI, V., MURTHY, R. & DEVI, S. **2009**. Template free synthesis of silver–gold alloy nanoparticles and cellular uptake of gold nanoparticles in Chinese Hamster Ovary cell. Materials Chemistry and Physics, 113**,** 276-282.

PAULSEN, J., THOMAS, C. & DAHN, J. **2000**. O2 Structure Li2/3[Ni1/3Mn2/3]O2: A New Layered Cathode Material for Rechargeable Lithium Batteries. I. Electrochemical Properties. Journal of the Electrochemical Society, 147**,** 861-868.

PISTOIA, G. & WANG, G. **1993**. Aspects of the Li+insertion into LixMn2O4 for 0<< i> x</i>< 1. Solid State Ionics, 66**,** 135-142.

PISTOIA, G., ANTONINI, A., ROSATI, R., BELLITTO, C. & INGO, G. **1997**. Doped Li-Mn spinels: physical/chemical characteristics and electrochemical performance in Li batteries. Chemistry of materials, 9**,** 1443-1450.

POLO FONSECA, C., BELLEI, M., AMARAL, F., CANOBRE, S. & NEVES, S. **2009**. Synthesis and characterization of LiMxMn2-xO4 (M = Al, Bi and Cs ions) films for lithium ion batteries. Energy Conversion and Management, 50**,** 1556-1562.

PRÖLL, J., KOHLER, R., TORGE, M., ULRICH, S., ZIEBERT, C., BRUNS, M., SEIFERT, H. & PFLEGING, W. **2011**. Laser microstructuring and annealing processes for lithium manganese oxide cathodes. Applied Surface Science, 257**,** 9968-9976.

RAJA, M. W., MAHANTY, S. & BASU, R. N. **2009**. Influence of S and Ni co-doping on structure, band gap and electrochemical properties of lithium manganese oxide synthesized by soft chemical method. Journal of Power Sources, 192**,** 618-626.

RAO, M. M., LIEBENOW, C., JAYALAKSHMI, M., WULFF, H., GUTH, U. & SCHOLZ, F. **2001**. High-temperature combustion synthesis and electrochemical characterization of LiNiO2, LiCoO2 and LiMn2O4 for lithium-ion secondary batteries. Journal of Solid State Electrochemistry, 5**,** 348-354. 115.

ROBERTSON, A., LU, S., AVERILL, W. & HOWARD, W. **1997**. M3+-Modified LiMn2O4 Spinel Intercalation Cathodes I. Admetal Effects on Morphology and Electrochemical Performance. Journal of the Electrochemical Society, 144**,** 3500-3505.

RODRIGUEZ-CARVAJAL, J., ROUSSE, G., MASQUELIER, C. & HERVIEU, M. **1998**. Electronic crystallization in a lithium battery material: columnar ordering of electrons and holes in the spinel LiMn2O4. Physical review letters, 81**,** 4660.

ROSSOUW, M., DE KOCK, A., DE PICCIOTTO, L., THACKERAY, M., DAVID, W. & IBBERSON, R. **1990**. Structural aspects of lithium-manganese-oxide electrodes for rechargeable lithium batteries. Materials research bulletin, 25**,** 173-182.

SAIDI, M., BARKER, J., HUANG, H., SWOYER, J. & ADAMSON, G. **2003**. Performance characteristics of lithium vanadium phosphate as a cathode material for lithium-ion batteries. Journal of Power Sources, 119**,** 266-272.

SAU, T. K. & MURPHY, C. J. **2004**. Room temperature, high-yield synthesis of multiple shapes of gold nanoparticles in aqueous solution. Journal of the American Chemical Society, 126**,** 8648-8649.

SCHOONMAN, J., TULLER, H. & KELDER, E. **1999**. Defect chemical aspects of lithium-ion battery cathodes. Journal of Power Sources, 81**,** 44-48.

SHAFIEE, S. & TOPAL, E. **2009**. When will fossil fuel reserves be diminished? Energy Policy, 37**,** 181-189.

SHI, J. Y., YI, C.-W. & KIM, K. 2**010**. Improved electrochemical performance of AlPO4-coated LiMn1.5Ni0.5O4 electrode for lithium-ion batteries. Journal of Power Sources, 195**,** 6860-6866.

SHI, Y., TANG, H., JIANG, S., KAYSER, L.V., LI, M., LIU, F., JI, F., LIPOMI, D.J., ONG, S.P. and CHEN, Z., **2018**. Understanding the electrochemical properties of naphthalene diimide: implication for stable and high-rate lithium-ion battery electrodes. *Chemistry of Materials*, *30*(10), pp.3508-3517.

SHIN, Y., BAE, I.-T., AREY, B. W. & EXARHOS, G. J. **2008**. Facile stabilization of gold-silver alloy nanoparticles on cellulose nanocrystal. The Journal of Physical Chemistry C, 112**,** 4844-4848. 116.

SIDES, C. R., CROCE, F., YOUNG, V. Y., MARTIN, C. R. & SCROSATI, B. **2005**. A High-Rate, Nanocomposite LiFePO4⁄ Carbon Cathode. Electrochemical and solid-state letters, 8**,** A484-A487.

SON, J., PARK, K., KIM, H. & CHUNG, H. **2004**. Surface-modification of LiMn2O4 with a silver-metal coating. Journal of Power Sources, 126**,** 182-185.

STAROWICZ, M., STYPUŁA, B. & BANAŚ, J. **2006**. Electrochemical synthesis of silver nanoparticles. Electrochemistry Communications, 8**,** 227-230.

SUN, H., CHEN, Y., XU, C., ZHU, D. & HUANG, L. **2012**. Electrochemical performance of rare-earth doped LiMn2O4 spinel cathode materials for Li-ion rechargeable battery. Journal of Solid State Electrochemistry, 16**,** 1247-1254.

TALEB, A., PETIT, C. & PILENI, M. **1997**. Synthesis of highly monodisperse silver nanoparticles from AOT reverse micelles: a way to 2D and 3D self-organization. Chemistry of materials, 9**,** 950-959.

TAN, S. M. & JOHAN, M. R. **2011**. Effects of MnO2 nano-particles on the conductivity of PMMA-PEO-LiClO4-EC polymer electrolytes. Ionics, 17**,** 485-490.

TARASCON, J. M. & ARMAND, M. **2001**. Issues and challenges facing rechargeable lithium batteries. Nature, 414**,** 359-367.

TARASCON, J., COOWAR, F., AMATUCI, G., SHOKOOHI, F. & GUYOMARD, D. **1995**. The Li1+xMn2O4 C system Materials and electrochemical aspects. Journal of Power Sources, 54**,** 103-108.

TAY, S. F. & JOHAN, M. R. **2010**. Synthesis, structure, and electrochemistry of Ag-modified LiMn2O4 cathode materials for lithium-ion batteries. Ionics, 16**,** 859-863.

THACKERAY, M. **1995**. Structural considerations of layered and spinel lithiated oxides for lithium ion batteries. Journal of the Electrochemical Society, 142**,** 2558-2563. 117

THACKERAY, M., DE KOCK, A. & DAVID, W. **1993**. Synthesis and structural characterization of defect spinels in the lithium-manganese-oxide system. Materials research bulletin, 28**,** 1041-1049.

THIRUNAKARAN, R., KIM, K.-T., KANG, Y.-M. & LEE, J.-Y. **2004**. Solution synthesis of boron substituted LiMn2O4 spinel oxide for use in lithium rechargeable battery. Ionics, 10**,** 188-192.

TU, J., ZHAO, X., CAO, G., ZHUANG, D., ZHU, T. & TU, J. **2006**. Enhanced cycling stability of LiMn2O4 by surface modification with melting impregnation method. Electrochimica Acta, 51**,** 6456-6462.

VAN DEN BOSSCHE, P., VERGELS, F., VAN MIERLO, J., MATHEYS, J. & VAN

WANG, G., WANG, J., MAO, W., SHAO, H., ZHANG, J. & CAO, C. **2005**. Physical properties and electrochemical performance of LiMn2O4 cathode materials prepared by a precipitation method. Journal of Solid State Electrochemistry, 9**,** 524-530.

WANG, J. & SUN, X. **2012**. Understanding and recent development of carbon coating on LiFePO4 cathode materials for lithium-ion batteries. Energy & Environmental Science, 5**,** 5163-5185.

WEI, Y. J., YAN, L. Y., WANG, C. Z., XU, X. G., WU, F. & CHEN, G. **2004**. Effects of Ni Doping on [MnO6] Octahedron in LiMn2O4. The Journal of Physical Chemistry B, 108**,** 18547-18551.

WILLIAMS, G. P. **2001**. X-ray data booklet. X-RAY DATA BOOKLET. 118

WINTER, M. & BESENHARD, J. O. **1999**. Electrochemical lithiation of tin and tin-based intermetallics and composites. Electrochimica Acta, 45**,** 31-50.

WU, H., TU, J., CHEN, X., LI, Y., ZHAO, X. & CAO, G. **2007**. Effects of Ni-ion doping on electrochemical characteristics of spinel LiMn2O4 powders prepared by a spray-drying method. Journal of Solid State Electrochemistry, 11**,** 173-176.

XIA, Y. & YOSHIO, M. **1997**. Studies on Li-Mn-O spinel system (obtained from melt-impregnation method) as a cathode for 4 V lithium batteries Part IV. High and low temperature performance of LiMn2O4. Journal of Power Sources, 66**,** 129-133.

XIA, Y. **2008**. Development of Low Cost Cathode Materials for Lithium-ion Batteries. Department of Energy and Materials Science, Graduate School of Science and Engineering (Saga University.

XU, K. **2004**. Nonaqueous liquid electrolytes for lithium-based rechargeable batteries. Chemical Reviews, 104**,** 4303-4418.

YAMADA, A. & TANAKA, M. **1995**. Jahn-Teller structural phase transition around 280 K in LiMn2O4. Materials research bulletin, 30**,** 715-721.

YAMADA, A., TANAKA, M., TANAKA, K. & SEKAI, K. **1999**. Jahn–Teller instability in spinel Li–Mn–O. Journal of Power Sources, 81–82**,** 73-78.

YANG, S., JIA, J., DING, L. & ZHANG, M. **2003**. Studies of structure and cycleability of LiMn2O4 and LiNd0.01Mn1.99O4 as cathode for Li-ion batteries. Electrochimica Acta, 48**,** 569- 573.

YANG, Z., ZHANG, J., KINTNER-MEYER, M. C., LU, X., CHOI, D., LEMMON, J. P. & LIU, J. **2011**. Electrochemical energy storage for green grid. Chemical Reviews, 111**,** 3577- 3613. 119.

YI, T.-F., HU, X.-G., DAI, C.-S. & GAO, K. **2007**. Effects of different particle sizes on electrochemical performance of spinel LiMn2O4 cathode materials. Journal of materials science, 42**,** 3825-3830.

YING, J., WAN, C. & JIANG, C. **2001**. Surface treatment of LiNi0.8Co0.2O2 cathode material for lithium secondary batteries. Journal of Power Sources, 102**,** 162-166.

YUNJIAN, L., XINHAI, L., HUAJUN, G., ZHIXING, W., QIYANG, H., WENJIE, P. & YONG, Y. **2009**. Electrochemical performance and capacity fading reason of LiMn2O4 graphite batteries stored at room temperature. Journal of Power Sources, 189**,** 721-725.

ZABAN, D., A., SCHECHTER, A., EIN-ELI, Y., ZINIGRAD, E. & MARKOVSKY, B. **1995**. The Study of Electrolyte Solutions Based on Ethylene and Diethyl Carbonates for Rechargeable Li Batteries I. Li Metal Anodes. Journal of the Electrochemical Society, 142**,** 2873-2882.

ZHAO, X., REDDY, M., LIU, H., RAMAKRISHNA, S., RAO, G. S. & CHOWDARI, B. V. **2012**. Nano LiMn2O4 with spherical morphology synthesized by a molten salt method as cathodes for lithium ion batteries. RSC Advances, 2**,** 7462-7469.

ZHOU, M., CHEN, S., ZHAO, S. & MA, H. **2006**. RETRACTED: One-step synthesis of Au– Ag alloy nanoparticles by a convenient electrochemical method. Physica E: Low-dimensional Systems and Nanostructures, 33**,** 28-34.

ZHU, H.-L., CHEN, Z.-Y., JI, S. & LINKOV, V. **2008**. Influence of different morphologies on electrochemical performance of spinel LiMn2O4. Solid State Ionics, 179**,** 1788-1793.

.

REFERENCES